

**IMPERIAL**

**COMPUTATIONAL DISCOVERY OF  
HYBRID CHALCOGENIDE PEROVSKITE  
PHOTOVOLTAICS**

Author

**JJ ACTON**

CID: 02529224

Supervised by

**DR ALEX GANOSE**

**DR JARVIST FROST**

A Thesis submitted in fulfillment of requirements for the degree of  
**Master of Research in Soft Electronic Materials**

Department of Physics  
Imperial College London  
2024



## Abstract

Chalcogenide perovskites are an emerging class of photovoltaics due to their highly stable, lead-free structures and promising optoelectronic properties. To date, the literature on chalcogenide perovskites focuses predominantly on fully inorganic systems such as  $\text{BaZrS}_3$ . In this work, first principles calculations using density functional theory (DFT) were performed to carry out theoretical computations on a range of hybrid organic-inorganic chalcogenide perovskite materials. We utilised a variety of monovalent and divalent cations within the A-site to assess their electronic, optical, and thermodynamic properties, evaluating their suitability as photovoltaic absorber materials. Our comprehensive analysis revealed hydrazinium zirconium sulfide ( $\text{N}_2\text{H}_6\text{ZrS}_3$ ) showed the most promising results by exhibiting a stable perovskite structure with a direct bandgap of 1.68 eV with an indirect bandgap of 1.18 eV. These bandgap characteristics contributed to a theoretical maximum efficiency of 18.27%. This study represents the first comprehensive computational report on hybrid chalcogenide perovskites, opening new avenues for the development of highly efficient, stable, and environmentally friendly photovoltaic materials.



## Acknowledgments

I would like to thank Dr Alex Ganose and Dr Jarvist Frost for their support and advice throughout my time writing this thesis. Additionally, I would like to express my gratitude to the Virtual Atoms group for always making time to give their insights to any questions I had.



# Contents

<b>Abstract</b>	<b>i</b>
<b>Acknowledgments</b>	<b>iii</b>
<b>List of Acronyms</b>	<b>ix</b>
<b>List of Figures</b>	<b>xv</b>
<b>List of Tables</b>	<b>xix</b>
<b>1 Introduction</b>	<b>1</b>
1.1 Principles of Photovoltaic Solar Cells . . . . .	2
1.1.1 Photovoltaic Mechanisms . . . . .	2
1.1.2 Solar Cell Architecture . . . . .	5
1.1.3 Properties of Photovoltaic Solar Cells . . . . .	8
1.2 Generations of Solar Cells . . . . .	10
1.2.1 Crystalline Silicon Solar Cells . . . . .	10
1.2.2 Thin film Photovoltaics . . . . .	11
1.2.3 Emerging Photovoltaics . . . . .	13
1.2.4 Perovskite Solar Cells . . . . .	16
1.2.5 Hybrid Organic-Inorganic Perovskites . . . . .	19
1.2.6 Challenges in Perovskite Materials . . . . .	21
1.2.7 Ruddlesden-Popper Perovskites . . . . .	24

<b>2 Chalcogenide Perovskites</b>	<b>25</b>
2.1 Experimental Reports of Chalcogenide Perovskites . . . . .	28
2.2 Tolerance and Octahedral Factors . . . . .	31
2.3 Computational Reports of Chalcogenide Perovskites . . . . .	32
2.4 Chalcogenide Perovskite Properties . . . . .	45
2.4.1 Stability . . . . .	45
2.4.2 Chemical Properties . . . . .	48
2.4.3 Optoelectronic Properties . . . . .	50
2.4.4 Defect Chemistry and Doping . . . . .	51
2.5 Synthesis Methods . . . . .	53
2.6 Hybrid Chalcogenide Perovskites . . . . .	56
<b>3 Research Outline</b>	<b>59</b>
<b>4 Computational Theory</b>	<b>61</b>
4.1 Quantum Mechanical Approaches . . . . .	61
4.2 Hartree-Fock Method . . . . .	63
4.3 Density Functional Theory . . . . .	65
4.4 Exchange-Correlation Functional . . . . .	66
4.4.1 LDA and GGA . . . . .	67
4.4.2 Hybrid Density Functional Theory . . . . .	69
4.5 Quantum Mechanics in Solid State . . . . .	70
4.5.1 Periodic Boundaries and The Unit Cell . . . . .	70
4.5.2 The Brillouin Zone and The Reciprocal Lattice . . . . .	71
4.5.3 Basis Sets and Pseudopotentials . . . . .	73
<b>5 Methodology</b>	<b>77</b>
5.1 Vienna <i>Ab Initio</i> Simulation Package . . . . .	77
5.2 Organic Cation Substitution . . . . .	78

---

5.3	Geometric and Electronic Optimisation . . . . .	78
5.4	<i>Ab Initio</i> Molecular Dynamics . . . . .	79
5.4.1	Machine Learning Force Fields . . . . .	80
5.5	Thermodynamic Stability . . . . .	80
5.6	Electronic Structure Calculations . . . . .	81
5.6.1	Density of States . . . . .	81
5.6.2	Band Structures . . . . .	82
5.6.3	Effective Masses . . . . .	82
5.7	Optical Calculations . . . . .	83
5.7.1	Dielectric Values and Optical Absorption . . . . .	83
5.7.2	Spectroscopic Limited Maximum Efficiency . . . . .	84
5.7.3	Band Alignment . . . . .	85
<b>6</b>	<b>Results and Discussion</b>	<b>87</b>
6.1	Inorganic Chalcogenide Perovskites . . . . .	87
6.2	Hybrid Organic-Inorganic Chalcogenide Perovskites . . . . .	93
6.3	Material Screening . . . . .	94
6.4	Geometric and Electronic Optimisation . . . . .	95
6.5	Electronic Properties . . . . .	98
6.6	Optical Properties . . . . .	106
6.7	<i>Ab Initio</i> Molecular Dynamics . . . . .	109
6.8	Thermodynamic Properties . . . . .	110
6.9	Band Alignments . . . . .	112
6.10	HZ(Zr, Hf)(S, Se) <sub>3</sub> Trends . . . . .	113
6.10.1	Chemical Composition Analysis . . . . .	113
6.10.2	Charge Density Analysis . . . . .	115
	<b>Conclusions and Further Work</b>	<b>119</b>



# List of Acronyms

**AIMD** *Ab Initio* Molecular Dynamics

**BHJ** bulk heterojunction

**B-O** Born-Oppenheimer

**CB** conduction band

**CBM** conduction band minimum

**CdTe** cadmium telluride

**CIGS** copper indium gallium selenide

**CT** charge transfer

**CVD** chemical vapour deposition

**DFPT** Density Functional Perturbation Theory

**DFT** Density Functional Theory

**DOS** Density of States

**DSSC** dye-sensitised solar cells

**EA** electron affinity

**ETL** electron transfer layer

**FF** fill factor

**FTO** fluorine-doped tin oxide

**GaAs** gallium arsenide

**GGA** Generalised Gradient Approximation

**HDFT** Hybrid Density Functional Theory

**HF** Hartree-Fock

**HOIP** hybrid organic-inorganic perovskites

**HOMO** highest occupied molecular orbital

**HSE06** Heyd, Scuseria and Ernzerhof functional

**HTL** hole transfer layer

**HZ** hydrazinium

**IP** ionisation potential

$I_{sc}$  short-circuit current

**ITO** tin-doped indium oxide

**JDOS** joint density of states

$J_{ph}$  photogenerated current density

$J_{sc}$  short-circuit current density

**KS** Kohn-Sham

**kWh** kilowatt-hour

**LCAO** linear combination of atomic orbitals

**LDA** Local Density Approximation

**LED** light emitting diodes

**LUMO** lowest unoccupied molecular orbital

**MD** molecular dynamics

**ML** machine learning

**MLFF** machine learning force fields

**NFA** non-fullerene acceptors

**OPV** organic photovoltaics

**PAW** projector augmented wave

**PBE** Perdew, Burke and Ernzerhof functional

**PBESol** Perdew, Burke and Ernzerhof functional adapted for solids and surfaces

**PCBM** phenyl-C<sub>61</sub>-butyric acid methyl ester

**PCE** power conversion efficiency

**PDFT** periodic density functional theory

**PDOS** partial density of states

**PL** photoluminescence

**PSC** perovskite solar cells

**PV** photovoltaic

**QDSC** quantum dot solar cells

**SCF** self-consistent field

**SEM** scanning electron microscopy

**Si** silicon

**SLME** spectroscopic Limited Maximum Efficiency

**SOC** spin-orbit coupling

**SQ** Shockley-Queisser

**SRH** Shockley-Read-Hall

**TISE** time independent Schrödinger equation

**UPS** ultraviolet photoelectron spectroscopy

**VASP** Vienna Ab initio Simulation Package

**VB** valence band

**VBM** valence band maximum

$V_{oc}$  open-circuit voltage

**XRD** x-ray diffraction

**XRF** x-ray fluorescence



# List of Figures

1.1	Illustration of the photoexcitation of an electron in a direct and indirect semiconductor. The black arrow indicates the electron moving from the valence band maximum to the conduction band minimum, with the difference in energy being the bandgap, $E_g$ . The incident photon is represented by $\gamma$ and the change in crystal momentum by absorption or emission of a phonon is represented by $\beta$ in the indirect semiconductor. . . . .	4
1.2	(a) Standard solar cell architecture. (b) Illustration of a <i>p-n</i> junction within the photoactive absorber material in action. The <i>n</i> -type (orange shaded region) and <i>p</i> -type region (purple shaded region) show the formation of a depletion region upon contact and the formation of an electric field (yellow arrows). The large filled blue circles represent the <i>p</i> -type dopant ions while the large filled green circles represent the <i>n</i> -type dopant ions. Upon absorption of a photon ( $\gamma$ ), an electron-hole pair is generated within the depletion region. The bias of the electric field causes the electron (small green filled circle) to move toward the <i>n</i> -type material and the hole (small hollow blue circle) to move towards the <i>p</i> -type material as indicated by the white arrows. Illustration adapted from Ref. 1 . . . . .	6
1.3	Illustration of an energy level diagram in a solar cell. Electron-hole pairs are generated by absorption of a photon ( $\gamma$ ), and separated into free electrons ( $e^-$ ) and free holes ( $h^+$ ). The electrons move down in energy towards the cathode while holes move up in energy toward the anode. . . . .	7
1.4	Typical J-V curve for a solar cell. The fill factor (FF) can be calculated by the ratio of the orange region to the blue region - that being $\frac{V_{MPP} \times J_{MPP}}{V_{oc} \times J_{sc}}$ . . . . .	9
1.5	The Shockley-Queisser limit for a single junction solar cell as a function of power conversion efficiency (PCE) and bandgap energy. . . . .	9
1.6	Cubic perovskite structure where A is an inorganic/organic cation, B is a metal cation and X is an anion. . . . .	17
1.7	Cubic phase perovskite structure of $\text{CH}_3\text{NH}_3\text{PbX}_3$ where the X-site is a halide anion. . . . .	20

---

1.8	A J-V curve depicting the changes in current density as a function of applied electric field for a forward and reverse scan. Figure reproduced from Ref. 2. . . . .	23
2.1	Most common polytypes of $\text{ABX}_3$ chalcogenides. . . . .	27
2.2	Bandgap of 18 $\text{ABX}_3$ compounds in the distorted perovskite, “needle-like”, and hexagonal phases calculated with the Heyd, Scuseria and Ernzerhof functional (HSE06) functional. The optimal band gap region for solar-cell materials is highlighted in light green. An extended region for theoretical efficiencies above 28% is highlighted in light red. Figure reproduced from Ref. 3. <sup>4</sup> . . . . .	35
2.3	(a) Calculated Goldschmidts tolerance factor for chalcogenide perovskites. (b) Computed bandgaps of chalcogenide perovskites with the optimal bandgap located within the gold horizontal bar. Figure reproduced from Ref. 5. . . . .	37
2.4	(a) Computed optical absorption spectra (calculated using HSE06) of several materials with distorted perovskite structure, compared to Si and $\text{MAPbI}_3$ . The absorption coefficient of $\text{MAPbI}_3$ is computed using the Perdew, Burke and Ernzerhof functional (PBE) functional without considering the spin-orbit coupling (SOC) effect. (b) Computed band structure of $\text{SrSnSe}_3$ . (c) Computed partial density of states (PDOS) of $\text{SrSnSe}_3$ with distorted perovskite structure. Figure reproduced from Ref. 5. . . . .	38
2.5	(a) Formation energies and PBE calculated band gaps of 77 types of perovskites. (b) Formation energies and PBE calculated band gaps of 20 stable perovskites. Solid symbols indicate that such a compound has been synthesised in experiments. Figure reproduced from Ref. 6. . . . .	40
2.6	(a) Calculated optical absorption coefficients of six types of perovskites with $\text{MAPbI}_3$ and as a comparison GaAs. (b) Calculated conversion efficiency of six types of perovskites, $\text{MAPbI}_3$ and GaAs. Figure reproduced from Ref. 6. <sup>4</sup> . . . . .	41
2.7	Angle variance, $\sigma^2$ , as a function of the quadratic elongation, $\lambda$ , in (a) chalcogenide compounds and (b) halide perovskites . (c) Colour map plot of chalcogenides and halides using Tolerance factor (TF); (d) colour map using $\Delta H_c$ (in eV/ion). For an ideal cubic perovskite, $\lambda=1$ , $\sigma^2=0$ and $\Delta H_c= 0.0$ eV/ion. Figure reproduced from Ref. 7. . . . .	44
2.8	Gaussian kernel density estimates of $\Delta H_c$ for each A-site cation. Figure reproduced from Ref. 7. Represents how the A-site cation radius, $r_A$ , effects $\Delta H_c$ in chalcogenide and halide perovskites. . . . .	44

---

2.9 Photoluminescence characteristics of BaZrS <sub>3</sub> compared to MAPbI <sub>3</sub> . (a) Absorption coefficient and photoluminescence spectrum at room temperature. (b) BaZrS <sub>3</sub> photoluminescence intensity spectra over five weeks under ambient conditions. (c) MAPbI <sub>3</sub> photoluminescence intensity spectra over two weeks under ambient conditions. (d) Photoluminescence of BaZrS <sub>3</sub> and MAPbI <sub>3</sub> under ambient conditions. Figure reproduced from Ref. 8. <sup>4</sup>	46
2.10 (a) Simulated interatomic distance of BaZrS <sub>3</sub> and H <sub>2</sub> O. (b) Simulated interatomic distance of MAPbI <sub>3</sub> and H <sub>2</sub> O. (c) Anion migration paths in BaZrS <sub>3</sub> and MAPbI <sub>3</sub> . (d) Energy barriers for sulphur vacancies and iodine vacancies. Figures reproduced from Ref. 8. <sup>4</sup>	47
2.11 Thermogravimetric analysis mass change for various chalcogenide structures. Figure reproduced from Ref. 9.	48
2.12 Bar chart representing the abundance of common elements used in solar cell. Those in blue are common to chalcogenide perovskites while orange indicates elements of other common photovoltaics. Data from Ref. 10.	49
2.13 Formation energies of intrinsic point defects in BaZrS <sub>3</sub> as a functional of Fermi level, under (a) S-poor and (b) S-rich conditions. The Fermi level is referenced to the (valence band maximum (VBM)) of BaZrS <sub>3</sub> . The slopes of the formation-energy lines indicate defect charge states and the dots denote charge-state transition levels. Figure reproduced from Ref. 11.	52
4.1 A 1 × 1 × 1 conventional unit cell (purple) surrounded by unit cells (dashed green) to represent periodicity to form a 3 × 3 × 1 expanded unit cell. Image reproduced from Ref. 12	70
4.2 Illustration of a pseudopotential describing the wavefunction within the cutoff region, $r_c$ . $\Psi$ (blue dashed line) represents the true all electron wavefunction while $\tilde{\Psi}$ (red line) represents the pseudopotential wavefunction.	73
6.1 Optimised structure of (a) BaZrS <sub>3</sub> and (b) BaHfS <sub>3</sub> .	89
6.2 Partial density of states and band structure of (a-b) BaZrS <sub>3</sub> and (c-d) BaHfS <sub>3</sub> .	90
6.3 HSE06 calculated optical absorption spectra for BaZrS <sub>3</sub> and BaHfS <sub>3</sub> as a function of energy. Full lines indicate the optical absorption and dashed lines indicate the fundamental bandgap.	91
6.4 spectroscopic Limited Maximum Efficiency (SLME) for BaZrS <sub>3</sub> and BaHfS <sub>3</sub> as a function of film thickness, calculated using HSE06.	92

---

6.5	Hybrid chalcogenide perovskites with a stable perovskite structure and monovalent A-site cation calculated using HSE06. (a) HY $\text{Sb}$ $\text{S}_3$ , (b) HY $\text{Bi}$ $\text{S}_3$ , (c) HY $\text{BiSe}_3$ , (d) AM $\text{BiSe}_3$ , (e) HABi $\text{Se}_3$ , (f) MAMBi $\text{Se}_3$ . 100
6.6	Atomic structures for optimised $2 \times 2 \times 2$ supercells of hydrazinium (HZ) compounds. Calculations were completed using Perdew, Burke and Ernzerhof functional adapted for solids and surfaces (PBEsol) functional. (a-b) HZZr $\text{S}_3$ , (c-d) HZZr $\text{Se}_3$ , (e-f) HZHf $\text{S}_3$ and (g-h) HZHf $\text{Se}_3$ . . . . . 102
6.7	Partial density of states and band structure of (a-b) HZZr $\text{S}_3$ , (c-d) HZZr $\text{Se}_3$ , (e-f) HZHf $\text{S}_3$ and (g-h) HZHf $\text{Se}_3$ . All calculated using HSE06. 104
6.8	HSE06 calculated optical absorption spectra for AMBi $\text{Se}_3$ and HABi $\text{Se}_3$ as a function of energy. Full lines indicate the optical absorption and dashed lines indicate the fundamental bandgap . . . . . 106
6.9	(a) HSE06 calculated optical absorption spectra for HZ(Zr, Hf)(S, Se) $_3$ compounds as a function of energy. (b) SLME for HZ(Zr, Hf)(S, Se) $_3$ compounds as a function of film thickness, calculated using HSE06. BaZr $\text{S}_3$ and BaHf $\text{S}_3$ compounds included as a comparison. . . . . 107
6.10	HZZr $\text{S}_3$ after 10 ps of <i>Ab Initio</i> Molecular Dynamics (AIMD) normal to the (a) a-direction and (b) c-direction. (c) Plot of the temperature and energy per atom as a function of time for HZZr $\text{S}_3$ . . . . . 110
6.11	Convex hull of each HZ chalcogenide. (a) HZZr $\text{S}_3$ , (b) HZZr $\text{Se}_3$ , (c) HZHf $\text{S}_3$ , (d) HZHf $\text{Se}_3$ . . . . . 111
6.12	Band alignments for each HZ compound. . . . . 113
6.13	Direct and indirect bandgaps plotted for HZ perovskites. . . . . 114
6.14	Comparison of changes in electron and hole effective masses in hydrazinium compounds. Effective mass is in units of electron rest mass. 115
6.15	Band structure and partial charge density isosurface of (a) the VBM C-point of HZZr $\text{S}_3$ and (b) the VBM T-point BaZr $\text{S}_3$ . Zirconium atoms are in purple and sulphur are in black. The isosurface level is set to 2 meV/ $\text{\AA}$ . Barium and hydrazinium have been excluded for image clarity. . . . . 116

# List of Tables

1.1	Perovskite phase formed at varying Goldschmidt ( $t$ ) and octahedral ( $\mu$ ) factors. . . . .	18
2.1	Phases of experimentally reported chalcogenide crystal structures. Those in bold have had multiple phases reported. . . . .	30
2.2	Experimentally verified chalcogenide perovskites (where X= S, Se) with bandgaps determined. Adapted from Ref. 13 and 14. . . . .	30
2.3	Calculated formation energy (eV/f.u.) for ABX <sub>3</sub> compounds in the distorted perovskite, “needle-like” and hexagonal phases relative to the perfect perovskite phase. Materials in bold are most stable in the distorted perovskite phase or are within 45 meV/f.u. of the most stable phase. Table reproduced from Ref. 3. . . . .	36
2.4	PBE0-calculated band gap and effective mass. Materials in bold have both a optimal bandgap and an effective mass less than $m_0$ . Table reproduced from Ref. 6 with only X= S, Se included. . . . .	41
2.5	Synthesis methods for chalcogenide perovskites. Table reproduced from Ref. 15 with more recent synthesis methods added. . . . .	54
6.1	Calculation parameters for BaZrS <sub>3</sub> and BaHfS <sub>3</sub> . . . . .	88
6.2	Calculated lattice parameters and respective deviations from experimental values. <sup>16</sup> . . . . .	88
6.3	The calculated direct bandgap ( $E_g^d$ ), indirect bandgap ( $E_g^i$ ), electron effective mass ( $m_e$ ) and hole effective mass ( $m_h$ ) for inorganic chalcogenide perovskites. Effective masses are in units of rest mass ( $m_0$ ). . . . .	91
6.4	Optical properties of BaZrS <sub>3</sub> and BaHfS <sub>3</sub> . Includes high-frequency dielectric constants ( $\epsilon_\infty$ ) along the X, Y and Z directions at 0 eV and the Spectroscopic Limited Maximum Efficiency (SLME). . . . .	92
6.5	Organic cations used as an A-site molecules in the ABX <sub>3</sub> perovskite structure. All molecular weights were taken from Ref. 17. . . . .	95

6.6	The 50 compounds examined in this report with their converged k-points and phases formed after geometric optimisation and electronic convergence. The cutoff energy for all compounds was 500 eV. The compounds are split into sulphur and selenium based perovskites. The upper rows separated by the horizontal black line represent monovalent cations while the lower rows are compounds with divalent A-site cations. . . . .	96
6.7	Effective radius ( $R_A$ ) and ionic radii ( $R_B, R_X$ ) used to calculate the tolerance factor ( $t$ ) and octahedral factor ( $\mu$ ) as well as the associated number of cation lone pairs ( $N_{LP}$ ) for the chalcogenide perovskites. . . . .	98
6.8	Lattice parameters for the stable chalcogenide perovskites calculated using PBEsol functional. . . . .	98
6.9	Electronic properties of hydrazinium based compounds. The direct and indirect bandgaps are given in eV, and the effective masses ( $m_e$ and $m_h$ ) are given in units of the electron rest mass. . . . .	103
6.10	Optical properties of HZ based chalcogenide perovskites. Includes high-frequency ( $\varepsilon_\infty$ ) and static ( $\varepsilon_{\text{ionic}}$ ) dielectric responses along the X, Y, and Z directions at 0 eV and the total dielectric constant ( $\varepsilon_0$ ). The corresponding SLME for each compound is also provided. $\varepsilon_\infty$ calculated using HSE06 and $\varepsilon_{\text{ionic}}$ calculated using Density Functional Perturbation Theory (DFPT). . . . .	108
6.11	Formation energy and competing phases of HZ containing compounds. 111	

# 1

## Introduction

### Contents

---

<b>1.1 Principles of Photovoltaic Solar Cells . . . . .</b>	<b>2</b>
1.1.1 Photovoltaic Mechanisms . . . . .	2
1.1.2 Solar Cell Architecture . . . . .	5
1.1.3 Properties of Photovoltaic Solar Cells . . . . .	8
<b>1.2 Generations of Solar Cells . . . . .</b>	<b>10</b>
1.2.1 Crystalline Silicon Solar Cells . . . . .	10
1.2.2 Thin film Photovoltaics . . . . .	11
1.2.3 Emerging Photovoltaics . . . . .	13
1.2.4 Perovskite Solar Cells . . . . .	16
1.2.5 Hybrid Organic-Inorganic Perovskites . . . . .	19
1.2.6 Challenges in Perovskite Materials . . . . .	21
1.2.7 Ruddlesden-Popper Perovskites . . . . .	24

---

As the demand for energy rises, so does the need for consistent and sustainable energy production. At present, fossil fuels dominate the energy market supply and subsequently account for 75% of global emissions and 90% of carbon dioxide emissions annually.<sup>18</sup> It is estimated that current levels of energy consumption will double by 2050, requiring an additional 13 TW of energy to be produced in line with this rise in demand.<sup>19</sup> The current global demand has primarily been met through by natural gas, oil and coal, acting as the cornerstone for energy production, driving

industrialisation and economic growth. However, due to the finite nature of these energy sources, it is imperative that energy production methods transition to more renewable sources. In recent years, the volatility of fossil fuel prices has further underscored the need for alternative energy solutions.<sup>20</sup> Of the energy sources currently available, solar energy is by far the most plentiful with the total power of the Sun's radiation that is incident on Earth being  $1.4 \times 10^{17}$  W - more than 5,000 times greater than the global energy demand predicted for 2050.<sup>19</sup> Photovoltaic solar cells have experienced significant technological advancements in recent decades which has seen the global photovoltaic (PV) market size increase from \$2.5 B in 2000 to \$96.5 B in 2023 with predictions of increases to \$238.99 B by 2032.<sup>21</sup> This increase is being driven by lower cost per kilowatt-hour (kWh), increased module efficiencies and government subsidies through green policies. As photovoltaics become increasingly more integrated into our lives, it is important to develop solar cells that are not only highly efficient but also non-toxic and made from Earth-abundant materials. Currently, many solar cell technologies encounter challenges related to their production, including high fabrication costs and the use of toxic and rare elements, which impedes their large-scale production potential.<sup>22,23</sup> To ensure the sustainability of solar energy as a mainstream power source, future innovations must focus on creating affordable, environmentally friendly solar cells that can be manufactured on a large scale basis.

## 1.1 Principles of Photovoltaic Solar Cells

### 1.1.1 Photovoltaic Mechanisms

The production of electricity through the absorption of photons is demonstrated through the photovoltaic effect, first discovered by French physicist, Edmund Becquerel in 1839.<sup>24</sup> Progress was continued by Charles Fritts in the 1880s, who de-

signed the first solid state PV cell made from selenium, to produce a solar cell with an efficiency of 1% by converting the visible range of light into electricity.<sup>25</sup> Further advancements were made in the 1920's to establish the foundations of quantum and band theory, fundamental to our current understanding of the photovoltaic effect.<sup>26</sup> A solar cell can simply be thought of as a semiconducting diode that requires the photovoltaic effect to function. The photovoltaic effect being a two stage mechanism consisting of a photogeneration stage followed by a charge separation stage.<sup>27</sup> When a photon of high enough energy (i.e an energy greater than the bandgap) is absorbed in a material, photogeneration will occur, forming an electron-hole pair. This electron-hole pair is formed by the excitation of an electron from the valence band (VB) to the conduction band (CB). A positively charged hole remains in the VB at the location the electron had previously occupied. The electron and hole are no longer bound to atoms and can be described as free charges. In a semiconducting material these free charges produce a photocurrent, while subsequently producing a photovoltage from the potential difference across the CB and VB. This current and voltage can then be applied to an external circuit, generating electricity. For a semiconducting material to efficiently absorb photons a direct bandgap is desirable. A direct bandgap is formed when the conduction band minimum (CBM) and VBM align in  $k$ -space, otherwise an indirect bandgap is formed. An indirect bandgap is a result of different energy eigenvalues across various  $k$ -values within the Brillouin zone, leading to the emission or absorption of a phonon to conserve crystal momentum.<sup>28-32</sup> This results in the absorption of photons only occurring in an indirect bandgap material when there is an adequate number of phonons available with the correct  $k$ -value. As a consequence, optical absorption is weaker in indirect bandgap materials, necessitating thicker absorption layers compared to direct bandgap materials.<sup>33</sup> A representation of this concept can be seen in Figure 1.1.

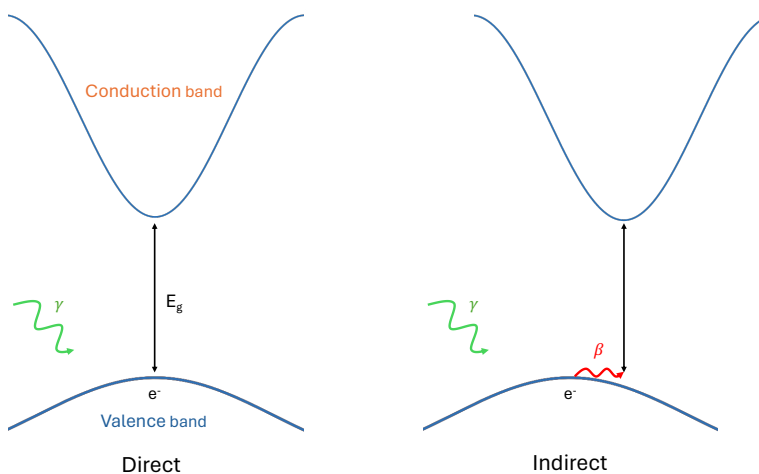


Figure 1.1: Illustration of the photoexcitation of an electron in a direct and indirect semiconductor. The black arrow indicates the electron moving from the valence band maximum to the conduction band minimum, with the difference in energy being the bandgap,  $E_g$ . The incident photon is represented by  $\gamma$  and the change in crystal momentum by absorption or emission of a phonon is represented by  $\beta$  in the indirect semiconductor.

Charge separation occurs when the photogenerated electron-hole pairs are separated within a *p-n* junction, made possible in inorganic semiconductors by their low binding energy,  $E_b$ , as a result of their intrinsically high dielectric constants,  $\varepsilon_r$ , as seen in:

$$E_b = \frac{q^2}{4\pi\varepsilon_r\varepsilon_0 r} \quad (1.1)$$

where  $q$  is the elementary charge,  $\varepsilon_0$  is the permittivity of free space and  $r$  is the average separation between an electron and hole. An electron-hole pair will only exist on average, for a time equal to that of the minority carrier lifetime before recombination occurs, making charge separation a fundamental component of a solar cells function.<sup>34</sup> Recombination processes occur due to intrinsic physical processes as well as from defects in solar cells. The essential physical processes result in radiative recombination and Auger recombination which are unavoidable, whereas non-radiative recombination and Shockley-Read-Hall (SRH) recombination are preventable through the use of high purity materials, careful interfacial engineering and

advanced fabrication techniques.<sup>35–37</sup>

### 1.1.2 Solar Cell Architecture

A typical *p-n* junction solar cell architecture comprises of metallic electrode, an electron transfer layer (ETL), a photoactive absorber material, a hole transfer layer (HTL) and a transparent conducting contact such as tin-doped indium oxide (ITO) conducting glass (Figure 1.2a). A *p*-type material is one that the majority carriers are holes, while an *n*-type material has electrons as the majority carrier. The photoactive absorber material can be produced from the same material with each side doped to produce a *p*-type side and an *n*-type side such as in a silicon (Si) solar cell. Otherwise, a *p*-type and *n*-type material can be used to form a heterojunction such as those utilised in cadmium telluride (CdTe) solar cells.<sup>38</sup> It is noted that in silicon solar cells the ETL and HTL are referred to as the emitter and passivation layers, respectively. Additionally, if the semiconductor is not easily doped, an intrinsic, *i*, region can be included to form an *n-i-p* or inverted *p-i-n* architecture.

Traditional silicon solar cells are based on a *p-n* junction where an electric field is formed by the diffusion of the majority carriers of the *p* and *n*-type materials along the interface. Upon contact, a diffusion gradient is formed, where electrons move from the electron-rich *n*-type material to the hole-rich *p*-type material. As diffusion occurs electrons and holes recombine resulting in the depletion of the majority carriers at the junction.<sup>39</sup> This results in a net positive charge formed in the *n*-type region and net negative in the *p*-type side, forming an electric field to further repel majority carriers from crossing the junction, thus forming a depletion region. As more charges cross the potential barrier it becomes larger, making it more difficult for a continuous stream of charges to cross, eventually resulting in an equilibrium potential barrier where no charges can cross. Under illumination, it is this potential

barrier that results in charge separation in solar cells. The free electron charges are then transported to the electrode on the *n*-types side to an external circuit where they do external work and then travel through the circuit back to the *p*-type side where they recombine with the holes at the electrode. The system stays in equilibrium under illumination as electron-hole pairs are constantly being generated, maintaining a charge imbalance.<sup>25</sup> This process can be seen in Figure 1.2b.

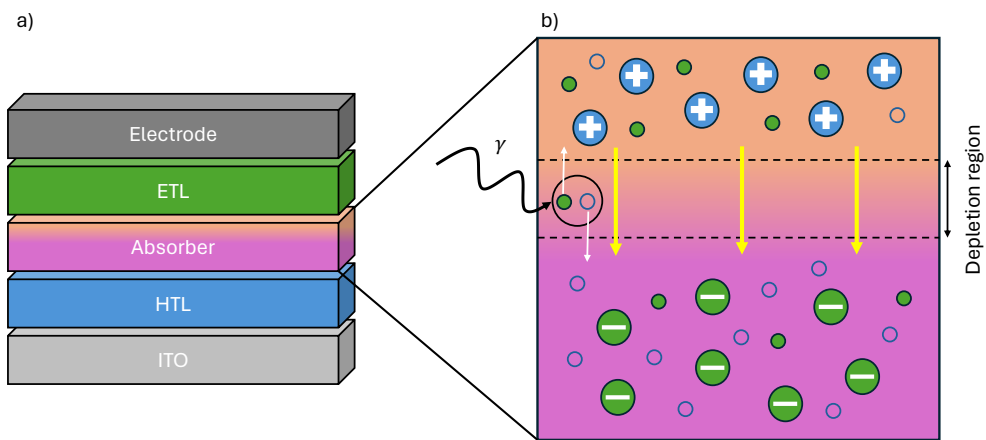


Figure 1.2: (a) Standard solar cell architecture. (b) Illustration of a *p*-*n* junction within the photoactive absorber material in action. The *n*-type (orange shaded region) and *p*-type region (purple shaded region) show the formation of a depletion region upon contact and the formation of an electric field (yellow arrows). The large filled blue circles represent the *p*-type dopant ions while the large filled green circles represent the *n*-type dopant ions. Upon absorption of a photon ( $\gamma$ ), an electron-hole pair is generated within the depletion region. The bias of the electric field causes the electron (small green filled circle) to move toward the *n*-type material and the hole (small hollow blue circle) to move towards the *p*-type material as indicated by the white arrows. Illustration adapted from Ref. 1

At low electric fields, the drift velocity,  $v_d$ , is proportional to the electric field strength,  $\mathbf{E}$ , with the mobility,  $\mu = \frac{\mathbf{E}}{v_d} \text{ cm}^2\text{V}^{-1}\text{s}^{-1}$ . The average charge carrier drift velocity varies for electrons and holes and can be approximated by the Drude mobility equation, where  $q$  is the charge of the free carrier,  $\tau$  is the average scattering

time and  $m^*$  is the effective carrier mass:

$$\mu = \frac{q\tau}{m^*} \quad (1.2)$$

Once the charge carriers are generated and separated in the depletion region they are transported to the electrodes to be used in an external circuit. In the case of generated electrons, they will be transported to the ETL which is used to facilitate the transport of electrons to the cathode. This is done by using an ETL material with a CBM with a slightly higher energy than the cathode and a similar energy as the active layer. This lowers the energy barrier for electron transfer, improving extraction efficiency as well as preventing holes from recombining. For the HTL to be efficient, the anode should have a slightly higher work function than the HTL valence band while having a similar energy level to the active layers valence band.

The energy levels of each component can be seen in Figure 1.3.<sup>40</sup>

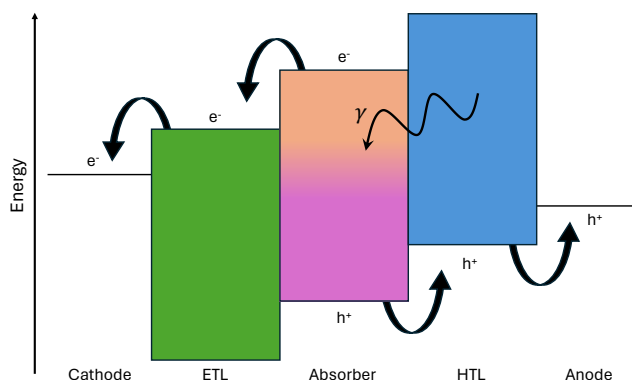


Figure 1.3: Illustration of an energy level diagram in a solar cell. Electron-hole pairs are generated by absorption of a photon ( $\gamma$ ), and separated into free electrons ( $e^-$ ) and free holes ( $h^+$ ). The electrons move down in energy towards the cathode while holes move up in energy toward the anode.

### 1.1.3 Properties of Photovoltaic Solar Cells

The photogenerated current density ( $J_{ph}$ ), of a solar cell is given by the flux of photons with energy greater than the bandgap, therefore an increased bandgap results in a reduced current density as fewer photons have the required energy to be absorbed. The short-circuit current ( $I_{sc}$ ) is a function of the photogenerated current and is equal to the maximum current drawn under illumination when the voltage is zero. The short-circuit current density ( $J_{sc}$ ) is typically used over  $I_{sc}$  to incorporate the area of cell.<sup>41,42</sup> The open-circuit voltage ( $V_{oc}$ ) is the maximum voltage available in a solar cell and occurs when the current equals zero and is calculated by:

$$V_{oc} = \frac{n k_B T}{q} \ln \left( \frac{J_{sc}}{J_0} + 1 \right) \quad (1.3)$$

where  $n$  is the ideality factor,  $k_B$  is the Boltzmann constant,  $q$  is the elementary charge and  $J_0$  is the dark saturation current density.<sup>41,43–45</sup> The  $V_{oc}$  and  $J_{sc}$  give rise to the fill factor (FF) which is characterised by:

$$\text{FF} = \frac{V_{MPP} \times J_{MPP}}{V_{oc} \times J_{sc}} \quad (1.4)$$

where  $V_{MPP}$  and  $J_{MPP}$  are the voltage and current maximum power points, respectively.<sup>46,47</sup> Figure 1.4 shows a J-V curve of a typical solar cell where the FF is a ratio of the  $\frac{V_{MPP} \times J_{MPP}}{V_{oc} \times J_{sc}}$ .

The PCE% ( $\eta$ ) is then defined as:

$$\text{PCE \%}(\eta) = \frac{V_{oc} \times J_{sc} \times \text{FF}}{P_{in}} \times 100 \% \quad (1.5)$$

where  $P_{in}$  is the incident power density. The PCE is tested under standard conditions at 25 °C with an AM 1.5G spectrum and a  $P_{in}$  of 1 kW cm<sup>-2</sup>.<sup>35</sup> The maximum theoretical efficiency of a single junction solar cell is limited to  $\approx 33.7\%$  under

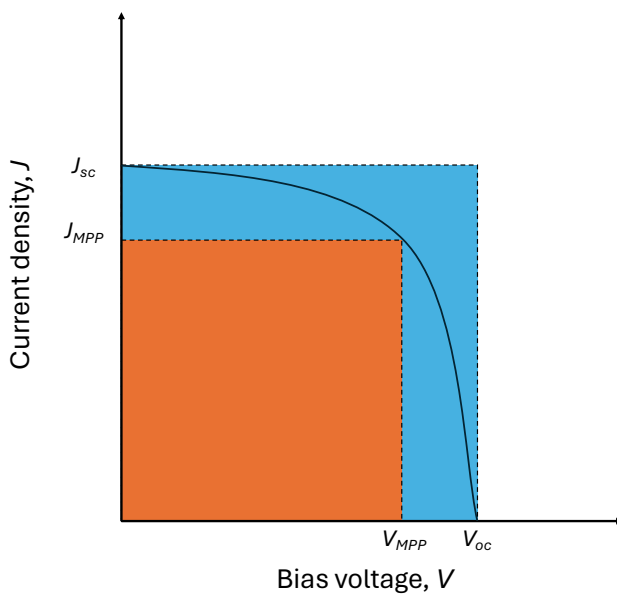


Figure 1.4: Typical J-V curve for a solar cell. The FF can be calculated by the ratio of the orange region to the blue region - that being  $\frac{V_{MPP} \times J_{MPP}}{V_{oc} \times J_{sc}}$ .

the mentioned conditions, calculated by the Shockley-Queisser (SQ) limit.<sup>48</sup> This principle of detailed balance sets a fundamental limit on the conversion efficiency by taking into account by including various loss mechanisms, including recombination, thermal and spectral losses. The SQ limit for a single junction solar cells PCE can be seen as a function of the bandgap in Figure 1.5.

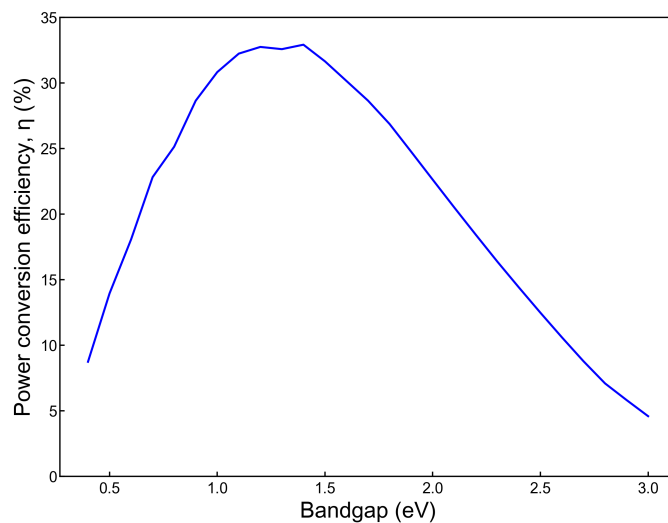


Figure 1.5: The Shockley-Queisser limit for a single junction solar cell as a function of PCE and bandgap energy.

## 1.2 Generations of Solar Cells

### 1.2.1 Crystalline Silicon Solar Cells

The first generation of silicon solar cells were first developed by Chapin et al.<sup>49</sup> in 1954 in Bell Labs which was made possible by utilising the Czochralski method to produce solar cells with a PCE of 8%.<sup>49</sup> A typical silicon solar cell today, comprises of a lightly doped ( $1 \times 10^{16} \text{ cm}^{-3}$ ) *p*-type silicon wafer (300-500  $\mu\text{m}$ ) with a heavily doped ( $1 \times 10^{19} \text{ cm}^{-3}$ ) *n*-type material deposited by chemical vapour deposition (CVD) or ion implantation directly onto the *p*-type base.<sup>50</sup> This results in a silicon wafer which has low sheet resistance, maximised absorption and improved diffusion lengths.<sup>35</sup> Silicon solar cells form a *p-n* junction via this doping to increase the concentration of charge carriers by the addition of group III boron and group V phosphorous to form a *p*-type acceptor and *n*-type donor, respectively. Silicon wafer technologies accounted for over 95%<sup>51</sup> of total photovoltaic production in 2023 due to the abundance of silicon in nature, the longevity of the modules and the high power conversion efficiencies. Nevertheless, silicon solar cells have considerable drawbacks. The most prominent being the possession of an indirect bandgap. Consequently, Si cells require thicker active layers making them cells unsuitable for thin film applications. Si cells are also restricted by their high energetic and economic cost associated with them.<sup>52</sup> Furthermore, single junction silicon cells are nearing the SQ limit of  $\eta_{max} \approx 30\%$  for a 1.1 eV monocrystalline Si solar cell.<sup>48</sup> As the SQ limit is approached, it becomes incrementally more challenging to obtain higher efficiencies, leading to the exploration of new generation photovoltaics increasingly enticing.<sup>53</sup>

### 1.2.2 Thin film Photovoltaics

Thin film photovoltaic have been developed as an alternative to crystalline silicon photovoltaics by having a higher absorption coefficients and direct bandgaps, resulting in shorter minority carrier diffusion lengths and thinner films.<sup>35</sup> Thin film photovoltaics are normally formed from multiple elements compared to elemental silicon, which allows for modifications of properties to enhance performance. Amorphous silicon ( $\alpha$ -Si), copper indium gallium selenide (CIGS) and CdTe comprise of the most common thin films photovoltaics.

#### Amorphous Silicon

Amorphous silicon is an alternative to crystalline silicon. The first cells were produced in 1976 by Carlson and Wronski<sup>54</sup> with an efficiency of 2.4%. Today, amorphous cells have a record PCE of 13.4% demonstrated by Kim et al.<sup>55</sup> Amorphous silicon cells have the benefits of being cheaper to produce compared to crystalline Si. They can also be deposited at lower temperatures ( $<300\text{ }^{\circ}\text{C}$ ) making deposition possible on a variety of substrates, and making them suitable for roll-to-roll manufacturing.<sup>56</sup> Amorphous silicon make use of a *p-i-n* architecture with the intrinsic layer aiding in photon absorption and creating an electric field to drive charge separation.<sup>30</sup> However, due to the amorphous nature, there is a high density of defects and ‘dangling bonds’ resulting in a shorter minority carrier diffusion lengths and sub-optimal electronic properties.<sup>57</sup> This can be alleviated through hydrogen passivation to form hydrogenated amorphous silicon ( $\alpha$ -Si:H).<sup>58</sup> The main disadvantage of  $\alpha$ -Si:H is the intrinsic metastability caused by the addition of hydrogen atoms, known as the Staebler-Wronski effect.<sup>59</sup> Under illumination, photo-degradation of the Si-H bonds occurs over time, resulting in increased defect density, higher recombination rates and thus a reduced FF, diminishing efficiency over time. This

is accompanied by the low maximum theoretical efficiency of  $\approx 15\%$ , much lower than other competing thin film technologies which limits  $\alpha$ -Si:H use in commercial settings.<sup>30,35,60,61</sup>

## CIGS

Copper indium selenide ( $\text{CuInSe}_2$  or CIS) is a ternary compound and is the predecessor to CIGS, first synthesised by Hahn and Mutschke<sup>62</sup> in 1953, and was found to have a bandgap of 1.04 eV. Kazmerski et al.<sup>63</sup> then reported the first  $\text{CuInSe}_2/\text{CdS}$  thin film solar cell in 1976, having an efficiency of 4–5 %. Since then, the addition of gallium has become common to form semiconducting chalcopyrite alloys such as  $\text{Cu}(\text{In}_{1-x}\text{Ga}_x)\text{S}(\text{Se})_2$  (CIGS) to improve light absorption by shifting the bandgap to the visible range.<sup>64</sup> CIGS have advantages over other thin film technologies by not containing highly toxic components and having upper efficiencies of 23.6%.<sup>65</sup> CIGS can also include a variety of alloys, making their bandgaps tuneable from 1–1.6 eV while maintaining low defect densities and high absorption coefficients ( $1 \times 10^5 \text{ cm}^{-1}$ ).<sup>53,60,66</sup> The primary issues surrounding CIGS are the high grain boundary recombination rates as a result of dark currents and high defect density at the heterojunction.<sup>35</sup> Additionally CIGS have a reduced spectral response at increased wavelengths due to the limited collection of charge carriers.<sup>35</sup> These issues can be partially suppressed through passivisation and annealing but still remain as a significant issue in the development of CIGS.<sup>35</sup> Additionally, indium is a scarce metal which can be price volatile, reducing incentives to produce CIGS on a large scale.

## CdTe

The first CdTe cell was reported by Bonnet and Rabenhorst<sup>67</sup> in 1972 and is a group II-VI semiconductor with a direct bandgap of 1.44 eV.<sup>60</sup> Initially CdTe was produced

as a *p*-type photovoltaic material however it has the ability of being doped as *n*-type material, making it an attractive material for use in solar cells. CdTe panels are also flexible and can be made semi-transparent, having potential applications in windows and agrivoltaics.<sup>68</sup> Over the past decades, CdTe efficiency has climbed to 22.6% through optimisations of optical properties via increased carrier lifetimes and improved photocurrent collection.<sup>52,69</sup> Nevertheless, CdTe is limited by Fermi level pinning due to high trapped states at grain boundaries which consequently decreases *p*-type doping efficiency which must be done extrinsically.<sup>70</sup> As well as this, cadmium is extremely toxic and tellurium is a rare element which further limits its widespread adoption.

### 1.2.3 Emerging Photovoltaics

The third generation of solar cells are a group of emerging photovoltaics that attempt to incorporate the properties of previous generations by being affordable, scalable and highly efficient while remaining non-toxic. Emerging photovoltaics use novel techniques and materials in pursuit of advancing solar cell technologies. Optimising these materials has proved arduous, due to many complications involving device interfaces and intrinsic device properties.<sup>71–73</sup> These emerging photovoltaics are primarily still in research stages with limited commercial availability. The main emerging technologies include dye-sensitised solar cells (DSSC), organic photovoltaics (OPV) and perovskite solar cells (PSC). Other emerging technologies which are being developed include quantum dot solar cells (QDSC), multi-junction solar cells and concentrated solar cells with potential to surpass the single junction detailed balance limit by using concepts such as singlet fission and multiple exciton generation.<sup>74</sup>

## Dye-Sensitised Solar Cells

Dye-Sensitised Solar Cells are hybrid organic-inorganic devices based on a nanotechnology, first conceptualised and fabricated by O'Regan and Grätzel<sup>75</sup>. DSSCs contain four essential components: i) A highly porous photoanode, typically TiO<sub>2</sub> (anatase) coated on a transparent conductive glass substrate, ii) a thin layer of dye sensitiser in contact with the TiO<sub>2</sub> coating that absorbs photons and generates excitons, iii) an electrolyte redox system (typically I<sup>-</sup>/I<sub>3</sub><sup>-</sup>) to collect electrons at a counter electrode through an organic solvent and iv) a counter electrode formed from a Ti coated fluorine-doped tin oxide (FTO) glass substrate.<sup>76</sup> Dye sensitised solar cells work through the photoexcitation of electrons within the dye sensitiser molecules in the TiO<sub>2</sub> layer. The electrons are injected into the conduction band of the TiO<sub>2</sub> and diffuse through the permeable film which is facilitated by the energy level imbalance between the sensitiser and TiO<sub>2</sub> in the form of a Schottky barrier. As the electrons are transported, an electric current forms and holes are left in the dye. The holes are subsequently replenished by an electron donation from the iodine in the electrolyte I<sup>-</sup>/I<sub>3</sub><sup>-</sup> redox couple, preventing recombination. In turn, the iodine is reduced by the triiodide at the fluorine tin oxide (FTO) counter electrode, allowing for continued flow of electrons through the circuit.<sup>52,77-80</sup> DSSCs are simple yet effective solar applications which are straightforward to fabricate and can be done at low costs and hence have been commercialised although leave plenty to be desired. Currently, the highest performing DSSC has a PCE of 13.0%<sup>65</sup> and is limited by the potential of the redox couple which results in a large voltage losses. DSSC's also have a narrow spectral absorption range which is difficult to alter due to the ramifications in redox chemistry and charge carrier kinetics.<sup>81</sup>

## Organic Photovoltaics

Organic photovoltaics are based on the use of  $\pi$ -conjugated electronic materials to combine the desirable electronic properties of semiconductors with the advantages of being lightweight, mechanically flexible and being solution processable.<sup>82</sup> Photoconductivity was first observed in anthracene by A. Pochettino and A. Sella<sup>83</sup> in 1906. These electronic properties arise from the overlap of  $p_z$  orbitals forming via  $sp^2$  hybridisation, resulting in a  $\pi$ -conjugated backbone of delocalised electrons.<sup>84</sup> Similar to band theory, organic polymers have a highest occupied molecular orbital (HOMO) and lowest unoccupied molecular orbital (LUMO), analogous to the VBM and CBM, respectively. Under optical excitation a photon is absorbed and a Coulombically bound singlet exciton is formed. This exciton has a binding energy significantly higher than the thermal energy ( $k_B T$ ) as a result of the low dielectric constants seen in organic molecules making charge separation more difficult in OPV. The exciton diffuses through the material to the donor/acceptor (D/A) interface modelled by Förster resonance energy transfer theory.<sup>85</sup> A blended bulk heterojunction (BHJ) is required in organic photovoltaics for efficient charge transfer to occur due to the low exciton diffusion lengths ( $L_D$ ).<sup>86,87</sup> Therefore, an energy offset is required to prevent geminate recombination by using a blend of donor and acceptor materials for the excitons to diffuse across. The exciton can then dissociate at the D/A interface if the energy offset of the HOMO and LUMO between the two materials is greater than the binding energy, resulting in a charge transfer (CT) state. The quantum chemical charge hopping rate of electrons between two sites ( $\Gamma$ ) is described by Marcus theory<sup>88</sup> seen in Equation 1.6 which is dependant on three parameters; the Gibbs free energy between initial and final states ( $\Delta G$ ), the electronic coupling or transfer integral ( $J$ ) and the reorganisation energy ( $\lambda$ ):<sup>28,84,89</sup>

$$\Gamma_{if} = \frac{|J_{if}|^2}{\hbar} \sqrt{\frac{\pi}{\lambda k_B T}} \exp \left[ \frac{-(\Delta G + \lambda)^2}{4\lambda k_B T} \right] \quad (1.6)$$

The free carriers can then diffuse from each other until they are extracted at their respective electrodes while avoiding bimolecular recombination. To date, organic photovoltaic have a record power conversion efficiency of 19.2% set by Zhu et al.<sup>90</sup> which was enabled by a ternary donor-acceptor morphology which improved exciton diffusion lengths while reducing recombination rates. This success has been made possible through decades of exploration of organic molecules and understanding of device physics. The main breakthroughs in organic photovoltaics include the shift from single layer to bilayer cells, improving  $J_{sc}$  and  $FF$  significantly. The use of the BHJ solar cell has also drastically increased the performance of OPVs.<sup>91</sup> Developments in material selection have also improved OPVs performance and stability. The use of non-fullerene acceptors (NFA) allow for tuneable HOMO and LUMO, improved extinction coefficients by improved push-pull hybridisation resulting in highly stable devices compared to fullerene based acceptors such as phenyl-C61-butyric acid methyl ester (PCBM).<sup>92,93</sup> More recently the use of a ternary heterojunction has further improved  $J_{sc}$ ,  $V_{oc}$  and  $FF$  and extended device lifetimes by enhanced charge carrier mobility and active layer morphology.<sup>94</sup> Despite these breakthroughs, as of yet organic photovoltaics have not been widely commercialised due to long term stability issues and inferior efficiencies as a result of lower charge mobility's and energy offsets required for charge carrier separation. The amorphous nature of polymers also results in high non-radiative recombination due to high densities of trapped states, limiting their capabilities.<sup>81</sup>

#### 1.2.4 Perovskite Solar Cells

The crystal structure of a perovskite material is based on the mineral Perovskite  $\text{CaTiO}_3$  discovered in 1839 by Gustav Rose. Perovskite materials have an  $\text{ABX}_3$  crystal structure which exhibits corner sharing  $\text{BX}_6$  octahedra in three dimensions with an A-site atom occupying the centre of each unit cell. This can be viewed in

Figure 1.6.

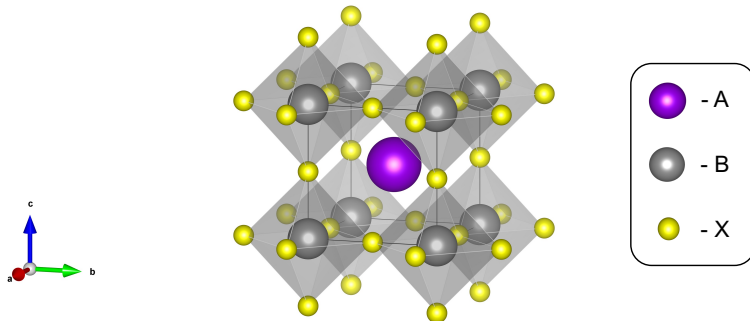


Figure 1.6: Cubic perovskite structure where A is an inorganic/organic cation, B is a metal cation and X is an anion.

The  $\text{ABX}_3$  structure consists of a A-site cation housed in the centre of a  $\text{BX}_6$  octahedra. This octahedra comprises of a B-site cation bonded to six X-site anions which are also bonded to other octahedra producing a perovskite crystal. The A-site cation bonds with the 12 X-site anions to form a cuboctahedron. The high coordination number is made possible due to the high ionicity of perovskites, resulting in a large Coulombic attraction between oppositely charged ions.<sup>13</sup> Perovskite materials can take different crystal phases based on the relative position of the  $\text{BX}_6$  polyhedra. These phases are largely governed by the Goldschmidt and octahedral factors. These parameters are based on the ionic radii of each ion (assumed to be spherical) and predict which crystal phase will be formed. The Goldschmidt tolerance factor ( $t$ ) is defined as:<sup>95</sup>

$$t = \frac{R_A + R_X}{\sqrt{2}(R_B + R_X)} \quad (1.7)$$

where  $R_A$ ,  $R_B$  and  $R_X$  are the ionic radii for the respective site. A tolerance factor of  $0.91 < t < 1$  indicates a perfect cubic structure while  $0.71 < t < 0.9$  indicates a distorted perovskite structure.<sup>95</sup> Generally, when  $t < 0.71$  or  $t > 1$  a corner sharing

octahedra structure is unfavourable and a face or edge sharing structure is more likely to form. The octahedral factor,  $\mu$ , is a measure of whether the B site cation will favour an octahedral coordination with X site atom and is defined as:

$$\mu = \frac{R_B}{R_X} \quad (1.8)$$

The octahedral factor is satisfied when  $0.4 \leq \mu \leq 0.8$ . Table 1.1 shows a summary of the crystal structures based on the Goldschmidt and octahedral factors.<sup>95, 96</sup>

The octahedral factor is often overlooked, however plays an important role in predicting the electronic and optical properties, as they are determined by the  $\text{BX}_6$  octahedra. Therefore, this octahedral geometry must be maintained to ensure a high photovoltaic efficiency.<sup>13</sup> It is important to note these factors do not predict phases with complete accuracy and can be amended for different perovskite variants (oxides, halides, chalcogenides). Perovskite structures bear many unique physical properties such as superconductivity,<sup>97</sup> ultra-low thermal conductivity,<sup>98</sup> high dielectric constants and large absorption coefficients. This has seen perovskites being used in applications such as thermoelectrics, memristors, light emitting diodes (LED) and photovoltaic solar cells.<sup>99-101</sup> This report will focus on perovskites for photovoltaic applications in solar cells. The most widely researched perovskite photovoltaic devices comprise of an organic/inorganic monovalent A-site cation, a divalent metal B-site cation and a halide X-site anion.<sup>102</sup> To maintain charge neutrality in halide based perovskites where  $\text{X} = \text{I}, \text{Br}, \text{Cl}$ , the two cations must have a valence sum to three, such as in  $\text{MAPbI}_3$  where  $\text{MA} = \text{methylammonium}$ .

Table 1.1: Perovskite phase formed at varying Goldschmidt ( $t$ ) and octahedral ( $\mu$ ) factors.

Structure	$t$	$\mu$
Cubic	0.91-1	$\geq 0.41$
Distorted	0.71-0.91	$\geq 0.41$
Non-perovskite	< 0.71 or > 1	< 0.41

### 1.2.5 Hybrid Organic-Inorganic Perovskites

Hybrid organic-inorganic perovskites are crystalline materials with an organic A-site cation and inorganic B and X-site ions. They are advantageous over fully inorganic perovskite structures as they combine the physical properties of organic molecules with the optoelectronic properties of inorganic materials. hybrid organic-inorganic perovskites (HOIP)s are generally easier to process at low temperatures, inexpensive and chemically tuneable making them a low cost, solution processable, high performing solar cell material.<sup>103,104</sup> The exploration of HOIP semiconducting properties were first published by Mitzi et al.<sup>105</sup> in 1994 who characterised the semiconducting properties of  $(C_4H_9NH_3)_2(CH_3NH_3)_{n-1}Sn_nI_{3n+1}$ . Further developments by Chondroudis and Mitzi<sup>106</sup> emanated the discovery of electroluminescence in an organic-inorganic lead halide perovskite and quaterthiophene dye. The first use of HOIPs in solar cells was in 2009, where Miyasaka et al.<sup>107</sup> reported the use of a halide perovskite within a DSSC comprised of a  $CH_3NH_3Pb_3I_3/TiO_2$  anode and Pt-coated FTO anode to obtain a PCE of 3.81%. To date, single junction perovskite have reached record efficiencies of 26.7%.<sup>65,82</sup> Methylammonium lead halides ( $CH_3NH_3^+Pb^{2+}X_3^-$ ) where X=Cl, Br, I (Figure 1.7) are the most widely researched perovskite absorbers and have attracted an immense volume of research in the past decade due to its impressive optical and electronic properties for solar application due to possessing; a direct bandgap of 1.55 eV ( $CH_3NH_3PbI_3$ ), low exciton binding energies, high defect tolerances, remarkable charge carrier diffusion lengths and charge carrier mobility, an impressive absorption coefficient along with a tuneable bandgap making them an incredibly desirable material for solar photovoltaics.<sup>108-119</sup> The desirable properties in lead halide perovskites can be attributed to the  $BX_6$  cage where the conduction band is determined by the overlap of 6p-orbitals of the Pb while the valence band is determined by the overlap of the 6s-orbitals of Pb and 5p-orbitals of I.<sup>120</sup> These properties then impact the CB and VB, directly effecting

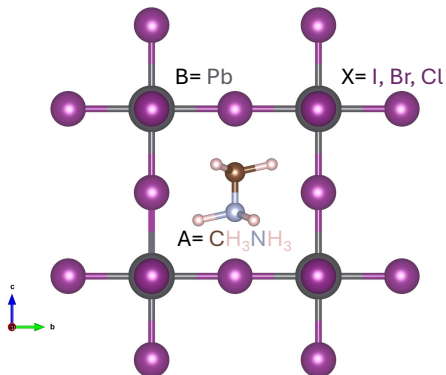


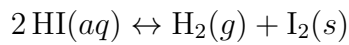
Figure 1.7: Cubic phase perovskite structure of  $\text{CH}_3\text{NH}_3\text{PbX}_3$  where the X-site is a halide anion.

the effective mass and hence their mobility.<sup>121</sup> The strong absorption properties of lead halide perovskites are also a result of its electronic structure. The possession of a direct bandgap and high density of states at the CBM results in a higher joint density of states (JDOS). Generally, organic molecules such as methylammonium ( $\text{MA}^+$ ) or formamidinium ( $\text{FA}^+$ ) are used as the A-site cation as they enhance the structural stability of the perovskite framework. Intrinsically, the housing of the A-site cation can determine the phase stability of the perovskite as they stabilise the structure, preventing tilting and rotations of the corner sharing octahedra resulting in an increased octahedral factor. The ability to produce crystalline thin films through solution processable approaches has allowed hybrid devices to excel in comparison to fully inorganic devices.<sup>122</sup> Evidently, perovskite materials are extremely versatile given the substantial degrees of freedom in the composition, however, they have four fundamental drawbacks associated with them. These include; poor environmental stability, charged ionic motion resulting in hysteresis, lead toxicity and problematic doping.<sup>123</sup>

### 1.2.6 Challenges in Perovskite Materials

#### Instability

Many HOIP materials including  $\text{MAPbI}_3$  exhibit instabilities arising from their ‘soft’ nature as a result of primarily being formed of ionic bonds. The low temperature processing of  $\text{MAPbI}_3$  is a result of the low formation energy, which also makes  $\text{MAPbI}_3$  susceptible to rapid degradation under environmental conditions, in particular; oxygen and moisture, UV radiation, elevated temperatures and electric bias.<sup>124–126</sup>  $\text{MAPbI}_3$  is highly sensitive to oxygen and moisture and when in contact tends to hydrolyse resulting in the formation  $\text{PbI}_2$ ,  $\text{CH}_3\text{NH}_2$  and  $\text{HI}$  which can be seen in the reactions below:<sup>124,127</sup>



These degradation processes result in the formation of photo-inactive phases resulting in reductions in PCE. Under illumination, Ruan et al.<sup>128</sup> observed  $\text{MAPbI}_x\text{Br}_{3-x}$  display a two step degradation process comprised of an initial reversible phase segregation before an irreversible phase segregation of iodine domains which increased with the intensity of illumination. It was also found the presence of 1% v/v oxygen concentration can substantially increase this degradation process. The presence

of oxygen generates free radicals which interact with organic molecules and causes degradation to  $\text{PbI}_2$ .<sup>129</sup> Elevated temperatures can also induce degradation which can be problematic during annealing processing. Abdelmageed et al.<sup>130</sup> showed that  $\text{MAPbI}_3$  films in an inert atmosphere can start to degrade at temperatures above 75 °C under illumination and at 95 °C in dark conditions. For the illuminated sample, it was found that a combination thermal and photo-dissociation resulted in degradation to metallic Pb and  $\text{PbI}_2$ , whereas the dark sample only degraded to  $\text{PbI}_2$ . The stability of halide perovskites can be improved by methods such as encapsulation, however in reality the intrinsic properties of  $\text{MAPbI}_3$  will need to be deeply understood to fully harness the potential of halide perovskites.

## Hysteresis

Hysteresis is a phenomenon seen in many dissipative devices where there is a delay between the change in material properties under an electric field.<sup>131</sup> Hysteresis results in a difference in  $J_{sc}$  values between forward and reverse scans and is generally believed to be due to; unbalanced charge transport/extraction, ion and vacancy migration and the trapping/detrapping of charges.<sup>41,131</sup> When hysteresis is displayed in a J-V curve in solar cells, it is generally undesirable as is a common sign of instability from ion migration and charge trapping/detrapping which can ultimately result in uncertainties in PCE. An illustration of this hysteresis can be viewed in Figure 1.8.<sup>2</sup>

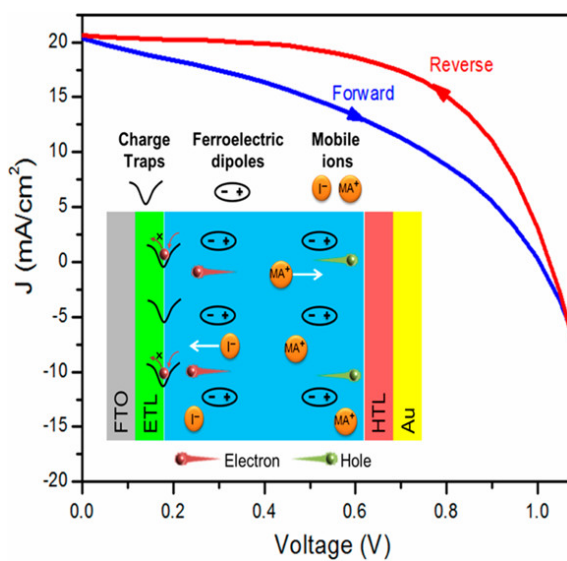


Figure 1.8: A J-V curve depicting the changes in current density as a function of applied electric field for a forward and reverse scan. Figure reproduced from Ref. 2.

### Lead Toxicity

Lead toxicity remains a significant issue which limits the scalability of perovskites due to the toxic nature of lead and the solvents used during solution processing.<sup>132,133</sup> To date, the best performing perovskite solar cells include Pb salts which are relatively soluble in water and are harmful to human health.<sup>134</sup> Although, there is some debate to the extent of Pb toxicity in small quantities, it can be agreed that a future without the use of Pb in photovoltaics is desirable. Efforts have been made to produce Pb free devices by using non-toxic replacement cations and the use of green solvents.<sup>135</sup> Pb can be replaced by either homovalent Sn, Ge or heterovalent Bi, Sb to ensure charge neutrality. For the case of a heterovalent substitute, a mixture of cations in the form of  $A_2B(I)B(III)X_6$  can be used or alternatively the use of vacancies be used within the in the form of an  $A_3B(III)_2X$  or  $A_2B(IV)X_6$  structure.<sup>136</sup> Exchanging for a homovalent element generally results in reductions in efficiency and stability. An example of this is the oxidation of  $Sn^{2+}$  forming  $Sn^{4+}$  which causes *p*-type self doping.<sup>137</sup>

## Doping

The term doping in halide perovskites refers to the addition of impurities to improve optoelectric properties or to control stability and crystal growth. Impurities in halide perovskites can be introduced by three mechanisms; intrinsic defect doping, extrinsic defect doping and charge transfer doping.<sup>138</sup> These mechanisms are done to improve free charge carrier generation or to shift the Fermi level.<sup>138</sup> However, doping can result in further instability in the crystal lattice by perturbing the crystal structure as a result of the ‘soft’ perovskite lattice. The ionic nature of halide perovskites also makes doping more challenging, resulting in extra precautions having to be taken when incorporating dopants into the crystal lattice.

### 1.2.7 Ruddlesden-Popper Perovskites

Ruddlesden-Popper perovskites are a quasi-2D perovskite formed when the A-site cation is too large to be accommodated in the octahedra and forms an inorganic 2D sheet housed between an organic spacer. These are held together by van der Waals interactions in the hydrogen bonds, improving stability and tuneability. These perovskites take the form of  $A_{n+1}B_nX_{3n+1}$  or  $A_{n-1}A'_2B_nX_{3n+1}$ .<sup>139,140</sup> Generally A is an organic/inorganic cation, A' is a large organic spacer cation, B is a transition metal and X is an anion. These formations can be produced in chalcogenide based perovskites when the A-site cation is too large and open up another route for material discovery.

# 2

## Chalcogenide Perovskites

### Contents

---

<b>2.1</b>	<b>Experimental Reports of Chalcogenide Perovskites . . . . .</b>	<b>28</b>
<b>2.2</b>	<b>Tolerance and Octahedral Factors . . . . .</b>	<b>31</b>
<b>2.3</b>	<b>Computational Reports of Chalcogenide Perovskites . . . . .</b>	<b>32</b>
<b>2.4</b>	<b>Chalcogenide Perovskite Properties . . . . .</b>	<b>45</b>
2.4.1	Stability . . . . .	45
2.4.2	Chemical Properties . . . . .	48
2.4.3	Optoelectronic Properties . . . . .	50
2.4.4	Defect Chemistry and Doping . . . . .	51
<b>2.5</b>	<b>Synthesis Methods . . . . .</b>	<b>53</b>
<b>2.6</b>	<b>Hybrid Chalcogenide Perovskites . . . . .</b>	<b>56</b>

---

Chalcogenide materials are compounds containing group 16 elements; O<sup>2-</sup>, S<sup>2-</sup>, Se<sup>2-</sup> or Te<sup>2-</sup>. Chalcogenides have already been used successfully in photovoltaic devices such as previously mentioned CIGS and CdTe. More recently, a new class of chalcogenide based perovskite materials with the ABX<sub>3</sub> structure where X = S, Se, are being developed to combine the unique properties of chalcogenide materials within an ABX<sub>3</sub> perovskite structure in pursuit of discovering of a highly stable and defect tolerant family of materials which exhibit desirable optoelectronic properties.<sup>14</sup> Chalcogenide perovskites are most commonly comprised of group II–IV–VI<sub>3</sub>

compounds where II= Ba, Sr, Ca; IV= Zr, Hf, Ti; VI= S, Se. Other forms of chalcogenides that are found include III<sub>1</sub>–III<sub>2</sub>–VI<sub>3</sub> compounds where III<sub>1</sub> and III<sub>2</sub> = lanthanides, Y, Sc; VI= S, Se and more recently computational reports of group I–V–VI<sub>3</sub> where I = monovalent alkali metal or molecular cation; V= Nb, V, Ta, Ge, Bi, Sb; VI = S, Se.<sup>7,14</sup> Chalcogenide perovskites have only recently been developed for photovoltaic applications, however already satisfy many of the optoelectronic parameters for high efficiency devices for both single junction and tandem application. Chalcogenide perovskites are a unique class of materials as they display both covalent and ionic bonding with an ionicity in between a classic semiconductor and halide perovskite.<sup>3,141,142</sup> Chalcogenides in the ABX<sub>3</sub> form can take many different motifs based on the relative positioning of the BX<sub>6</sub> octahedra. To be considered a true perovskite these polytypes must exhibit a corner-sharing octahedral cage. Perfect cubic structures such as the SrTiO<sub>3</sub> (*Pm* $\bar{3}$ *m*) prototype are rare to find in chalcogenide perovskites.<sup>14</sup> Instead, they are more commonly found as distorted perovskites taking the GdFeO<sub>3</sub> (*Pnma*) and the YScS<sub>3</sub> (*Pnm*2<sub>1</sub>) polytypes.<sup>14</sup> Other structures can be formed although they are considered non-perovskite as they do not exhibit corner sharing octahedra, they instead preferentially form a face or edge sharing BX<sub>6</sub> octahedra configuration. The non-perovskites in this group include the orthorhombic “needle-like” NH<sub>4</sub>CdCl<sub>3</sub>-type (*Pnma*), the hexagonal BaNiO<sub>3</sub>-type (*P6*<sub>3</sub>/*mmc*), the orthorhombic UFeS<sub>3</sub>-type (*Cmcm*) and the monoclinic CeTmS<sub>3</sub>-type (*P2*<sub>1</sub>/*m*).<sup>14</sup> These structures can be seen in Figure 2.1. The distorted orthorhombic perovskites such as GdFeO<sub>3</sub> and YScS<sub>3</sub> are formed when the A-site cation is too small to fit inside the B-site interstices, rotating the octahedral cage and distorting the perovskite structure slightly away from the cubic structure.<sup>14</sup> Nevertheless, these distorted phases can still be used as effective solar absorbers due to their corner-sharing octahedra, fundamental to forming a direct bandgap, for example BaZrS<sub>3</sub>.<sup>14,143</sup> A hexagonal perovskite phase can form when too large of an A-site cation is used, resulting in a large lattice strain causing a face-sharing BX<sub>6</sub> octahedra to form, as seen

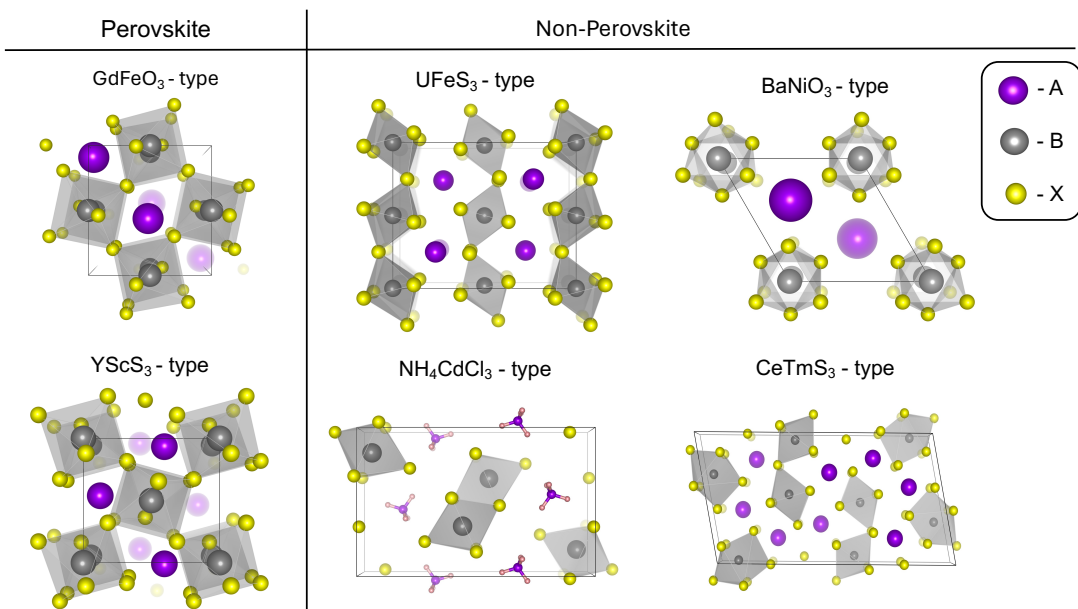


Figure 2.1: Most common polytypes of  $\text{ABX}_3$  chalcogenides.

in compounds such as  $\text{BaNiO}_3$  ( $P6_3/mmc$ ).<sup>144</sup> An orthorhombic “needle-like” phase can form when the A-site cation is very small, forming structures like  $\text{NH}_4\text{CdCl}_3$  ( $Pnma$ ).<sup>145</sup> Both hexagonal and “needle-like” phases display localised conduction and poor carrier mobility making them undesirable for photovoltaics.<sup>146</sup> The phase formation of these chalcogenides can be predicted using the Goldschmidt ( $t$ ) and octahedral factor ( $\mu$ ) as mentioned in Equations 1.7-1.8.

The following sections contain a comprehensive review on chalcogenide perovskites and their future prospects. This section will summarise the most important experimental and computational reports to give an insight on the current chalcogenide perovskites which exist and that have been synthesised. It will primarily focus on  $\text{ABX}_3$  compounds with  $\text{X} = \text{S}, \text{Se}$ . This being due to oxide perovskites producing too large of bandgaps making them unsuitable for solar cells while tellurium is omitted due to scarcity and has not predicted to be stable computationally.<sup>14,145</sup> Therefore, chalcogenide perovskites as solar absorbers in literature are almost exclusively those containing  $\text{S}^{-2}, \text{Se}^{-2}$  as these X-site anions due to the fact they have a raised valence band, narrowing the bandgap to the visible range, making them

suitable for photovoltaic application.<sup>147</sup>

## 2.1 Experimental Reports of Chalcogenide Perovskites

Chalcogenide perovskites were first synthesised in 1957 by Hahn and Mutschke<sup>62</sup> but still remain a relatively unexplored research area which is only beginning to be investigated in part due to the success of halide perovskites. Among the family of sulphur based chalcogenide perovskites, BaZrS<sub>3</sub> has been at the forefront of research as it possesses many desirable properties for a solar cell including; a bandgap of 1.75–1.94 eV,<sup>8,16,148–150</sup> an extraordinary absorption coefficient<sup>16</sup> and being highly stable in environmental conditions.<sup>8</sup> BaZrS<sub>3</sub> has also been widely reported to crystallise in the GdFeO<sub>3</sub>-type phase.<sup>8,16,62,141,147,151–155</sup> Similar chalcogenides such as BaHfS<sub>3</sub> has also been reported experimentally to crystallise as GdFeO<sub>3</sub>-type perovskite.<sup>16,154,156</sup> Above 980 °C, SrZrS<sub>3</sub> exhibits a GdFeO<sub>3</sub>-type structure which has been reported in multiple studies.<sup>16,147,154,155,157</sup> Below 980 °C, SrZrS<sub>3</sub> forms a NH<sub>4</sub>CdCl-type structure.<sup>157</sup> Similarly, EuZrS<sub>3</sub> forms a GdFeO<sub>3</sub>-type structure at high synthesis temperatures and a NH<sub>4</sub>CdCl-type structure at lower temperatures.<sup>154,158</sup> At high synthesis temperatures, SrHfS<sub>3</sub> and EuHfS<sub>3</sub> both form GdFeO<sub>3</sub>-type structures also.<sup>154,159</sup> Both CaZrS<sub>3</sub> and CaHfS<sub>3</sub> have been reported to form a GdFeO<sub>3</sub>-type perovskite, although only at high growth temperatures of 1050 °C.<sup>141,152,154</sup> Both BaTiS<sub>3</sub> and SrTiS<sub>3</sub> form a disordered hexagonal BaNiO<sub>3</sub> structure, unsuitable for photovoltaic application.<sup>9,62,152,155,160</sup> However, a computational report by Meng et al.<sup>161</sup> predicted that the addition of Ti could be an effective alloy in BaZr<sub>1-x</sub>Ti<sub>x</sub>S<sub>3</sub> ( $x \leq 0.25$ ) under near stoichiometric growth conditions. This was then confirmed by Wei et al.<sup>151</sup> who synthesised Ba(Zr<sub>0.96</sub>Ti<sub>0.04</sub>)S<sub>3</sub>, reducing the bandgap from 1.78 eV to 1.51 eV. This improved the theoretical PCE from 28% to 32% by shift-

ing the bandgap down to a more optimal energy potential. The inclusion of 4% Ti results in the lowering of the CBM, reducing the bandgap. However, a Ti concentration above 5% results in the formation of unstable secondary phases.<sup>151</sup> Group III<sub>1</sub>–III<sub>2</sub>–S<sub>3</sub> perovskite structures such as the prototype YScS<sub>3</sub> are another another type of chalcogenide perovskites where III<sub>1</sub>= Lanthanide, Y; III<sub>2</sub>= Ti, V, Cr, Mn, Fe, Co and Ni. Unfortunately, most produced non-perovskite phases.<sup>162–165</sup> One exception is LaLuS<sub>3</sub> which forms a YScS<sub>3</sub> phase.<sup>14</sup> In the case of selenium based perovskites, there are much fewer experimentally stable examples. Those of which that have shown a GdFeO<sub>3</sub>-type structure have all contained uranium; Rh<sub>2</sub>U<sub>6</sub>Se<sub>15</sub>, Cs<sub>2</sub>Ti<sub>2</sub>U<sub>6</sub>Se<sub>15</sub>, Cs<sub>2</sub>Cr<sub>2</sub>U<sub>6</sub>Se<sub>15</sub> and BaUSe<sub>3</sub>,<sup>166,167</sup> making them inadmissible candidate materials for solar application. Furthermore, compounds such as SrZrSe<sub>3</sub>, SrHfSe<sub>3</sub> and EuZrSe<sub>3</sub> all form non-perovskite NH<sub>4</sub>CdCl<sub>3</sub>-type phases.<sup>158,168,169</sup> It was reported in 1964 that BaZrSe<sub>3</sub> forms a hexagonal polytype, then in 1997 Tranchitella et al.<sup>168</sup> determined BaZrSe<sub>3</sub> forms non stoichiometrically in the hexagonal phase. Although the phase reported were controversial it was agreed that BaZrSe<sub>3</sub> does not form a corner-sharing perovskite phase. There is some debate on the phase formation of BaHfSe<sub>3</sub> as Moroz<sup>170</sup> reported a perovskite GdFeO<sub>3</sub> phase, however a review paper by Sopiha et al.<sup>14</sup> believes this is unlikely and that it is more likely oxygen contaminated the sample and it is more likely to form a non-stoichiometric hexagonal phase similar to BaZrSe<sub>3</sub>. Experimental reports shows that chalcogenide perovskites that can be used for solar cells (GdFeO<sub>3</sub>-type and YScS<sub>3</sub>-type) are very rare to come across in the ground state. Table 2.1 summarises these experimentally known inorganic perovskites. The bandgaps for experimentally stable perovskites can also be seen in table 2.2. Among these, the  $\beta$  phases of SrZrS<sub>3</sub> and SrHfS<sub>3</sub> only form in a GdFeO<sub>3</sub> at temperatures above 900 °C. Those containing Ca can be produced as a distorted perovskite but also require higher growth temperatures.

Table 2.1: Phases of experimentally reported chalcogenide crystal structures. Those in bold have had multiple phases reported.

GdFeO <sub>3</sub>	YScS <sub>3</sub>	NH <sub>4</sub> CdCl <sub>3</sub>	BaNiO <sub>3</sub>	UFeS <sub>3</sub>	CeTmS <sub>3</sub>	Off-Stoichiometry
BaHfS <sub>3</sub> <sup>16,154,156</sup>	CeScS <sub>3</sub> <sup>14</sup>	BaSnS <sub>3</sub> <sup>171</sup>	BaTaS <sub>3</sub> <sup>14</sup>	<b>BaVS<sub>3</sub></b> <sup>172</sup>	CeHoS <sub>3</sub> <sup>173</sup>	BaNbSe <sub>3</sub> <sup>174</sup>
BaUS <sub>3</sub> <sup>154</sup>	DyScS <sub>3</sub> <sup>14</sup>	EuZrS <sub>3</sub> <sup>175</sup>	<b>BaTiS<sub>3</sub></b> <sup>62,152,155,160</sup>	CeLuS <sub>3</sub> <sup>14</sup>	CeTmS <sub>3</sub> <sup>14</sup>	<b>BaTaSe<sub>3</sub></b> <sup>176</sup>
BaZrS <sub>3</sub> <sup>16,62,152,154,155</sup>	ErScS <sub>3</sub> <sup>14</sup>	EuZrSe <sub>3</sub> <sup>158</sup>	<b>BaVS<sub>3</sub></b> <sup>172</sup>	CeYbS <sub>3</sub> <sup>14</sup>	LaYS <sub>3</sub> <sup>177</sup>	<b>BaTiS<sub>3</sub></b> <sup>14</sup>
CaHfS <sub>3</sub> <sup>154</sup>	<b>LaYbS<sub>3</sub></b> <sup>178</sup>	PbHfS <sub>3</sub> <sup>14</sup>	<b>BaTaSe<sub>3</sub></b> <sup>179</sup>	CeYbSe <sub>3</sub> <sup>180</sup>		<b>BaZrSe<sub>3</sub></b> <sup>168</sup>
CaSnS <sub>3</sub> <sup>181</sup>	NdScS <sub>3</sub> <sup>14</sup>	PbZrS <sub>3</sub> <sup>182</sup>	BaTiSe <sub>3</sub> <sup>179</sup>	<b>LaYbS<sub>3</sub></b> <sup>178,180</sup>		PbTiS <sub>3</sub> <sup>183</sup>
CaZrS <sub>3</sub> <sup>154</sup>	PrScS <sub>3</sub> <sup>14</sup>	SnHfS <sub>3</sub> <sup>184</sup>	BaVSe <sub>3</sub> <sup>185</sup>	LaYbSe <sub>3</sub> <sup>180</sup>		PbVS <sub>3</sub> <sup>186</sup>
EuHfS <sub>3</sub> <sup>154</sup>	SmScS <sub>3</sub> <sup>14</sup>	SnSnS <sub>3</sub> <sup>187</sup>	<b>BaZrSe<sub>3</sub></b> <sup>14</sup>	NdLuS <sub>3</sub> <sup>14</sup>		SnNbS <sub>3</sub> <sup>188</sup>
SrHfS <sub>3</sub> <sup>16,156</sup>	TbScS <sub>3</sub> <sup>14</sup>	SnZrS <sub>3</sub> <sup>14</sup>	SrTiS <sub>3</sub> <sup>155</sup>	NdLuSe <sub>3</sub> <sup>173</sup>		
<b>SrZrS<sub>3</sub></b> <sup>16,154</sup>	<b>GdScS<sub>3</sub></b> <sup>189</sup>	SrHfSe <sub>3</sub> <sup>16,154</sup>	SrTiSe <sub>3</sub> <sup>190</sup>	NdYbS <sub>3</sub> <sup>14</sup>		
UCrS <sub>3</sub> <sup>14</sup>	HoScS <sub>3</sub> <sup>14</sup>	SrSnS <sub>3</sub> <sup>155,171</sup>		NdYbSe <sub>3</sub> <sup>180</sup>		
<b>GdScS<sub>3</sub></b> <sup>14</sup>	LaLuS <sub>3</sub> <sup>14</sup>	<b>SrZrS<sub>3</sub></b> <sup>141,157</sup>		PrLuS <sub>3</sub> <sup>14</sup>		
UNiS <sub>3</sub> <sup>191</sup>	LaScS <sub>3</sub> <sup>14</sup>	SrZrSe <sub>3</sub> <sup>168</sup>		PrLuSe <sub>3</sub> <sup>14</sup>		
URhS <sub>3</sub> <sup>14</sup>	YScS <sub>3</sub> <sup>14</sup>	PbSnS <sub>3</sub> <sup>171</sup>		PrYbS <sub>3</sub> <sup>14</sup>		
UVS <sub>3</sub> <sup>14</sup>				PrYbSe <sub>3</sub> <sup>14</sup>		
CeSc <sub>3</sub> <sup>14</sup>				SmYbSe <sub>3</sub> <sup>180</sup>		

Table 2.2: Experimentally verified chalcogenide perovskites (where X= S, Se) with bandgaps determined. Adapted from Ref. 13 and 14.

Compound/Alloy	Bandgap (eV)
BaZrS <sub>3</sub>	1.75, <sup>8</sup> 1.79, <sup>148</sup> 1.82, <sup>149</sup> 1.89, <sup>150</sup> 1.94 <sup>16</sup>
BaHfS <sub>3</sub>	2.06, <sup>156</sup> 2.17 <sup>16</sup>
SrZrS <sub>3</sub> ( $\beta$ phase)	2.05, <sup>147</sup> 2.14 <sup>16</sup>
SrHfS <sub>3</sub> ( $\beta$ phase)	2.32, <sup>156</sup> 2.41 <sup>16</sup>
BaZr(S <sub>0.6</sub> Se <sub>0.4</sub> ) <sub>3</sub>	1.76 <sup>16</sup>
BaZr <sub>1-x</sub> Ti <sub>x</sub> S <sub>3</sub>	1.51( $x=0.04$ ), <sup>8</sup> 1.63( $x=0.05$ ) <sup>16</sup>
CaSnS <sub>3</sub>	1.72 <sup>192</sup>
CaZrS <sub>3</sub>	1.90 <sup>141</sup>
LaYS <sub>3</sub>	2.0 <sup>177</sup>

## 2.2 Tolerance and Octahedral Factors

2

The Goldschmidt tolerance factor and octahedral are empirical parameters that are designed to predict the stability of perovskite based on their phase formation relative the radii of the A, B and X-site ions. Table 1.1 can be used as a guideline to assess what phase will be formed for particular values. One shortcoming of the standard Goldschmidt tolerance factor equation,  $t = \frac{R_A + R_X}{\sqrt{2}(R_B + R_X)}$  and octahedral factor  $\mu = \frac{R_B}{R_X}$  is that it was intended for the use of oxide perovskites. As oxygen is a small anion with radius 1.40 Å there is a considerable variety of B and X-site cations which satisfy both  $t$  and  $\mu$ . This is why over 90% of metal ions are stable in an  $\text{ABO}_3$  perovskite structure according to these parameters.<sup>193</sup> In the case of sulphur and selenium which have much larger radii (1.84 Å and 1.98 Å, respectively) there are two consequences.<sup>194</sup> Firstly, a larger A-site atom is required to satisfy  $t$  and secondly the B-Site cation needs to be increased to stabilise the octahedral cage and keep  $\mu > 0.41$ . The first issue is easily overcome by placing a larger cation or molecule in the A-site, however to amend the second point is more arduous, as there are few options of B-site cations which keeps  $\mu$  above the critical value of 0.41. For selenides, the ability to produce a desirable  $\mu$  value is hindered further. For these reasons there has been many attempts to modify the  $t$  to be more suited to S and Se perovskites by including electronegativity differences within the equation, or to include alloying in the expression.<sup>193,195</sup> Further difficulties with the tolerance factor occur while using an organic molecule in the A-site, as it is difficult to estimate the ionic radii of molecular cations due to varying bond-lengths from the addition of hydrogen bonds. Therefore to calculate the effective radii of a molecular cation,  $R_A$ , the following equation is used:<sup>196,197</sup>

$$R_A = R_{\text{mass}} + R_{\text{ion}} \quad (2.1)$$

where  $R_{\text{mass}}$  is the distance between the centre of mass of the molecule and the atom with the greatest distance from the centre of mass, excluding hydrogen, while  $R_{\text{ion}}$  is the corresponding ionic radius of such atom.

## 2.3 Computational Reports of Chalcogenide Perovskites

There are 3744 possible combinations of inorganic chalcogenide materials which can satisfy an  $\text{ABX}_3$  framework, therefore high throughput material screening is necessary to omit non-perovskite structures, unsuitable for photovoltaic devices. Material selection is therefore a vital step in discovering suitable chalcogenide solar absorbers. In this section, we will summarise the most influential papers that relate to this report. This will include computational reports on organic and inorganic chalcogenide perovskites to identify suitable A, B and X-site combinations for use in hybrid chalcogenide perovskites. This will be done by identifying properties of various materials through parameters such as; the Goldschmidt tolerance factor, the octahedral factor, ionic radii, phase formations, thermodynamic and dynamic stability as well as the optoelectronic properties. Through these measures it is possible to identify candidate compounds that have the possibility to be used in hybrid chalcogenide photovoltaics.

In 2009, Bennett et al.<sup>198</sup> reported on the ground-state atomic structure, the electronic structure and dielectric response of  $\text{BaZrS}_3$  using Density Functional Theory (DFT). It was found that there is a stronger covalent bonding character

in BaZrS<sub>3</sub> compared to BaZrO<sub>3</sub>, reducing the ionic contribution to the dielectric constant to a value of 36 in BaZrS<sub>3</sub> compared to 48 in BaZrO<sub>3</sub>. However, it was found that the high frequency dielectric constant increased from 4.9–9.6 in BaZrS<sub>3</sub>. The electronic structure of BaZrS<sub>3</sub> was also calculated using PDOS characterisation which showed greater mixing of Ba and Zr with S states compared to BaZrO<sub>3</sub>. The VBM of BaZrS<sub>3</sub> was found to be primarily comprised of S 3p-states while the conduction band minimum shows a covalent nature between unfilled Zr 4d-states and empty S 3d-states, effectively lowering the CBM energy which reduces the bandgap to 1.7 eV compared to 3.9 eV in BaZrO<sub>3</sub>.<sup>198</sup> This report demonstrates why oxides are not suitable for photovoltaic applications and chalcogens such as S exhibit more suitable bandgaps for solar cells.

In 2014, Brehm et al.<sup>195</sup> used DFT within the Local Density Approximation (LDA) framework to obtain the ground state structures of 20 ABS<sub>3</sub> compounds where A= K, Rb, Cs, Ca, Sr, Ba, Tl, Sn, Pb, Bi and B = Sc, Y, Zr, V, Nb. For each compound, the formation energy of 22 different phases were calculated which included; five corner-sharing, four edge-sharing and six face-sharing BX<sub>6</sub> structures. The final seven phases were mixed motif phases. For the lowest energy phases, the entropy contribution to the Gibbs free energy was calculated. These calculations demonstrated that GdFeO<sub>3</sub>-type phases exhibit higher vibrational entropy compared to NH<sub>4</sub>CdCl<sub>3</sub>-type perovskites. The phonon normal mode frequencies were then calculated at the  $\Gamma$ -point to determine the ground state phase stability of the each structure using the equation:

$$F_{vib,solid} = \sum_{s=1}^{3N} \left\{ \frac{\hbar\omega_s}{2} + k_B T \ln \left[ 1 - \exp \left( \frac{-\hbar\omega_s}{k_B T} \right) \right] \right\} \quad (2.2)$$

where  $N$  represents the number of atoms in the system,  $\omega_s$  represents a  $\Gamma$ -point normal mode frequency in the harmonic approximation,  $k_B$  is the Boltzmann constant, and  $T$  is temperature in degrees Kelvin. The calculated ground state

energies showed that none of the combinations had a preferential corner sharing perovskite structure. This is contradictory to other literature as it is well known that BaZrS<sub>3</sub> does exhibit a corner-sharing GdFeO<sub>3</sub>-type structure. This is likely due to the usage a less accurate functional (LDA). Nevertheless, this report calculates the lowest ground state energies for 22 different phases - much more than standard in literature. The ability to measure stability across numerous phases widens the range of likelihood of calculating the true ground state energy and not being limited to a local minima energy. In other words, as the number of phases analysed is increased, the propensity that the compound is in its true ground state is also increased.

One of the most significant papers on chalcogenide perovskite compounds was published in 2015 by Sun et al.<sup>3</sup> who predicted the optical properties of ABX<sub>3</sub> structures where A= Ca, Sr, Ba; B= Ti, Zr, Hf; X= S, Se using first principles calculations. This report differs to that of Bennett et al.<sup>198</sup> which focuses on structural characterisation rather than screening material properties for photovoltaic application. Sun et al.<sup>3</sup> used DFT implemented in the Vienna Ab initio Simulation Package (VASP) program to calculate the bandgaps of 18 different ABX<sub>3</sub> compounds under different phases, seen in Figure 2.2. Compounds in the distorted perovskite structures generally have the widest bandgaps, followed by “needle-like” phases and finally hexagonal phases. The VBM was found to consist primarily of chalcogen *p*-orbitals while the CBM was predominantly comprised of the B-site transition metal *d*-orbitals. This resulted in sulphide based compounds having a larger bandgap by  $\approx 0.5\text{--}0.6\text{ eV}$  greater than selenides in the distorted and “needle-like” phases due to the lower energy levels of the 3*p* S orbitals compared to the 4*p* Se orbitals. It is also clear that Hf based compounds exhibit higher bandgaps than corresponding Zr compounds due to the higher energy of 5*d* Hf orbitals in comparison to the 4*d* Zr orbitals.<sup>3</sup> The ability to alter the bandgap based on the B and X-site atoms allows for flexibility when selecting organic cations for this report. Although many “needle-like” phases have optimal bandgaps for solar applications, it was found that

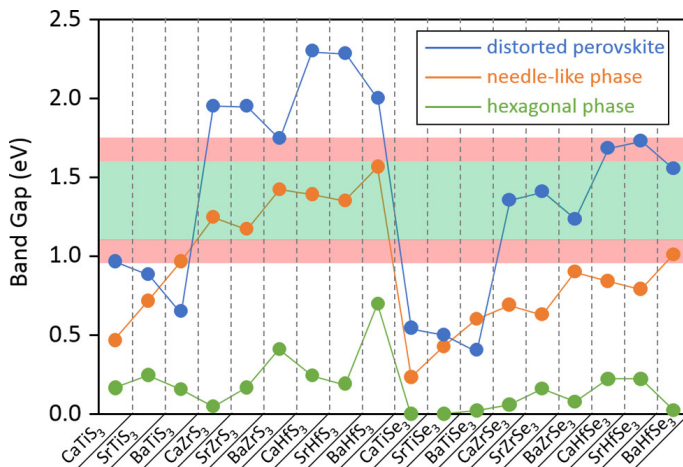


Figure 2.2: Bandgap of 18  $ABX_3$  compounds in the distorted perovskite, “needle-like”, and hexagonal phases calculated with the HSE06 functional. The optimal band gap region for solar-cell materials is highlighted in light green. An extended region for theoretical efficiencies above 28% is highlighted in light red. Figure reproduced from Ref. 3.<sup>4</sup>

the absorption onset was much higher than their fundamental bandgaps indicating a pseudo-direct bandgap, making them unsuitable for thin film applications.<sup>3</sup> Considering this, the remaining suitable compounds (within the light red and green region of Figure 2.2) which exhibit a distorted perovskite structure were;  $\text{CaTiS}_3$ ,  $\text{BaZrS}_3$ ,  $\text{CaZrSe}_3$ ,  $\text{SrZrSe}_3$ ,  $\text{BaZrSe}_3$ ,  $\text{CaHfSe}_3$ ,  $\text{SrHfSe}_3$  and  $\text{BaHfSe}_3$ . To further screen these compounds Sun et al.<sup>3</sup> calculated the formation energies for each compound relative to the ideal perovskite phase seen in table 2.3.

Among the compounds with suitable bandgaps,  $\text{BaZrS}_3$ ,  $\text{CaZrSe}_3$  and  $\text{CaHfSe}_3$  are most stable in the distorted perovskite phase while  $\text{CaTiS}_3$  is within 45 meV/f.u. of the most stable phase, meaning under careful synthesis conditions a distorted perovskite phase could be formed.  $\text{BaZrS}_3$  has been experimentally shown to form a distorted perovskite phase as seen in table 2.1. For the compounds with Ca in the A-site, there are no stable compounds that have been synthesised as of yet, although there has been attempts by Tranchitella et al.<sup>168</sup> and Moroz<sup>170</sup> whom attempted to synthesise  $\text{CaZrSe}_3$  and  $\text{CaHfSe}_3$ , respectively, but were both unsuccessful. During the synthesis of  $\text{CaZrSe}_3$ , it was noted that a binary mixture of  $\text{CaSe}$  and  $\text{ZrSe}_2$

Table 2.3: Calculated formation energy (eV/f.u.) for  $\text{ABX}_3$  compounds in the distorted perovskite, “needle-like” and hexagonal phases relative to the perfect perovskite phase.

Materials in bold are most stable in the distorted perovskite phase or are within 45 meV/f.u. of the most stable phase. Table reproduced from Ref. 3.

Compound	Distorted	Needle-like	Hexagonal
<b>CaTiS3</b>	-1.120	-1.160	-0.285
SrTiS3	-0.436	-0.531	-0.216
BaTiS3	-0.022	0.049	-0.183
<b>CaZrS3</b>	-1.529	-1.512	-0.084
<b>SrZrS3</b>	-0.784	-0.829	0.029
<b>BaZrS3</b>	-0.200	-0.192	0.134
<b>CaHfS3</b>	-1.428	-1.381	-0.033
<b>SrHfS3</b>	-0.696	-0.731	0.054
<b>BaHfS3</b>	-0.143	-0.108	0.124
<b>CaTiSe3</b>	-1.325	-1.364	-0.540
SrTiSe3	-0.632	-0.775	-0.461
BaTiSe3	-0.102	-0.189	-0.390
<b>CaZrSe3</b>	-1.688	-1.661	-0.402
SrZrSe3	-0.959	-1.042	-0.295
BaZrSe3	-0.338	-0.433	-0.182
<b>CaHfSe3</b>	-1.615	-1.569	-0.360
SrHfSe3	-0.893	-0.976	-0.275
BaHfSe3	-0.285	-0.376	-0.189

was formed. This report gives an important insight to procedures used to investigate chalcogenide compounds for photovoltaic application and the importance of bandgap engineering which can be applied to hybrid organic-inorganic chalcogenide perovskites.

In 2017, Ju et al.<sup>5</sup> computed the bandgaps of 26 chalcogenide perovskites possessing either a cubic or pseudocubic structure with theoretical efficiencies greater than 25% ( $0.9 < E_g < 1.6$  eV). Each phase was determined by calculating the empirical Goldschmidt’s tolerance factor seen in Figure 2.3a. Of these perfect and distorted perovskites, the bandgap for each can be found in Figure 2.3b.

$\text{ABO}_3$  based perovskites are seen to exhibit bandgaps too wide for photovoltaic usage due the high electronegativity of oxygen as outlined by Bennett et al.<sup>198</sup>, which causes strong ionic bonding with the metal cation and a large energy difference in the VB and CB. The high electronegativity of oxygen is also related to a high difference in electron affinity and ionisation potential and hence a large bandgap that has poor

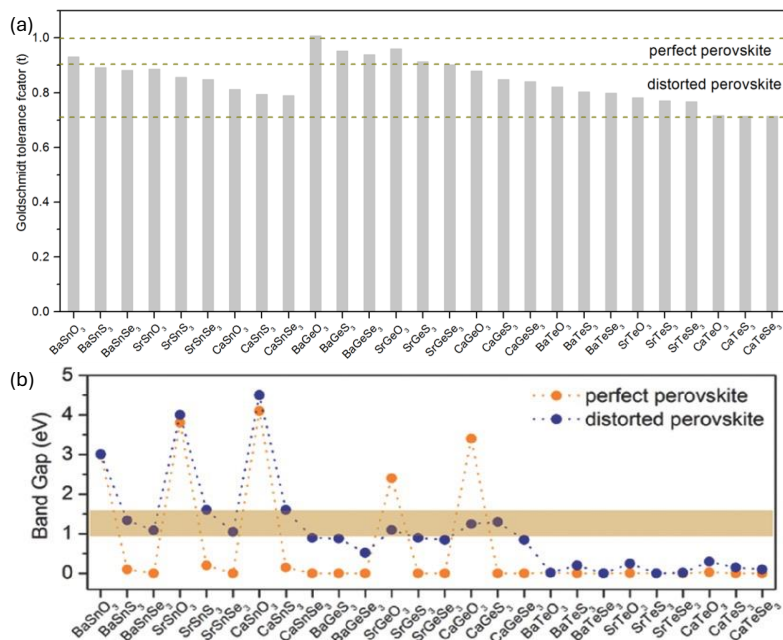


Figure 2.3: (a) Calculated Goldschmidt tolerance factor for chalcogenide perovskites. (b) Computed bandgaps of chalcogenide perovskites with the optimal bandgap located within the gold horizontal bar. Figure reproduced from Ref. 5.

charge transfer properties along the B-X bonds, causing oxides to have insulating properties.<sup>199</sup> None of the compounds displaying a perfect perovskite structure were shown to have an ideal bandgap, however eight of the distorted perovskites had a suitable bandgap, four of which are predicted to possess a direct bandgap; SrSnSe<sub>3</sub> (1.00 eV), CaGeO<sub>3</sub> (1.15 eV), SrSnS<sub>3</sub> (1.56 eV) and CaSnS<sub>3</sub> (1.58 eV). The optical absorption spectra of these compounds were computed against MAPbI<sub>3</sub> and Si seen in Figure 2.4a. SrSnSe<sub>3</sub> showed the strongest absorption within the visible range (1.59–3.26 eV). Further calculations were then completed on SrSnSe<sub>3</sub> including the electronic band structure (Figure 2.4b) and the density of states (Figure 2.4c).

It is seen that SrSnSe<sub>3</sub> has an absorption coefficient only slightly inferior to MAPbI<sub>3</sub> and possesses a CBM and VBM localised to the  $\Gamma$ -point. The VBM was shown to be mainly occupied by Se 4p-orbitals while the CBM consisted also of Se 4p-orbitals and Sn 5s-orbitals. SrSnSe<sub>3</sub> also showed impressive effective masses  $m_h^* = 0.12, 0.19, 0.31$  and  $m_e^* = 0.18, 0.19, 0.24$  in the [100], [110] and [111] directions, respectively.<sup>5</sup> These small effective masses indicate desirable charge transport

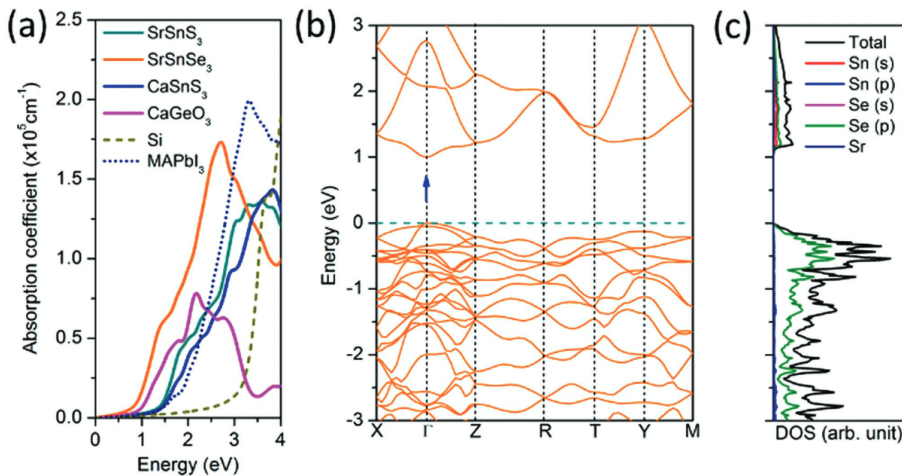


Figure 2.4: (a) Computed optical absorption spectra (calculated using HSE06) of several materials with distorted perovskite structure, compared to Si and MAPbI<sub>3</sub>. The absorption coefficient of MAPbI<sub>3</sub> is computed using the PBE functional without considering the SOC effect. (b) Computed band structure of SrSnSe<sub>3</sub>. (c) Computed PDOS of SrSnSe<sub>3</sub> with distorted perovskite structure. Figure reproduced from Ref. 5.

properties. SrSnSe<sub>3</sub> was also calculated to have a very low exciton binding energy of 9.6 meV, further alluding to promising transport properties. The main shortcoming of SrSnSe<sub>3</sub> is that the most stable phase is a “needle-like” phase followed by a distorted phase.<sup>5</sup> To achieve this distorted phase rather than a the “needle-like” phase, non-equilibrium thin film synthesis techniques can be implemented.<sup>200–202</sup> This can however increase complexity and the cost of production as elevated temperatures and pressures may be required. Overall, this paper gives an insight into candidates for B and X-site ions that are not used often in literature. In particular, the use of Sn can be used as an alternative to Zr and Hf and has a smaller ionic radii which will increase the variability of organic A-site cations that can be implemented in this report. Although the smaller radius can result in more deformation of the octahedral cage as the critical octahedral factor value becomes more difficult to satisfy.

In 2018, Filippone et al.<sup>203</sup> calculated the enthalpy of formation of distorted ABX<sub>3</sub> structures from binary chalcogenide compounds (AX and BX<sub>2</sub>), where A=Ca, Sr, Ba; B= Ti, Zr, Hf; X= S, Se. Using the PBEsol, it was found that BaTiS<sub>3</sub>, SrZrS<sub>3</sub>, BaZrS<sub>3</sub>, SrHfS<sub>3</sub>, BaHfS<sub>3</sub>, BaZrSe<sub>3</sub> and BaHfSe<sub>3</sub> all had negative enthalpy

of formation, meaning they would be stable with respect to the binary phases.<sup>14,203</sup> However, only BaHfS<sub>3</sub> and BaZrS<sub>3</sub> are reported to also have a negative ground state energy in the GdFeO<sub>3</sub>-type structure. Filippone et al.<sup>203</sup> also calculated that CaZrSe<sub>3</sub> and CaHfSe<sub>3</sub> had high positive enthalpy of formation values of 0.290 eV/f.u. and 0.293 eV/f.u., respectively. This may be an indication as to the reason why the synthesis attempts by Tranchitella et al.<sup>168</sup> and Moroz<sup>170</sup> resulted in the formation of binary phases and unsuccessful synthesis attempts.

In 2018, Huo et al.<sup>6</sup> conducted a high-throughput screening of 168 ABX<sub>3</sub> chalcogenide perovskites (A = Mg, Ca, Sr, Ba, Zn, Cd, Sn, Pb; B = Ti, Zr, Hf, Si, Ge, Sn, Pb; X = O, S, Se) as four different crystal structures (*Pm* $\overline{3}$ *m*, *Pnma*, *P6*<sub>3</sub>/*mmc* and *Pnma* “needle-like”). First-principles calculations based on DFT were carried out to obtain material properties including phase stability, thermodynamic stability, kinetic stability, effective masses and optical absorption values.<sup>6</sup> Based on these properties the most successful candidate materials were found to be BaZrS<sub>3</sub>, BaZrSe<sub>3</sub>, SrZrSe<sub>3</sub>, BaHfSe<sub>3</sub> and SrHfSe<sub>3</sub>. To come to this conclusion, ground state energies were calculated at zero temperature. 77 structures had ground state energies with a cubic (6), distorted orthorhombic (62) or hexagonal (9) perovskite structure. The formation energy of these 77 structures was then calculated using the PBE functional and any structures with a formation energy greater than 60 meV/atom were removed. The bandgaps of the 77 structures were also calculated using the PBE functional, which can underestimate the bandgaps, therefore compounds with a calculated bandgap of 0–1.1 eV were chosen for further analysis.<sup>4</sup> It was found that 20 structures had a suitable bandgap for photovoltaic application. The formations energies and bandgaps of the 77 structures can be seen in Figure 2.5a and the 20 structures with suitable bandgaps can be seen in Figure 2.5b.

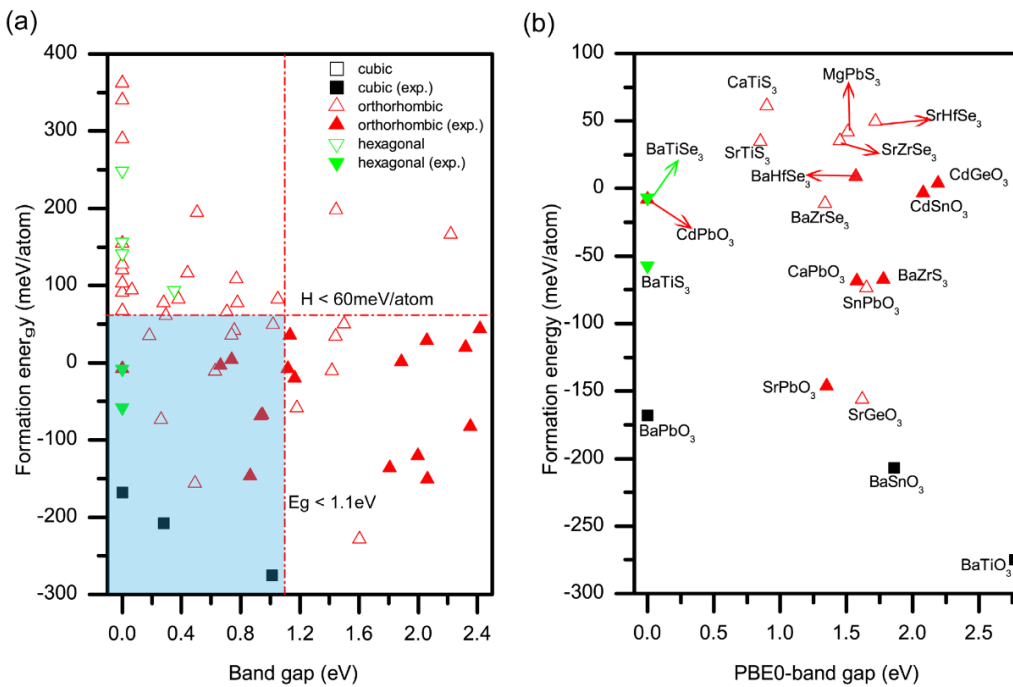


Figure 2.5: (a) Formation energies and PBE calculated band gaps of 77 types of perovskites. (b) Formation energies and PBE calculated band gaps of 20 stable perovskites. Solid symbols indicate that such a compound has been synthesised in experiments. Figure reproduced from Ref. 6.

These results give accurate descriptions of the formation energies as they correctly predicted the phase formation and stability's of CaPbO<sub>3</sub>, SrPbO<sub>3</sub>, CdGeO<sub>3</sub>, CdPbO<sub>3</sub>, CdSnO<sub>3</sub>, BaZrS<sub>3</sub> and BaHfSe<sub>3</sub>, all of which had been previously synthesised.<sup>204–209</sup> Following this, effective mass calculations were carried out. Orthorhombic effective masses are an average of the  $X$ ,  $Y$  and  $Z$  directions which can be seen in table 2.4. The six compounds outlined in bold have a suitable bandgap and effective masses less than the electron rest mass ( $m_0$ ). The optical absorption and theoretical efficiency of these six compounds; BaZrS<sub>3</sub>, BaHfSe<sub>3</sub>, MgPbS<sub>3</sub>, SrZrSe<sub>3</sub>, SrHfSe<sub>3</sub> and BaZrSe<sub>3</sub> were then calculated.

The strong absorption at the band edges in chalcogenide perovskites can be attributed to the  $p$ - $d$  transitions, differing from halide perovskites which rely on  $p$ - $p$  orbital transitions. The optical absorption coefficients can be seen in Figure 2.6a and the theoretical conversion efficiencies in Figure 2.6b with MAPbI<sub>3</sub> and

Table 2.4: PBE0-calculated band gap and effective mass. Materials in bold have both a optimal bandgap and an effective mass less than  $m_0$ . Table reproduced from Ref. 6 with only X= S, Se included.

Compound	$E_g^d$	$E_g^i$	$m_e/m_0$	$m_h/m_0$
BaTiS <sub>3</sub>	0	—	—	—
BaTiSe <sub>3</sub>	0	—	—	—
<b>MgPbS<sub>3</sub></b>	1.51	—	0.52	0.34
CaTiS <sub>3</sub>	0.90	—	0.39	0.26
SrTiS <sub>3</sub>	0.85	—	0.41	0.53
<b>BaZrS<sub>3</sub></b>	1.78	—	0.30	0.46
<b>BaZrSe<sub>3</sub></b>	1.34	—	0.25	0.42
<b>BaHfSe<sub>3</sub></b>	1.57	—	0.26	0.49
<b>SrZrSe<sub>3</sub></b>	1.45	—	0.31	0.47
<b>SrHfSe<sub>3</sub></b>	1.72	—	0.47	0.51

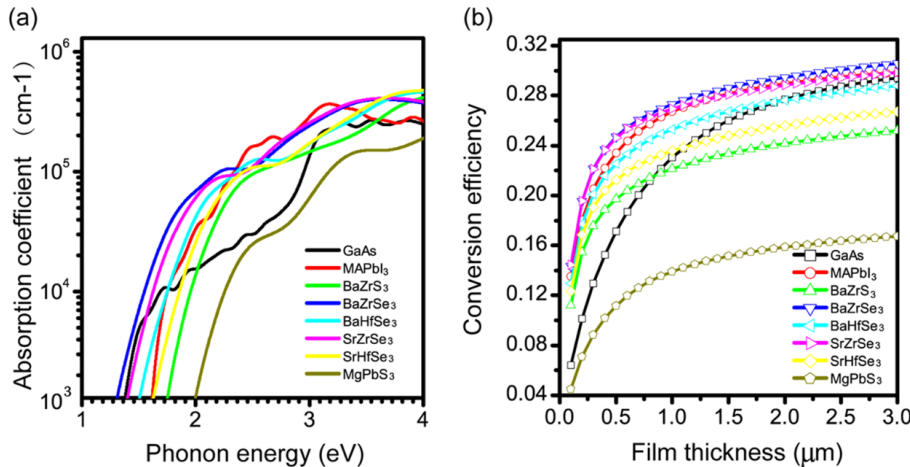


Figure 2.6: (a) Calculated optical absorption coefficients of six types of perovskites with MAPbI<sub>3</sub> and as a comparison GaAs. (b) Calculated conversion efficiency of six types of perovskites, MAPbI<sub>3</sub> and GaAs. Figure reproduced from Ref. 6.<sup>4</sup>

GaAs included as a comparison.<sup>6</sup> MgPbS<sub>3</sub> was then removed from the potential candidates due to its low absorption coefficient resulting in a poor PCE. This is due to the *s*-orbital transition in Pb<sup>4+</sup>, which is inferior to the *p-d* transitions seen in the other compounds. Dynamic stability was then carried out on the remaining materials, which all displayed stability at 300K. Overall, this paper serves as an excellent demonstration of workflow and uses a material screening funnel which can be implemented in this report to discover new hybrid chalcogenide perovskite solar absorbers.

In 2019, Park et al.<sup>210</sup> used machine learning (ML) algorithms and DFT to produce a systematic material screening analysis of inorganic and organic A-site cations on both  $\text{ABX}_3$  chalcogenide ( $\text{I-V-VI}_3$ ) and halide ( $\text{I-II-VII}_3$ ) perovskites.<sup>210</sup> They reported that for organic A-site cations, stability can be determined by the effective radius of polyatomic molecules and the number of lone pairs interacting with B-site atoms. 384  $\text{ABX}_3$  chalcogenide and halide perovskites which were charge neutral were chosen, where  $\text{B} = \text{V}^{5+}$ ,  $\text{Nb}^{5+}$ ,  $\text{Ta}^{5+}$ ,  $\text{Ge}^{2+}$ ,  $\text{Sn}^{2+}$  and  $\text{Pb}^{5+}$  and  $\text{X} = \text{O}^{2-}$ ,  $\text{S}^{2-}$ ,  $\text{Se}^{2-}$ ,  $\text{Te}^{2-}$ ,  $\text{F}^-$ ,  $\text{Cl}^-$ ,  $\text{Br}^-$  and  $\text{I}^-$ . The A-site metals chosen were  $\text{Li}^+$ ,  $\text{Na}^+$ ,  $\text{K}^+$ ,  $\text{Rb}^+$  and  $\text{Cs}^+$  and the molecular A-site cations included hydronium ( $\text{HY}^+$ ), ammonium ( $\text{AM}^+$ ), sulfonium ( $\text{SF}^+$ ), phosphonium ( $\text{PH}^+$ ), hydroxylammonium ( $\text{HA}^+$ ), methylammonium ( $\text{MA}^+$ ), hydrazinium ( $\text{HZ}^+$ ), formamidinium ( $\text{FA}^+$ ), formamide cation ( $\text{FO}^+$ ), ethylammonium ( $\text{EA}^+$ ), and guanidinium ( $\text{GA}^+$ ). As organic molecules are not spherical, it is difficult to predict how their orientation will interact with the surrounding octahedra. Therefore, randomly oriented molecules were used to avoid molecules becoming trapped in local minima configurations. The compounds then underwent a full structural relaxation and the phase stability was measured by  $\Delta H_c$ , which is the difference in energy between the cubic phase and relaxed phase calculated by DFT:

$$\Delta H_c = E_{\text{cubic}} - E_{\text{relax}} \quad (2.3)$$

The octahedral deformation was then measured by two parameters,  $\lambda$  and  $\sigma^2$  which denote the quadratic elongation and angle variance, respectively. A cubic structure has  $\lambda = 1$  and  $\sigma^2 = 0$ . Those compounds exhibiting edge or face sharing octahedra were then excluded as to not skew  $\lambda$  and  $\sigma^2$  values.<sup>7</sup> The comparison of 1704 perovskite structures was then completed using VASP calculations and by taking into account the different possible orientations of molecular cations. At high temperatures the organic cations can rotate freely and be modelled as spheres. At

lower temperatures the molecules could not be modelled as spherical. This results in a reduction in symmetry within the lattice and distort bonds. Therefore, the initial molecular orientation can result in different local energy mimimas.<sup>7</sup> To model the effective radii of these molecular cations the methods by Glazer<sup>197</sup> and Kieslich et al.<sup>196</sup> were used. Subsequently after relaxation, 1339 structures retained a perovskite structure. Figure 2.7 shows the angle variance ( $\sigma^2$ ) as a function of the quadratic elongation ( $\lambda$ ) where  $r_A$  is the radii of A-site cation and  $TF$  is the tolerance factor. Figure 2.7a is particularly relevant to this report as it shows that cations of smaller effective radii tend to remain closer to cubic structure. This differs greatly to halides (Figure 2.7b) which can tolerate a much larger A-site cation without major distortions. This implies that chalcogenide perovskites should be more stable when using smaller cations as a small increase in  $\angle X-B-X'$  will result in large distortions of the perovskite structure. Figure 2.7c shows a tolerance factor  $< 1$  can preserve a linear correlation between angle variance and parabolic elongation. In contrast, a tolerance factor  $\geq 1$  results in much greater elongation and deformation of the structure rather than distorting the  $\angle X-B-X'$  angle. It is desirable to minimise  $\lambda$ , as high values result in the loss of a perovskite structure, indicating severe structural phase instability. It can also be seen that halide structures are more concentrated around low values of  $\Delta H_c$  compared to chalcogenides, indicating the  $[BX_6]$  octahedra in chalcogenides are less rigid than halides, potentially indicating weaker bonds within B-X site interactions and making them less stable.<sup>7</sup>

This instability is further presented in Figure 2.8, where an increase in  $r_A$  results in a larger  $\Delta H_c$  in chalcogenides. Furthermore, chalcogenides were found to become highly unstable when  $\Delta H_c > 0.1$  eV/ion.<sup>7</sup> Halide perovskites, on the other hand are much more tolerable to variation in  $r_A$ . Using small cations will therefore be a priority in this report to minimise instability in potential candidate materials. While this report offers many insights into the properties of chalcogenide perovskites, it will be essential to adapt the methodologies to align with the objectives of this report.

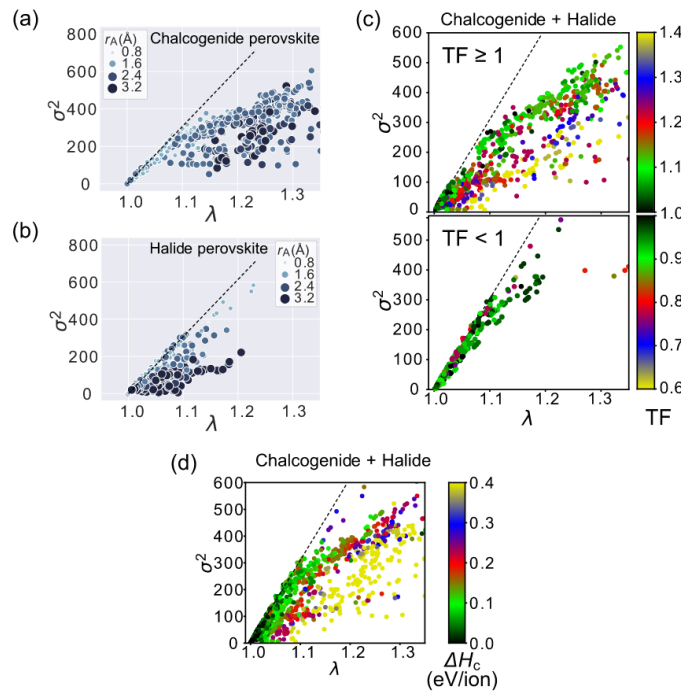


Figure 2.7: Angle variance,  $\sigma^2$ , as a function of the quadratic elongation,  $\lambda$ , in (a) chalcogenide compounds and (b) halide perovskites . (c) Colour map plot of chalcogenides and halides using Tolerance factor (TF); (d) colour map using  $\Delta H_c$  (in eV/ion). For an ideal cubic perovskite,  $\lambda=1$ ,  $\sigma^2=0$  and  $\Delta H_c= 0.0$  eV/ion. Figure reproduced from Ref. 7.

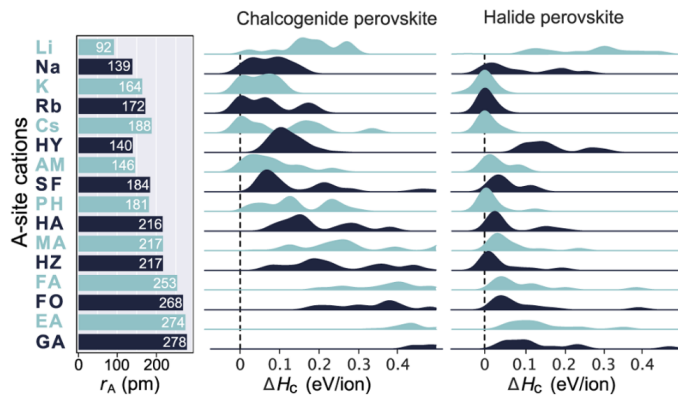


Figure 2.8: Gaussian kernel density estimates of  $\Delta H_c$  for each A-site cation. Figure reproduced from Ref. 7. Represents how the A-site cation radius,  $r_A$ , effects  $\Delta H_c$  in chalcogenide and halide perovskites.

Namely, in our report the use of Ta and Nb will be omitted and will be replaced with more Earth abundant materials such as Bi, Sb, Si, Ti, Ge and Sn. We will also only be considering S and Se based chalcogens for reasons aforementioned. Furthermore, the use of  $\Delta H_c$  can only be used as an indicator for stability and may not be an

accurate representation of a compounds true phase stability. Therefore, in this report will calculate the formation energy and energy above hull for each candidate material to achieve a more reliable characterisation of the thermodynamic stability.

## 2.4 Chalcogenide Perovskite Properties

### 2.4.1 Stability

To date, the most widely reported chalcogenide perovskite is BaZrS<sub>3</sub>. This is due to its thermodynamic stability but also its environmental stability. As seen, experimental verification has confirmed the promising properties of BaZrS<sub>3</sub> for photovoltaic devices. This is attributed to the formation of the pseudocubic GdFeO<sub>3</sub>-type distorted perovskite structure, resulting in a highly stable structure. Additionally, large band dispersions lead to low effective masses and therefore high charge carrier mobility.<sup>4</sup> Furthermore, BaZrS<sub>3</sub> has a very high absorption coefficient ( $> 10^5 \text{ cm}^{-1}$ ), close to the optimal absorption wavelength and has a direct bandgap of  $\approx 1.78 \text{ eV}$ .<sup>16</sup> BaZrS<sub>3</sub> is lead free and has several synthesise route while forming polycrystalline thin films.<sup>154,211</sup> There are also a number of other materials with appropriate bandgaps for solar application which have been reported by others, however this section will focus on the stability of BaZrS<sub>3</sub> as it is the most widely researched.<sup>4</sup> A report by Gupta et al.<sup>8</sup> explains the underlying mechanisms of BaZrS<sub>3</sub> high stability in comparison to MAPbI<sub>3</sub> by using characterisation techniques such as; photoluminescence (PL), x-ray diffraction (XRD), Raman spectroscopy and scanning electron microscopy (SEM).<sup>4</sup> Their results showed that BaZrS<sub>3</sub> stability was extended as a result of minimal ion migration and low numbers of interactions with moisture compared to MAPbI<sub>3</sub>. This allowed the chalcogenide samples to retain 60% of their photoresponse after four weeks, compared to MAPbI<sub>3</sub> which only retained 5% after four days under the same conditions.<sup>4</sup> The PL intensity graphs

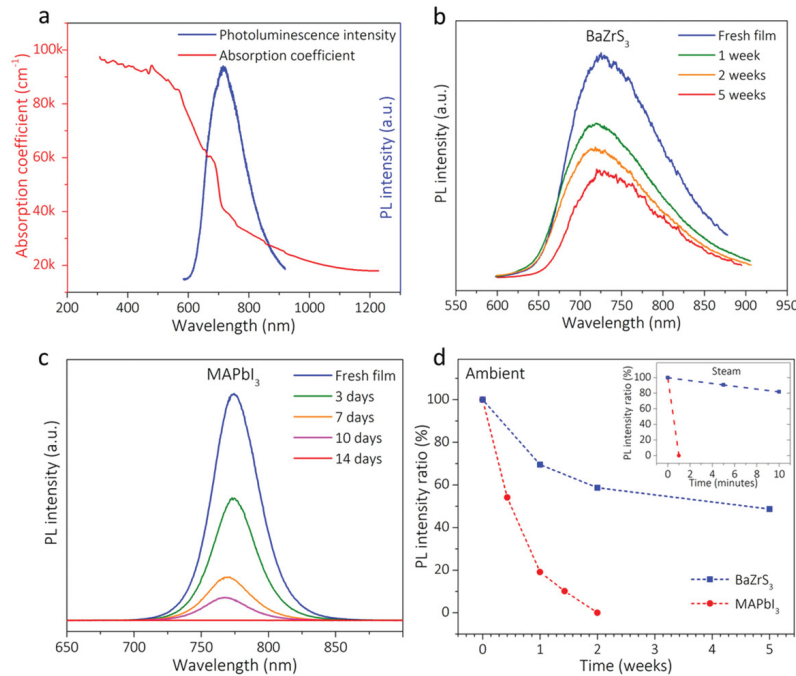


Figure 2.9: Photoluminescence characteristics of BaZrS<sub>3</sub> compared to MAPbI<sub>3</sub>. (a) Absorption coefficient and photoluminescence spectrum at room temperature. (b) BaZrS<sub>3</sub> photoluminescence intensity spectra over five weeks under ambient conditions. (c) MAPbI<sub>3</sub> photoluminescence intensity spectra over two weeks under ambient conditions. (d) Photoluminescence of BaZrS<sub>3</sub> and MAPbI<sub>3</sub> under ambient conditions.

Figure reproduced from Ref. 8.<sup>4</sup>

for these results can be seen in Figures 2.9a-d.

Further calculations were carried out using DFT in conjunction with data from Mosconi et al.<sup>212</sup> to simulate the effects of BaZrS<sub>3</sub> interactions with moisture. It was found after 10 ps that the change in distance between BaZrS<sub>3</sub> and H<sub>2</sub>O molecules was minimal, indicating that there is little interaction between moisture and BaZrS<sub>3</sub>.<sup>4</sup> MAPbI<sub>3</sub> showed a large reduction in interatomic distance due to its hydrophilic nature.<sup>4</sup> These results are visible in Figures 2.10a and 2.10b. Gupta et al.<sup>8</sup> also observed that photo-induced degradation was more prevalent in MAPbI<sub>3</sub> in comparison to BaZrS<sub>3</sub>. Chalcogenides vacancies showed to have higher activation energies compared to halide vacancies which resulting in the MAPbI<sub>3</sub> having a migration rate 10<sup>7</sup> times greater than that of BaZrS<sub>3</sub>.<sup>4,8</sup> The nearest neighbour sites can be seen in Figures 2.10c and the energy barriers for the such migration paths in Figure

2.10d.<sup>4</sup> This report demonstrates the exceptional photo and moisture stability of chalcogenide perovskites compared to halide perovskites.<sup>4</sup>

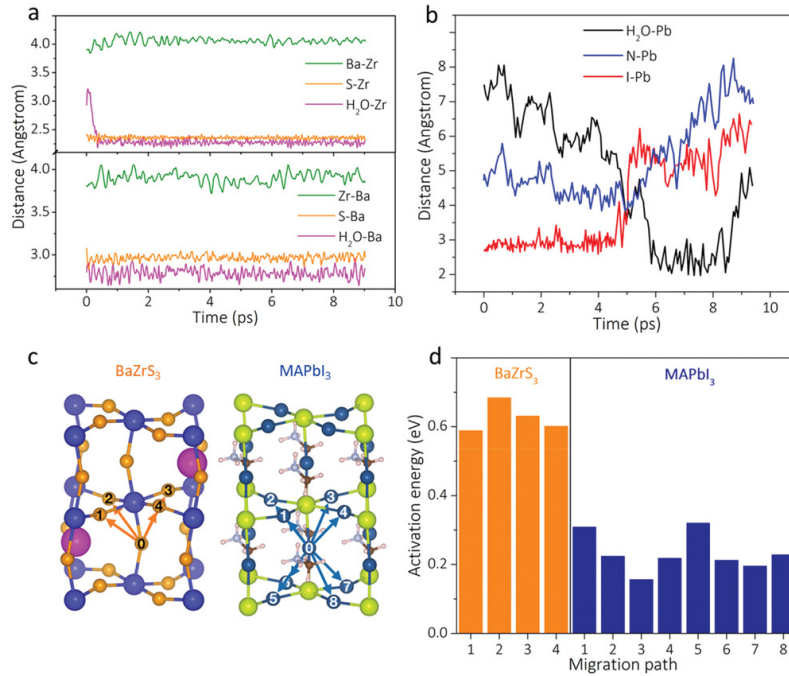


Figure 2.10: (a) Simulated interatomic distance of BaZrS<sub>3</sub> and H<sub>2</sub>O. (b) Simulated interatomic distance of MAPbI<sub>3</sub> and H<sub>2</sub>O. (c) Anion migration paths in BaZrS<sub>3</sub> and MAPbI<sub>3</sub>. (d) Energy barriers for sulphur vacancies and iodine vacancies. Figures reproduced from Ref. 8.<sup>4</sup>

Niu et al.<sup>9</sup> reported the thermal stability of five chalcogenide compounds ( $\alpha$ -SrZrS<sub>3</sub>,  $\beta$ -SrZrS<sub>3</sub>, BaZrS<sub>3</sub>, Ba<sub>2</sub>ZrS<sub>4</sub>, Ba<sub>3</sub>ZrS<sub>7</sub>) using thermogravimetric analysis up to 1200 °C in air. It was discovered that perovskite chalcogenides have a thermal stability greater than 600 °C and that the Ruddlesden-Popper phases have the highest thermal stability followed by  $\beta$ -SrZrS<sub>3</sub> and BaZrS<sub>3</sub> and finally the “needle-like”  $\alpha$ -SrZrS<sub>3</sub>. The thermogravimetric results can be seen in Figure 2.11. The increase in mass at approximately 600 °C indicates degradation of the sample by oxidation, confirmed by XRD. It was noted the reduction in mass initially seen in some samples was due to evaporation of excess iodine used as a catalyst in synthesis. Chalcogenides have exhibited superior stability properties in the presence of moisture, light and elevated temperature which are all weaknesses of their halide counterparts. Although, further research must be completed to observe the stability of chalcogenides in full

stack devices to understand the interfacial stability of chalcogenide perovskites.

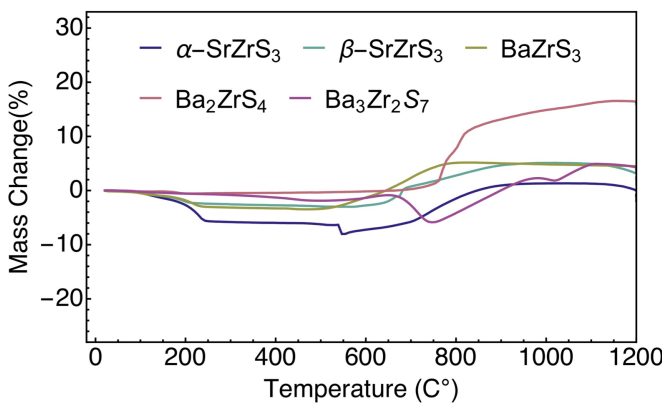


Figure 2.11: Thermogravimetric analysis mass change for various chalcogenide structures. Figure reproduced from Ref. 9.

## 2.4.2 Chemical Properties

### Toxicity and Abundance

Toxicity in photovoltaics has been an increasing concern as previously discussed with the use of Pb in halide perovskites and Cd in CdTe devices.  $\text{ABX}_3$  chalcogenide photovoltaics benefit as they do not contain toxic elements and can actually contain elements that are present in living organisms such as Sr.<sup>213</sup> and Zr.<sup>214</sup> Ba can be toxic when in a water soluble forms such as  $\text{BaCl}_2$ , however these cases are rare as most stable Ba compounds are water insoluble.<sup>215</sup> Sulphur is also non toxic apart from biologically active compounds like  $\text{H}_2\text{S}$ . Selenium is non-toxic in and is necessary for normal cellular function and only becomes toxic in very high doses.<sup>216</sup> The vast majority of elements used in chalcogenide perovskites are generally harmless, a major advantage to that of traditional photovoltaics and halide perovskites which use Pb. When it comes to the sustainability and scalability of photovoltaic technologies another important factor is the abundance of the constituent materials that will be used. The abundance of many common elements in photovoltaics can be seen in

Figure 2.12.

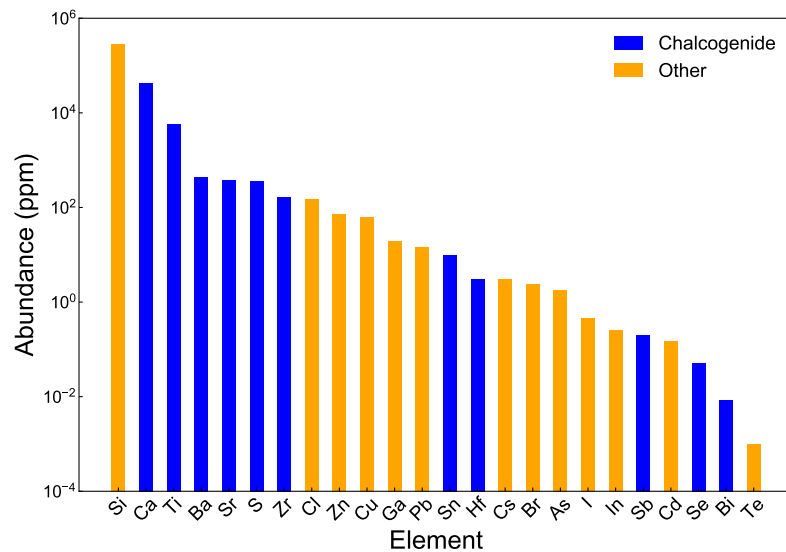


Figure 2.12: Bar chart representing the abundance of common elements used in solar cell. Those in blue are common to chalcogenide perovskites while orange indicates elements of other common photovoltaics. Data from Ref. 10.

Chalcogenide perovskites present a compelling case for scalability due to their elemental abundance. For instance, Ba has an abundance of 425 ppm and Sr (370 ppm), are significantly more plentiful than Pb (14 ppm), Cs (3 ppm) and I (0.45 ppm) which are crucial components of halide perovskites. Zr (165 ppm) and Ti (5,650 ppm) are also highly abundant and commonly used as elements within the B-site of chalcogenide perovskites or as alloying agents. By using abundant, non-toxic elements such as those in chalcogenide perovskites, minimal damage can be caused both to the environment and to human health. Additionally, the use of organic molecules can be introduced to limit the use of inorganic materials. This approach supports the scalability and economic feasibility of solar energy and also aligns better with global sustainability goals.

### 2.4.3 Optoelectronic Properties

#### Light Absorption

Chalcogenide perovskites exhibit impressive optoelectronic properties that have been calculated by first principles and verified through experimental reports.<sup>16</sup> Absorption is an important optical property of solar cells as it determines the minimum thickness of the absorber layer required.<sup>14</sup> Distorted chalcogenide perovskites including BaZrS<sub>3</sub>, SrZrS<sub>3</sub>, BaHfS<sub>3</sub> and SrHfS<sub>3</sub> have been shown to have an extraordinary absorption coefficients of  $\alpha > 10^5 \text{ cm}^{-1}$  near the  $E_g$ .<sup>16</sup> This value exceeds all existing solar cells absorption coefficients by an order of magnitude.<sup>16</sup> This high  $\alpha$  can be attributed to the profound  $p-d$  transitions, deriving from dense S 3p valence states and transition metal  $d$  states which have a very high joint density of states (JDOS).<sup>14,16</sup> This JDOS allows the absorption to rise to above  $10^5 \text{ cm}^{-1}$  within 0.3–0.5 eV above the absorption onset.<sup>3,16,149,161,217</sup> Due to this, a thickness of 500 nm was found to be suitable by Nishigaki et al.<sup>16</sup> for an absorption layer in chalcogenide perovskites. The optical bandgap of chalcogenide perovskites such as BaZrS<sub>3</sub> has been debated and ranges from 1.75–1.94 eV as seen in table 2.2. DFT has verified a direct bandgap however, the fundamental transitions have been debated. Hanzawa et al.<sup>156</sup> found the fundamental transition was allowed, whereas Peng et al.<sup>218</sup> concluded that the transition was forbidden due to band crossing. Nishigaki et al.<sup>16</sup> similarly found that the transition  $V_1 \rightarrow C_1$  is forbidden while  $V_2 \rightarrow C_1$  is the dominant absorption energy transition and occurs at 0.1 eV higher than the fundamental bandgap. These uncertainties may pertain to the ambiguities with the optical bandgap of BaZrS<sub>3</sub>. Photoluminescence peak positions are more consistent and have an average value of  $1.82 \pm 0.04 \text{ eV}$  across literature.<sup>14</sup>

## Charge Transport and Recombination

2

First principle calculations were carried out by Yuan et al.<sup>11</sup> to determine the carrier transport properties of BaZrS<sub>3</sub>. It was found that BaZrS<sub>3</sub> has a phonon-limited electron mobility of 37 cm<sup>2</sup>/Vs and a hole mobility of 11 cm<sup>2</sup>/Vs. Sulphur interstitials were found to be the largest contributor to nonradiative recombination and were found to limit carrier lifetime to 10 ns in sulphur rich conditions.<sup>11</sup> The high electron mobility of 37 cm<sup>2</sup>/Vs is comparable to MAPbI<sub>3</sub>, however the hole mobility is much lower (11 vs 47 cm<sup>2</sup>/Vs).<sup>219</sup> This contrast in electron and hole mobility in BaZrS<sub>3</sub> arises from the electronic band structure. BaZrS<sub>3</sub> exhibits a more dispersive CBM resulting in a lower electron effective mass of 0.3  $m_0$  while the hole effective mass was found to be much higher with a value of 0.9  $m_0$ . This is primarily due to the sulphides anionic behaviour in the valence band resulting in a more localised orbitals and a flatter band structure.<sup>11</sup>

### 2.4.4 Defect Chemistry and Doping

The most recent information regarding defect chemistry and doping in BaZrS<sub>3</sub> was completed by Yuan et al.<sup>11</sup> whom used the HSE06 hybrid functional to characterise a 3×3×2 supercell with charge correction and spin-polarisation included to calculate all the vacancies, interstitials and anti-site point defects in BaZrS<sub>3</sub> in both S-poor and S-rich conditions. The formation energies of these are seen in Figure 2.13.

It was found that in sulphur poor conditions the main defects were comprised of shallow donor defects near the CBM with sulphur vacancies ( $V_S$ ) being highly concentrated due to the low formation energy.<sup>11</sup> The  $V_S$  has two donor levels (+/0) and (2+/+), both of which being close to the conduction band. As the formation energies of defects near the VB is much higher than the CB, BaZrS<sub>3</sub> will be highly *n*-type doped by the  $V_S$  donors.<sup>11</sup> In sulphur-rich conditions, Yuan et al.<sup>11</sup> found that

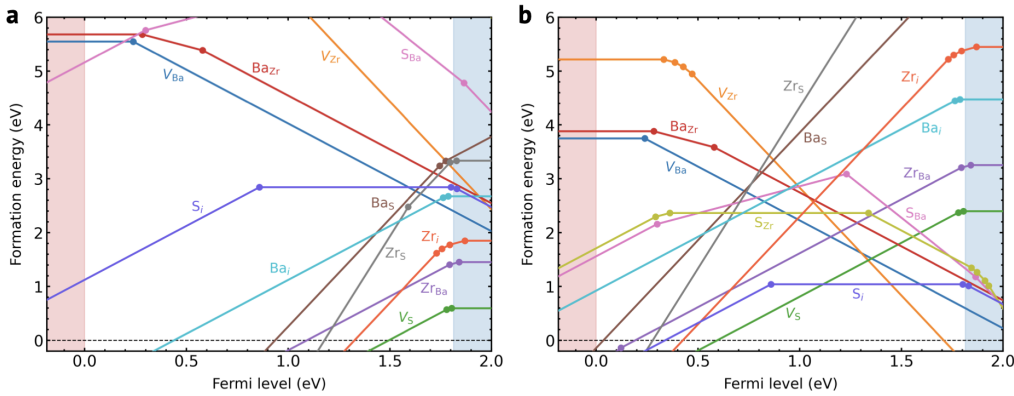


Figure 2.13: Formation energies of intrinsic point defects in  $\text{BaZrS}_3$  as a functional of Fermi level, under (a) S-poor and (b) S-rich conditions. The Fermi level is referenced to the (VBM) of  $\text{BaZrS}_3$ . The slopes of the formation-energy lines indicate defect charge states and the dots denote charge-state transition levels. Figure reproduced from Ref. 11.

the Fermi-level becomes pinned from the intersection of the  $V_S$  and  $V_{Zr}$ , causing the  $\text{BaZrS}_3$  to become primarily intrinsic with a slight *n*-type doping behaviour. Sulphur interstitial ( $S_i$ ) defects can also be seen to have a low formation energy, with charge state transitions of (2+/+) and (+/0) at 0.35 and 1.37 eV above the VBM, respectively. The (+/0) charge state transition has two non radiative capture processes:  $C_p^0$  for hole capture and  $C_n^+$  for the electron capture. The (2+/+) also has two capture processes:  $C_p^+$  and  $C_n^{2+}$ . The total capture coefficient  $C_{\text{tot}}$  is given by:

$$C_{\text{tot}} = \frac{C_n^+ + C_p^+}{1 + \frac{C_n^+}{C_p^0} + \frac{C_p^+}{C_n^{2+}}} \quad (2.4)$$

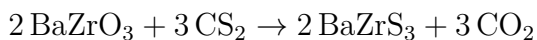
where  $C_{\text{tot}}$  refers to the rate at which charge carriers are trapped by defects and impurities in a material. At room temperature Yuan et al.<sup>11</sup> calculated  $C_{\text{tot}}$  to be  $1.25 \times 10^{-9} \text{ cm}^3/\text{s}$  which is slightly lower than that seen in the iodine interstitials in  $\text{MAPbI}_3$  ( $7 \times 10^{-9} \text{ cm}^3/\text{s}$ ).<sup>220</sup> This shows  $\text{BaZrS}_3$  is a defect-tolerant material with a low number of deep trap states to act as non-radiative recombination centres. Sulphur interstitial defects were found to be the limiting factor for the carrier lifetime which were calculated to be in the order of 10 ns.<sup>11</sup>

## 2.5 Synthesis Methods

2

Chalcogenides were first synthesised in 1857 by Hahn and Mutschke<sup>62</sup> who synthesised SrTiS<sub>3</sub>, BaTiS<sub>3</sub> and BaZrS<sub>3</sub>.<sup>4</sup> Since then, many novel synthesis techniques for chalcogenides have been recorded. Table 2.5 shows the wide variety of synthesis methods which is adapted from Buffiere et al.<sup>15</sup> and includes more recent synthesis methods for ABX<sub>3</sub> (X= S, Se) chalcogenide perovskite compounds.<sup>4</sup>

The most prominent approach for synthesis of chalcogenide perovskites has been through solid state reactions of powders, typically as oxides or sulphides.<sup>145</sup> The reactant materials are then sulphurised using CS<sub>2</sub> or H<sub>2</sub>S at high temperatures above 800 °C.



The high temperatures are required to prevent oxide phases forming and due to the endothermic nature of the reaction.<sup>142</sup> Additionally, these syntheses take extended periods of time to occur. A hypothesis for this extended reaction time by Hahn and Mutschke<sup>62</sup> states that in materials such as BaZrS<sub>3</sub> there is a large kinetic barrier at the surface of the constituent compounds (BaS and ZrS<sub>2</sub>) which limits diffusion resulting in a high energy input required to drive the reaction.<sup>4,14,62</sup> Wang et al.<sup>221</sup> discovered a method to synthesise BaZrS<sub>3</sub> at temperatures around 500 °C by using an excess of sulphur and through the addition of BaCl<sub>2</sub> during synthesis. However, the reduced synthesis temperatures resulted in BaZrS<sub>3</sub> not crystallising for at least 12 hours and took 168 hours to obtain a conversion rate of 77%.<sup>4,221</sup> More recently, Vincent et al.<sup>223</sup> developed a synthesis method which utilised a barium polysulfide liquid flux to overcome the diffusion limited growth regime and enhance the grain growth of BaZrS<sub>3</sub>. This method was successful at temperatures of 525 °C and only took 15 min to produce grains sizes in the order of hundreds of nanometers.<sup>223</sup> Prad-

Table 2.5: Synthesis methods for chalcogenide perovskites. Table reproduced from Ref. 15 with more recent synthesis methods added.

Compound	Synthesis Method	Structure	Ref.
BaTiS <sub>3</sub>	Sealed evacuated tubes (600–900 °C, BaS/TiS <sub>2</sub> mixture)	Hexagonal BaNiO <sub>3</sub>	62
	Ternary oxide under CS <sub>2</sub> flow (700–1000 °C)	-	152
	Sealed evacuated tubes (350–450 °C, BaS/BaCl <sub>2</sub> /TiS <sub>2</sub> /S mixture)	-	160
SrTiS <sub>3</sub>	Sealed evacuated tubes (600–900 °C, SrS/TiS <sub>2</sub> mixture)	Hexagonal BaNiO <sub>3</sub>	62
	Ternary oxide under CS <sub>2</sub> flow (800–1050 °C)	Needle-like phase	141
BaZrS <sub>3</sub>	Sealed evacuated tubes (800 °C, SrS/TiS <sub>2</sub> mixture)	Perovskite GdFeO <sub>3</sub>	62,141,152
	Binary oxide/carbonates under H <sub>2</sub> S flow (1100 °C)	-	154
	Sealed evacuated tubes (500–550 °C, BaS/BaCl <sub>2</sub> /ZrS <sub>2</sub> /S mixture)	-	221
	Ternary oxide (Ba–Zr–O) thin film sulfurised in an Ar + 5% H <sub>2</sub> S 700–1000 °C	Perovskite GdFeO <sub>3</sub>	222
	Liquid flux synthesis using barium thio-late and ZrH <sub>2</sub> at 500–600 °C	Perovskite GdFeO <sub>3</sub>	223
	Molecular precursor ink sulfurised at 575 °C	Perovskite GdFeO <sub>3</sub>	209
	Sputtered BaZr precursors capped by SnS are sulfurised at under 600 °C	Perovskite GdFeO <sub>3</sub>	224
	Crystallisation of pulsed laser deposited amorphous BaZrS <sub>x</sub> film at 500 °C	Perovskite GdFeO <sub>3</sub>	225
	Colloidal BaZrS <sub>3</sub> nanocrystals using a solid-state synthesis route	Perovskite GdFeO <sub>3</sub>	226
	sulfurisation procedure using CS <sub>2</sub> as the sulfur source at 1050 °C	Perovskite GdFeO <sub>3</sub>	151
CaZrS <sub>3</sub>	Solid-state synthesis to form colloidal nanocrystals	Perovskite GdFeO <sub>3</sub>	227
	Ternary oxide under CS <sub>2</sub> flow (1000–1200 °C)	Perovskite GdFeO <sub>3</sub> (highly distorted)	141,152
SrZrS <sub>3</sub>	Binary oxide/carbonates under H <sub>2</sub> S flow (1100 °C)	-	154
	Ternary oxide under CS <sub>2</sub> flow (1000–1200 °C)	Needle-like phase	141
	-	Perovskite GdFeO <sub>3</sub> (highly distorted)	152
BaSnS <sub>3</sub>	Binary oxide/carbonates under H <sub>2</sub> S flow (1100 °C)	-	154
	Piston cylinder, high-pressure apparatus (500–800 °C, 20 kbar, BaS/SnS <sub>2</sub> /S mixture)	Orthorhombic NH <sub>4</sub> CdCl <sub>3</sub>	171
SrSnS <sub>3</sub>	Piston cylinder, high-pressure apparatus (500–800 °C, 20 kbar, SrS/SnS <sub>2</sub> /S mixture)	Orthorhombic NH <sub>4</sub> CdCl <sub>3</sub>	171
CaHfS <sub>3</sub>	Binary oxide/carbonates under H <sub>2</sub> S flow (1100 °C)	Perovskite GdFeO <sub>3</sub>	154
BaHfS <sub>3</sub>	Binary oxide/carbonates under H <sub>2</sub> S flow (1100 °C)	Perovskite GdFeO <sub>3</sub>	154
SrZrSe <sub>3</sub>	Liquid flux synthesis using barium thio-late and HfH <sub>2</sub> at 500–600 °C	Perovskite GdFeO <sub>3</sub>	223
	Molecular precursor ink sulfurised at 575 °C	Perovskite GdFeO <sub>3</sub> (24.3%)/RP (75.7%)	209
	Sealed evacuated tubes (900–950 °C, SrSe/Zr/Se mixture)	Orthorhombic NH <sub>4</sub> CdCl <sub>3</sub>	168
SrHfSe <sub>3</sub>	Sealed evacuated tubes (800 °C, Sr/Hf/Se mixture)	Orthorhombic needle-like phase	169
CuTaS <sub>3</sub>	Grinding Ta <sub>2</sub> NiS <sub>3</sub> through brass sieve	Orthorhombic	228
	Sealed evacuated tubes (650–750 °C, Cu/Ta/S/I <sub>2</sub> mixture)	Honeycomb	229
LaYS <sub>3</sub>	Co-sputtered LaY precursor + sulfurisation (1000 °C)	CeTmS <sub>3</sub> type	230

han et al.<sup>209</sup> has also developed a synthesis method for BaZrS<sub>3</sub> and BaHfS<sub>3</sub> using a single phase, solution processed approach which has shown to form thin films at temperatures of 575 °C within 20 min.<sup>209</sup> Although synthesis temperatures and times are reducing, they are still very high in comparison to materials such as MAPbI<sub>3</sub> and further research must be completed to optimise synthesis processes.

### Chalcogenide Perovskite Devices

The first reported fabrication of a BaZrS<sub>3</sub> device was produced in 2024 by Dallas et al.<sup>227</sup> The solar cell had a unique architecture composed of a BaZrS<sub>3</sub>-filled TiO<sub>2</sub> electrode as the anode, an electrolyte solution of I<sub>3</sub><sup>-</sup> / I<sup>-</sup> and a Pt-coated FTO glass as the cathode. This design reached a PCE of 0.11% and FF of 61%. The report builds upon a synthesis method by Ravi et al.<sup>226</sup> based on solid state synthesis to form a colloidal nanocrystal ink using a N-Methyl-2-pyrrolidone (NMP)-oleylamine (OA) mixture which was then permeated into the mesoporous TiO<sub>2</sub> electrodes. This colloidal ink was discovered to be stable for months in humid air conditions demonstrating chalcogenide perovskites remarkable stability. The synthesis of BaZrS<sub>3</sub> was based on the solid state reaction of BaS and elemental Zr with iodine as the catalyst as reported by Niu et al.<sup>147</sup> and Ravi et al.<sup>226</sup> To then form BaZrS<sub>3</sub> particles, a solid state synthesis reaction was completed to produce the GdFeO<sub>3</sub>-type ternary perovskite phase. It was noted that a small amount of unwanted phases were also present namely, Ba<sub>3</sub>ZrS<sub>7</sub> and ZrS<sub>2</sub>. Characterisations were then completed to obtain an optical bandgap of 1.77 eV and strong absorption energies at less than 3.4 eV making this device highly suitable for Si-perovskite tandem cells. Using ultraviolet phototransistor spectroscopy (UPS), the workfunction was estimated at 3.2 eV and the VBM at 1.51 eV. BaZrS<sub>3</sub> displayed an *n*-type doping presumably due to sulphur vacancies within the lattice.<sup>231</sup> These sulphur vacancies were confirmed using x-ray fluorescence (XRF) which presented a stoichiometry of Ba<sub>0.99</sub>Zr<sub>0.9</sub>S<sub>2.52</sub>. The

final form of the device displayed an appealing bandgap for tandem photovoltaics, photoluminescence at the band-edge and acceptable polycrystalline grain formation deposited on the substrate. The main drawback from this technique is the large number of sulphur vacancies, resulting in an increase in trapped states and non-radiative recombination causing a reduction in free charge carriers and significant losses in PCE. The stability of the device after eight days showed a slight increase in  $J_{sc}$ , a small decrease in FF and a constant  $V_{oc}$  further reinforcing the high stability's of these chalcogenide perovskites.<sup>227</sup>

## 2.6 Hybrid Chalcogenide Perovskites

This report aims to advance our understanding of chalcogenide perovskites through the exploration of hybrid organic-inorganic chalcogenide perovskites. By combining organic molecules with various Earth-abundant materials, we aim to identify promising candidates for solar cells. Currently all experimental reports to date have been on fully inorganic compounds. However, similar to Pb halide perovskites, there is scope to replace the A-site with an organic molecule. To date, there has only been two reports which mention the use of hybrid chalcogenide perovskite - the first being the report by Park et al.<sup>7</sup> which used monovalent cations which would in turn result in pentavalent B-site cations to be used. The second being the report by Sun et al.<sup>3</sup> who mentions the substitution of the inorganic A-site cation with the organic  $\text{NH}_3\text{NH}_3^{2+}$  HZ ion to form  $\text{HZZrS}_3$ . This is the only paper to exclusively mention a divalent organic molecule being used in a chalcogenide perovskite to our knowledge. They predicted  $\text{HZZrS}_3$  was to have a direct bandgap of 1.68 eV at the  $\Gamma$ -point, equating to a theoretical efficiency of 29%, using the HSE06 functional. Molecular dynamics was also conducted at 423 K for 20 ps and showed no signs of instability, which is highly encouraging for this report. It was also recommended that other organic molecules such as  $\text{NH}_3-\text{CH}_2-\text{NH}_3^{2+}$  could be potential candidates. This

report stands as a good foundation to work from, in particular continuing on the work of HZZrS<sub>3</sub> and similar compounds.



# 3

## Research Outline

In this report, we show the computational discovery of novel organic molecules for integration into hybrid chalcogenide perovskites for application in photovoltaic devices. Using the VASP, this study aims to screen these organic molecules for charge neutrality and perform electronic and geometrical relaxations to ensure structural stability. By employing AIMD simulations with machine-learned force fields, we will assess the stability of selected hybrid chalcogenide candidates. Additionally, we will determine the thermodynamic stability of these molecules by calculating the energy above hull. Suitable materials will then have their electronic and optical properties evaluated, providing insights into their suitability for photovoltaic applications. Through this computational approach, we aim to identify potential organic molecules that can be implemented into a perovskite structure to be synthesised for use in photovoltaic solar cells.



# 4

## Computational Theory

### Contents

---

4.1	Quantum Mechanical Approaches	61
4.2	Hartree-Fock Method	63
4.3	Density Functional Theory	65
4.4	Exchange-Correlation Functional	66
4.4.1	LDA and GGA	67
4.4.2	Hybrid Density Functional Theory	69
4.5	Quantum Mechanics in Solid State	70
4.5.1	Periodic Boundaries and The Unit Cell	70
4.5.2	The Brillouin Zone and The Reciprocal Lattice	71
4.5.3	Basis Sets and Pseudopotentials	73

---

### 4.1 Quantum Mechanical Approaches

Computational quantum chemistry is a branch of chemistry which employs quantum mechanical approaches to calculate a variety of material properties. This report uses *Ab initio* calculations to assess the optoelectronic properties of solid state materials using the theory of quantum mechanics, differing from classical and empirical

methods which depend on predefined parameters. *Ab initio* calculations attempt to approximate the time independent Schrödinger equation (TISE) from first principles:

## 4

$$\hat{H}\Psi = E\Psi \quad (4.1)$$

where  $\Psi$  is the wavefunction,  $E$  is the energy eigenvalue and  $\hat{H}$  is the Hamiltonian operator, which can be decomposed into a kinetic contribution ( $\hat{T}$ ) and a potential energy contribution ( $\hat{V}$ ) within an electronic system provided by nuclear-nuclear, nuclear-electron and electron-electron interactions as:

$$\hat{H} = \hat{T}_{\text{elec}} + \hat{V}_{\text{elec-elec}} + \hat{T}_{\text{nuc}} + \hat{V}_{\text{nuc-nuc}} + \hat{V}_{\text{nuc-elec}} \quad (4.2)$$

which can be further decomposed to:

$$\hat{H} = \underbrace{\sum_i \frac{p_i^2}{2m_i} + \frac{1}{2} \sum_{i \neq j} \frac{e^2}{|r_i - r_j|}}_{\text{elec}} + \underbrace{\sum_A \frac{P_A^2}{2m_A} + \sum_{A \neq B} \frac{Z_A Z_B e^2}{|R_A - R_B|}}_{\text{nuc}} - \underbrace{\frac{1}{2} \sum_{A,i} \frac{Z_A e^2}{|R_A - r_i|}}_{\text{elec-nuc}} \quad (4.3)$$

where  $i, j$  are distinct electrons,  $p$  is the electron momentum,  $m$  is the mass,  $e$  is the elementary charge,  $r$  is the electronic coordinate,  $P$  is the nuclei momentum,  $Z$  is the atomic number,  $A$  and  $B$  are distinct nuclei and  $R$  is the nuclear coordinate. By obtaining the energy eigenvalue for the ground state and thus the wavefunction of the system, various properties can be determined through the use of additional operators. However, when there is more than one electron in the system

(i.e multi-electron) the electron-electron and nuclear-electron interactions become impossible to solve analytically and therefore approximations must be made to simplify the Hamiltonian operator to achieve a solution.<sup>232</sup> One simplification is the Born-Oppenheimer (B-O) approximation which allows for decoupling of the electronic and nuclear parts of the wavefunction by considering the nuclei stationary relative to electrons resulting in their kinetic energy,  $\hat{T}_{\text{nuc}}$ , being disregarded.<sup>233,234</sup> Additionally, nuclear-nuclear potential energies can be considered constant for a determined set of nuclear coordinates. This allows the nuclear and electronic wavefunctions to be solved separately to find the total wavefunction, seen as:<sup>235,236</sup>

$$\Psi_{\text{total}} = \psi_{\text{elec}} \times \psi_{\text{nuc}} \quad (4.4)$$

This allows the electron-nuclear interaction to become a mean field approximation which simplifies the interactions of each individual particle to a “mean” interaction across the system,<sup>237</sup> providing an initial solution to the Schrödinger equation, which can then be further refined by using self-consistent field (SCF) methods such as Hartree-Fock (HF) and DFT to iteratively generate wavefunctions of lower energy until convergence toward the ground state energy.

## 4.2 Hartree-Fock Method

In the late 1920’s, the HF method was proposed, with the idea of simplifying the TISE into a single electron Hamiltonian by treating electrons as non-interacting.<sup>238</sup> Within this approach the many electron wavefunction can essentially be determined by calculating the product of multiple single electron wavefunctions,  $\hat{h}_i$ , to satisfy the eigen equation:<sup>239</sup>

$$\hat{h}_i \chi_i(x_i) = \epsilon_i \chi_i(x_i) \quad (4.5)$$

where the single electron energy,  $\epsilon_i$ , occupies the spin orbital,  $\chi_i(x_i)$  with  $x_i$  being the generalised coordinate along each Cartesian direction. The total energy of this non-interacting electron system is therefore given by the summation of single electron energies, while the total electronic wavefunction is given by the Hartree Product for individual electrons  $1, 2, \dots, n$  for states  $\alpha, \beta, \gamma, \dots, \pi$ :<sup>240</sup>

## 4

$$\Psi(x_1, x_2, x_3, \dots, x_n) = \chi_\alpha(x_1), \chi_\beta(x_2), \chi_\gamma(x_3) \dots \chi_\pi(x_n) \quad (4.6)$$

The Hartree Product results in a symmetric wavefunction, rendering it unsuitable for electrons, as Fermions must obey the Pauli exclusion principle, meaning the wavefunction must be antisymmetric. To overcome this disparity, Fock<sup>233</sup> and Slater<sup>241</sup> showed that an antisymmetric wavefunction could be formulated through the use of the Slater determinant which ensures a symmetry exchange. This is viable as exchange integrals are formed when the determinant is applied and consequently results in electrons with the same spin orbital to have a wavefunction value of zero, making it impossible for symmetrical spin electrons to exist in the same space.<sup>242</sup> The non-zero wavefunctions can then be iterated, minimising energy at each step until the solution converges. Although the HF method is still used within quantum chemistry, it is generally used in conjunction with other quantum mechanical methods as will be discussed. The HF method is limited by the fact it does not account for electron correlation beyond the mean field approximation resulting in electron-electron interactions being neglected.<sup>243</sup> This can result in large errors when systems which rely heavily on electron correlation are examined as they do not account for van der Waals interactions, bond energies and reaction energies.<sup>244</sup>

## 4.3 Density Functional Theory

Density Functional Theory is a quantum method designed to simplify electron-electron interactions through approximations of the electron density, allowing other properties to be obtained.<sup>245,246</sup> The first model that explored using the electron density,  $\rho(\mathbf{r})$ , over the wavefunction was proposed in the 1920's by Thomas and Fermi<sup>247</sup> whom attempted to describe an electronic system by the electron density to develop ideas such as the homogeneous electron gas model.<sup>247</sup> The Thomas Fermi approach is a semi-classical method that describes the total energy of a system ( $E_{TF}$ ) based on a kinetic energy ( $T_{TF}$ ) functional and the distribution of electrons under the influence of the nuclear potential ( $V_{\text{nuc-elec}}$ ) and the electron-electron repulsion ( $E_{\text{elec-elec}}$ ) represented as:

$$E_{TF}[\rho(\mathbf{r})] = \underbrace{C_K \int [\rho(\mathbf{r})]^{\frac{5}{3}} d\mathbf{r}}_{T_{TF}} + \underbrace{e \int \rho(\mathbf{r}) V_{\text{ext}} \mathbf{r} d\mathbf{r}}_{V_{\text{nuc-elec}}} + \underbrace{\frac{e^2}{2} \iint \frac{\rho(\mathbf{r}\rho\mathbf{r}')}{|\mathbf{r} - \mathbf{r}'|} d\mathbf{r} d\mathbf{r}'}_{E_{\text{elec-elec}}} \quad (4.7)$$

where  $C_K$  is a kinetic constant equal to  $\frac{3h^2}{10m} \left(\frac{3}{8\pi}\right)^{\frac{2}{3}}$  and  $V_{\text{ext}}$  is the external potential. The physical meaning of the third term ( $E_{\text{elec-elec}}$ ) is that the electronic properties are determined by functionals of the electronic density by applying a local approximation which is the basis of the LDA. However, the inclusion of classical terms and the use of a mean field approximation results in poor predictions of real electronic systems. Major strides in DFT were developed by Hohenberg and Kohn in the 1960's to develop the framework of DFT that is used today.<sup>248</sup> It was found that the variational principle (i.e  $E_0 \leq \langle \psi_{\text{trial}} | \hat{H} | \psi_{\text{trial}} \rangle$ ) exist for the energy functional  $E[\rho(\mathbf{r})]$ , meaning the ground state energy,  $E_0$ , is always less than or equal to the total energy predicted by the electron density.<sup>245</sup> This energy functional can then be written as the sum of  $V_{\text{ext}}$  and the Hohenberg-Kohn universal functional,  $F[\rho(\mathbf{r})]$ , as:<sup>248</sup>

The Hohenberg-Kohn universal functional contains all the information required to obtain the ground state energy value, however the form of this functional was not identified by Hohenberg and Kohn in the 1964 paper.<sup>248</sup> It was not until the following year until Kohn and Sham<sup>249</sup> suggested a method to compute an approximation of  $F[\rho(\mathbf{r})]$ . This was done by calculating the sum of the Hartree energy,  $E_{\text{elec-elec}}$ , the kinetic energy,  $T_S[\rho(\mathbf{r})]$ , and the approximate energy correction in the form of the exchange-correlation energy,  $E_{xc}[\rho(\mathbf{r})]$ .<sup>1</sup>

$$F[\rho(\mathbf{r})] \equiv E_{\text{elec-elec}}[\rho(\mathbf{r})] + T_S[\rho(\mathbf{r})] + E_{xc}[\rho(\mathbf{r})] \quad (4.9)$$

The inclusion of fictitious non-interacting electrons with identical densities allows the kinetic energy term to be calculated through use of the Slater determinant in a single set of electron molecular orbitals, analogous to the Hartree-Fock method. Unfortunately, the exchange-correlation functional is not known and must be approximated in DFT calculations. Many functionals have been developed, each with their own associated complexities and computational costs.

## 4.4 Exchange-Correlation Functional

In DFT, the exchange correlation energy,  $E_{xc}$ , is a fundamental component that captures the many-body interactions electrons encounter which are not accounted for in the simpler terms of the total energy functional. The exchange correlation energy is the combination of the exchange energy,  $E_x$ , and the correlation energy,

$E_c$ .<sup>250</sup>

$$E_{xc} = E_x + E_c \quad (4.10)$$

The addition of the Exchange-correlation functional has been fundamental to the success of DFT and has enabled a wide range of systems to be described with good accuracy and relatively low computational cost compared to wavefunction based methods.

4

#### 4.4.1 LDA and GGA

Many exchange-correlation functionals are derived from the uniform electron gas model where the exchange correlation functional is given by the inner product of the local electron density and exchange-correlation energy per electron,  $\epsilon_{xc}[\rho(\mathbf{r})]$ , as:

$$E_{xc}[\rho(\mathbf{r})] = \int \rho(\mathbf{r}) \epsilon_{xc}(\rho(\mathbf{r})) d(\mathbf{r}) \quad (4.11)$$

It is seen that the exchange-correlation energy is dependent on the value of the electron density at each point in space and thus is suitably named the Local Density Approximation. This method is the most basic functional and can be computed by quantum Monte Carlo simulations.<sup>251</sup> The LDA assumes density is varying slowly within an inhomogeneous solid and can be calculated using the homogeneous electron gas functional. This is a viable approach to predict many semiconductor properties to a reasonable accuracy, however in systems with high electron densities or systems with a high degree of correlation, LDA begins to break down and produces inaccurate results. DFT is known to underestimate bandgaps of semiconductors however this is especially prominent in LDA, with bandgap underestimations of up to 40%.<sup>252</sup> This arises for two reasons, firstly the exchange-correlation functional,  $E_{xc}[\rho(\mathbf{r})]$ , is independent of energy in the Kohn-Sham equations resulting in DFT

not accounting for discontinuities in the exchange-correlation potential,  $V_{xc}[\rho(\mathbf{r})]$  when the number of electrons  $N$  changes by an integer value.

$$V_{xc}[\rho(\mathbf{r})] = \frac{dE_{xc}[\rho]}{d\rho(\mathbf{r})} \quad (4.12)$$

This derivative discontinuity,  $\Delta_{xc}$ , can be represented by the difference between the true Kohn-Sham potential gap and predicted bandgap not considering the discontinuity and require a correction which is not accounted for in LDA or Generalised Gradient Approximation (GGA) and thus result in lower bandgap prediction.<sup>253</sup> The GGA was first realised in 1986 by Perdew and Yue<sup>254</sup> as a refinement of LDA by including an expansion of higher-order gradients of the electron density in the space surrounding the point  $\mathbf{r}$  rather than solely at point  $\mathbf{r}$  as seen in LDA. The most popular GGA exchange-correlation is the PBE.<sup>255</sup> The widespread popularity of PBE is due to the simplicity of the functional compared to more complex alternatives, while maintaining a similar accuracy. However, the PBE functional can cause an underbinding in the gradient expansion, resulting in overestimates in lattice parameters.<sup>256</sup> To improve the accuracy in solids, PBEsol<sup>257</sup> was developed to better predict energies and lattice parameters in solids. Even after improving properties, GGAs, still suffer from intrinsic problems. Both LDA and GGA functionals suffer from the self-interaction error where an electron incorrectly interacts with itself. This can be understood by examining the  $E_{\text{elec-elec}}$  term in Equation 4.7 as it includes a self-interaction where there is an integral of the electron density with itself. Normally this self interaction would cancel out due to the basis of the Slater determinant in the exchange integral, however, as the exchange-correlation is an approximation there is always a remaining value associated with the self interaction. This residual value causes overestimates of Coulombic repulsion and delocalisation of electron densities.<sup>258</sup> This is particularly severe in highly localised orbitals such

as some transition metals and oxides.<sup>259</sup> Approaches such as DFT+U aim to correct delocalisation issues with PBE, however other methods must be used to improve electronic structure calculations.

#### 4.4.2 Hybrid Density Functional Theory

4

Hybrid Density Functional Theory (HDFT) is a more recent functional which aims to reduce the self-interaction problem by combining the exact HF exchange with the exchange-correlation functional in DFT in the general form of:

$$E_{xc}^{HDFT} = \alpha E_x^{HF} + (1 - \alpha) E_{xc}^{DFT} \quad (4.13)$$

where  $\alpha$  is the amount of HF exchange included. An  $\alpha$  value of 0.25 has been derived from perturbation theory and is suitable for most molecules and works particular well within the PBE0 functional to give accurate bond lengths and energies and takes the form of:<sup>260,261</sup>

$$E_{xc}^{PBE0} = \frac{1}{4} E_{xc}^{HF} + \frac{3}{4} E_x^{PBE} + E_c^{PBE} \quad (4.14)$$

Further developments were made by Heyd, Scuseria and Ernzerhof whom developed the HSE06, by splitting the terms from Equation. 4.14 into their short-range (SR) and long-range (LR) Coulombic interactions and thus the following equation can be derived:<sup>262</sup>

$$E_{xc}^{HSE}(\alpha, \omega) = \alpha E_x^{HF,SR}(\omega) + (1 - \alpha) E_x^{PBE,SR}(\omega) + E_x^{PBE,LR}(\omega) + E_c^{PBE} \quad (4.15)$$

where  $\alpha$  is a parameter governing the proportion of exchange and  $\omega$  is an adjustable parameter that dictates the extent of short-range interactions. The HSE06 functional is the equivalent of PBE0 when  $\omega = 0$  and tends towards PBE as  $\omega \rightarrow \infty$ .

The HSE06 functional uses  $\alpha = \frac{1}{4}$  and a  $\omega = 0.11 \text{ bohr}^{-1}$ .<sup>263</sup> HSE06 and PBE work well in solid and molecular systems and do not suffer from self interaction errors as much due to the exact exchange from HF.

## 4

## 4.5 Quantum Mechanics in Solid State

### 4.5.1 Periodic Boundaries and The Unit Cell

Crystalline solids are characterised by their periodic arrangement of atoms, which can be described using a primitive unit cell which is the smallest repeating unit that captures the structural and chemical features of the solid. The unit cell is defined by its lattice parameters ( $a$ ,  $b$ , and  $c$ ) and angles ( $\alpha$ ,  $\beta$ , and  $\gamma$ ), which reflect the periodicity and symmetry of the crystal lattice. A  $3 \times 3 \times 1$  unit cell can be seen in Figure 4.1.

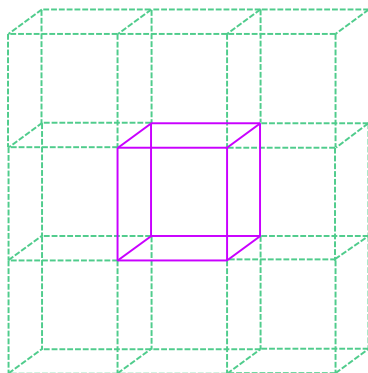


Figure 4.1: A  $1 \times 1 \times 1$  conventional unit cell (purple) surrounded by unit cells (dashed green) to represent periodicity to form a  $3 \times 3 \times 1$  expanded unit cell. Image reproduced from Ref. 12

This periodicity can be taken advantage of by instead of treating each atom in the solid individually, the periodicity of the lattice allows for the calculation of the wavefunction for a single unit cell under periodic boundary conditions. The resulting wavefunction can then be replicated for each cell to generate the wavefunction for

the entire solid structure. This approach, known as periodic density functional theory (PDFT) makes the computational treatment of solids tractable by significantly reducing the number of particles considered in the calculation. To further reduce the computational cost, the space group symmetry of the crystal can be exploited. By using the smallest possible unit cell, that being the primitive cell, the number of particles in the calculation can be reduced to efficiently solve the Schrödinger equation for the solid material. It must be noted that this approach is only applicable to crystalline solids that have a long-range periodicity and is not suitable for amorphous materials.

### 4.5.2 The Brillouin Zone and The Reciprocal Lattice

To describe our solid state systems we again take advantage of periodicity by describing the wavefunction as a combination of plane waves in the reciprocal lattice. This reciprocal lattice space can be understood by the periodicity of the real space lattice, described by the primitive lattice vectors  $\mathbf{a}_1$ ,  $\mathbf{a}_2$  and  $\mathbf{a}_3$  where the atomic structure is invariant under translation for any vector which is the sum of integer multiples of these vectors such that:

$$\mathbf{R} = n_1\mathbf{a}_1 + n_2\mathbf{a}_2 + n_3\mathbf{a}_3 \quad (4.16)$$

where  $n_i \in \mathbb{Z}$ . Alternatively, the real space lattice can be represented in terms of a reciprocal lattice with vectors  $\mathbf{b}_1$ ,  $\mathbf{b}_2$  and  $\mathbf{b}_3$  with the relationship  $\mathbf{a}_i \cdot \mathbf{b}_i = 2\pi$ , derived from the Fourier transformation of a distinct lattice. Therefore, the reciprocal lattice can be expressed as:

$$\mathbf{b}_i = \frac{2\pi}{\mathbf{a}_i} \quad (4.17)$$

For this reciprocal lattice translation the wavevector,  $k$ , which is akin to  $\mathbf{R}$  can then be used to describe the reciprocal lattice vectors as:

$$k = n_1 \mathbf{b}_1 + n_2 \mathbf{b}_2 + n_3 \mathbf{b}_3 \quad (4.18)$$

## 4

In the late 1920's Bloch derived a theorem, showing that the wavefunction of an electron moving through a periodic potential can be modelled as:<sup>264</sup>

$$\Psi(\mathbf{r}) = e^{ik\mathbf{r}} u(\mathbf{r}) \quad (4.19)$$

where  $u(\mathbf{r})$  is a periodic function at position  $\mathbf{r}$  within the unit cell. The wavevector,  $k$ , describes the phase relationship between adjacent cells such that each unit cell can be described as a discrete point with a range of values in the reciprocal lattice equating to:

$$-\frac{\pi}{a} < k \leq \frac{\pi}{a} \quad (4.20)$$

where  $a$  is the lattice spacing. The  $\Gamma$ -point is the region within the Brillouin Zone where  $k = 0$  and is often where the electronic bands maxima and minima are based, making the  $\Gamma$ -point essential for electronic structure calculations. To obtain the wavefunction, only the  $k$ -points within the first Brillouin zone are required, due to the aforementioned periodicity. As there are an infinite number of  $k$ -points, to make computational sense, an approximation is made through  $k$ -point sampling, where an integral of the Brillouin zone is calculated by the sum of equally spaced  $k$ -points. The number of  $k$ -points must converge to ensure accuracy while limiting computational costs. Fortunately, semiconductor PV materials do not require dense  $k$ -point meshes, unlike those seen in metallic systems.

### 4.5.3 Basis Sets and Pseudopotentials

The choice of basis functions used to represent the wavefunction can impact the computational cost and accuracy. Common basis functions include atom-centred basis sets composed of atomic orbitals, yielding the linear combination of atomic orbitals (LCAO) method.<sup>265</sup> In periodic materials, the plane wave basis set is most suitable due to its ability to translate into a periodic formalism through a fast Fourier series transformation. However, plane waves contain multiple nodes close to the nucleus, making it computationally expensive and difficult to calculate the wavefunction for these core states. This is overcome by replacing the nodes at the core section of the wavefunction with a smooth and nodeless pseudopotential curve.<sup>266</sup> Pseudopotentials effectively reduce the number of terms required to express the wavefunction and can drastically improve performance in computational calculations. A schematic of a pseudopotential can be seen in Figure 4.2. The curve exists from  $0 - r_c$ , where  $r_c$  is the plane wave cutoff value that is required to reduce the basis set to a finite size. This simple convergence parameter makes plane wave basis sets favourable over localised atomic basis sets.

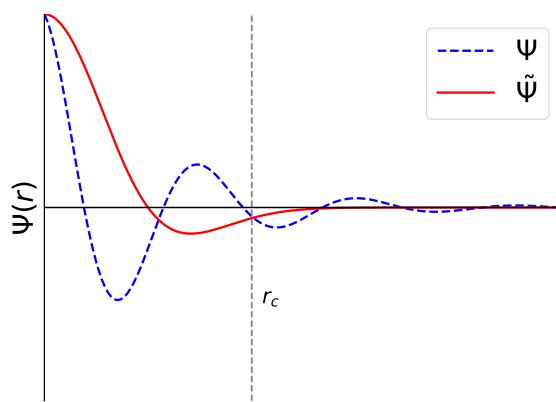


Figure 4.2: Illustration of a pseudopotential describing the wavefunction within the cutoff region,  $r_c$ .  $\Psi$  (blue dashed line) represents the true all electron wavefunction while  $\tilde{\Psi}$  (red line) represents the pseudopotential wavefunction.

VASP employs a combination of the pseudopotential method and plane wave

approach through the use of the projector augmented wave (PAW) method.<sup>267,268</sup> The PAW method can be used to simplify the all-electron wavefunction by applying a linear transformation operator,  $\hat{\mathcal{T}}$ , to transform rapidly oscillating wavefunctions with sharp features near the ion cores into smooth wavefunctions:

$$|\Psi\rangle = \hat{\mathcal{T}} |\tilde{\Psi}\rangle \quad (4.21)$$

where  $|\Psi\rangle$  is the all-electron wavefunction and  $|\tilde{\Psi}\rangle$  is the pseudo wavefunction. This transformation is applied to the Kohn-Sham (KS) equation to be solved. The transformation operator is defined such that by solving the KS equation the wavefunction becomes smooth. As it is already smooth at a particular point from the core,  $\hat{\mathcal{T}}$  needs to correct the wavefunction near the nuclei:<sup>269</sup>

$$\hat{\mathcal{T}} = 1 + \sum_a \hat{\mathcal{T}}^a \quad (4.22)$$

where  $a$  is an atom index and  $\hat{\mathcal{T}}^a$  is the atom centred transformation within an augmentation region around  $a$ . The augmentation region is defined as  $|\mathbf{r} - \mathbf{R}^a| < r_c^a$ , where  $\mathbf{R}^a$  is the position vector of the atomic site  $a$  and  $r_c^a$  is the cutoff radii of  $a$ . The all-electron KS wavefunction can then be obtained by applying  $\hat{\mathcal{T}}$  to the pseudo wavefunction in the form:<sup>269</sup>

$$\Psi(\mathbf{r}) = \tilde{\Psi}(\mathbf{r}) + \sum_a \sum_i (\phi_i^a(\mathbf{r}) - \tilde{\phi}_i^a(\mathbf{r})) \langle p_i^a | \tilde{\Psi} \rangle \quad (4.23)$$

where  $\phi_i^a(\mathbf{r})$  are the all-electron partial waves,  $\tilde{\phi}_i^a(\mathbf{r})$  are the pseudo partial waves and  $p_i^a$  is the projection function. A one centre expansion can also be produced to ultimately obtain the KS wavefunction as:<sup>268,269</sup>

$$\Psi(\mathbf{r}) = \tilde{\Psi} + \sum_a (\Psi^a(\mathbf{r} - \mathbf{R}^a) - \tilde{\Psi}^a(\mathbf{r} - \mathbf{R}^a)) \quad (4.24)$$

Additionally, this approach exploits the frozen core approximation to improve computational efficiency, while retaining accuracy by calculating the overlap density.



# 5

5

## Methodology

### Contents

---

<b>5.1</b>	<b>Vienna <i>Ab Initio</i> Simulation Package</b>	<b>77</b>
<b>5.2</b>	<b>Organic Cation Substitution</b>	<b>78</b>
<b>5.3</b>	<b>Geometric and Electronic Optimisation</b>	<b>78</b>
<b>5.4</b>	<b><i>Ab Initio</i> Molecular Dynamics</b>	<b>79</b>
5.4.1	Machine Learning Force Fields	80
<b>5.5</b>	<b>Thermodynamic Stability</b>	<b>80</b>
<b>5.6</b>	<b>Electronic Structure Calculations</b>	<b>81</b>
5.6.1	Density of States	81
5.6.2	Band Structures	82
5.6.3	Effective Masses	82
<b>5.7</b>	<b>Optical Calculations</b>	<b>83</b>
5.7.1	Dielectric Values and Optical Absorption	83
5.7.2	Spectroscopic Limited Maximum Efficiency	84
5.7.3	Band Alignment	85

---

### 5.1 Vienna *Ab Initio* Simulation Package

All calculations in this report are calculated using a DFT framework using VASP, which uses a plane wave code where interactions between ion cores and valence are

described by the PAW method.<sup>267,268</sup> VASP includes many features which are used extensively in this report including DFT and HDFT. These techniques allow for calculations of electronic and optical properties described below.

## 5.2 Organic Cation Substitution

To produce hybrid organic-inorganic chalcogenide perovskites, molecular substitution was implemented using the Pymatgen<sup>270</sup> python library which is an object orientated code used to represent and manipulate crystal and molecular structures to obtain material properties. These organic molecules are then used to replace the inorganic A-site atom. The organic cations used in this report had an oxidation state of +1 or +2 dependent on the charges of the B and X-sites to ensure neutrality. The molecules used ranged in size to understand the effects of effective radii on the stability of hybrid chalcogenide perovskite. Theoretically suitable compound structures were then generated in the cubic phase. The suitable organic molecules are then substituted into a perovskite structure taking and used for further analysis.

## 5.3 Geometric and Electronic Optimisation

Geometric and electronic structure relaxations are a critical prerequisite to understanding the properties of materials as they largely determine the accuracy of the calculations by optimisation of the ground state atomic positions. The  $k$ -point, plane wave basis set and the crystal structure must all be converged to ensure accurate results. As a crystal can be considered periodic in reciprocal space, VASP uses Monkhorst-Pack grids to sample the Brillouin zone. A denser  $k$ -point mesh grid improves accuracy at the expense of computational resources. The convergence for the  $k$ -point grid is satisfied when the difference in total energy between succes-

sive  $k$ -point meshes becomes less than 1 meV/atom. The values of the converged  $k$ -points will be dependent upon each structure and can be seen in table 6.6. The plane wave basis set in VASP is defined by the energy cutoff value that represents the electronic wavefunctions by determining the maximum kinetic energy of the plane waves. To ensure all required plane waves are included in the calculation a converged plane wave cut-off value was accepted when the total energy was less than 5 meV/atom. The geometric optimisations then iterates to find the ground state energy value. The wavefunctions are expanded in the plane wave up to a cutoff energy of 1.3 times the converged cut off value to account for Pulay stress errors.<sup>271</sup> The exchange-correlation function used is the GGA of Perdew, Burke and Ernzerhof.<sup>255</sup> Specifically, the revised version, PBEsol was used as it is a functional optimised for better accuracy in solid-state system. Atoms were relaxed until Hellmann Feynman forces on them were below  $0.01 \text{ eV}\text{\AA}^{-1}$  and the total energy is converged to  $1 \times 10^{-5} \text{ eV}$ .<sup>257</sup>

## 5.4 *Ab Initio* Molecular Dynamics

Molecular dynamics is a numerical method for studying many-particle systems by evolving atomic positions with a thermostat. In AIMD, this process includes a full quantum calculation of the electronic structure at every time step. It is generally limited by computational cost as it requires large systems over long time steps to maximise accuracy. AIMD simulations are carried out in this report on the hybrid chalcogenide perovskites which maintain a stable structure after geometric and electronic relaxation to observe the motion of  $4 \times 4 \times 4$  hybrid perovskite supercells. A large supercell is required to prevent finite size effects. The simulations are carried out using Langevin dynamics in the isothermal-isobaric ensemble under a constant temperature, pressure and number of particles using methods by Parrinello and Rahman.<sup>272,273</sup> A Langevin thermostat at 300 K is used in each simulation with a

runtime of 10 ps at a step size of 0.5 fs, requiring 20,000 molecular dynamics (MD) steps. A single  $k$ -point at the  $\Gamma$ -point ( $k= 0,0,0$ ) is used to improve computational efficiency.

### 5.4.1 Machine Learning Force Fields

AIMD has a much higher accuracy compared to classical MD at the cost of increased computational resources, limiting its capabilities to small systems.<sup>274</sup> In this report many of the molecular dynamic simulations are run with systems with compounds which have in excess of 750 atoms. To reduce computational time, machine learning force fields (MLFF)s have been implemented to model the dynamics of chalcogenides. By taking advantage of on-the-fly learning, only a fraction of the of the force calculations are completed by DFT, while the remainder by the MLFF.<sup>275,276</sup> Similar to as the AIMD, the MLFF uses an isothermalisobaric ( $NpT$ ) ensemble with the Langevin thermostat and a time step of 0.5 fs was used during the training process. The force field was initially trained from the ground state at 300 K.

## 5.5 Thermodynamic Stability

A system is thermodynamic stable when it is in its lowest energy state and cannot be further reduced through phase segregation into competing phases or through a phase transition into a new crystal structure.<sup>277</sup> In this report, we will calculate the thermodynamic stability with respect to the competing phases using the convex hull formalism, calculated using the Doped software.<sup>278</sup> For each compound, the ground state energies of the subsequent competing phases are calculated using a converged  $k$ -mesh and using the PBEsol functional. Additionally the formation energy,  $\Delta E_f$ , of each  $ABX_3$  compound is calculated using the formula:<sup>277</sup>

$$\Delta E_{f,ABX_3} = E_{ABX_3} - E_A - E_B - 3E_X \quad (5.1)$$

An  $\Delta E_f < 0$  would indicate the compound is stable with respect to the elemental phases. The energy above hull is a concept used to describe the thermodynamic stability of a compound relative to other possible phases in a multi-component system.<sup>277</sup> A compound can have a negative formation energy but a positive energy above hull, indicating a metastable phase which could further decompose, whereas an energy above hull of 0.0 eV indicates that the compound is thermodynamically stable and lies on the convex hull on a phase diagram which is the lowest energy configuration for that specific composition.<sup>277</sup>

## 5.6 Electronic Structure Calculations

### 5.6.1 Density of States

The Density of States (DOS) is a common property utilised in quantum systems to measure the number of electronic states available at a given energy in a known volume, for a infinitesimal energy change.<sup>279</sup> Calculations were made using the HSE06 which incorporating 25% HF exchange to improve the bandgap predictions. HSE06 is used in all electronic property calculations in this report. The DOS gives information on the valence states which contribute to the electronic structure. The available states near the VBM and CBM can then be plotted to obtain a bandgap value. Additionally, the PDOS values can be used to understand the exact states which contribute the most available states. Intense, narrow peaks indicate high localisation and little interaction with other states, while wide density of states with flatter regions indicates strong hybridisation between states. All the DOS plots in

this report include a Gaussian smearing of value of 0.1 eV. This report uses self consistent static calculations using the *tetrahedron method* with Blöchl corrections.

## 5.6.2 Band Structures

Band structures are used to represent the electronic energy levels of solid materials to derive a materials conduction properties, possession of a direct or indirect bandgap as well as the mobility of charge carrier through those bands based on the curvature.<sup>280</sup> These band energies reside in  $k$ -space, where all the unique  $k$ -vectors comprise the Brillouin zone of that particular crystal. To effectively understand the electronic structure, high symmetry points in the Brillouin zone within the Bravais lattice are chosen. As each Brillouin zone has a unique space group, the high symmetry points are tailored to each particular space group.<sup>281,282</sup> Energy eigenvalues are then calculated across different  $k$ -points. The higher number of  $k$ -points the more accurate the structure however, due to computational limits finite numbers of  $k$ -points are chosen. Within a band structure plot, strong dispersion's are an indication of orbital overlaps from strong interactions between atoms, whereas flatter bands indicate weak interactions.

## 5.6.3 Effective Masses

The band edges can also be used to determine the effective masses of the electron and hole carriers. A high dispersion results in highly delocalised electrons and holes and hence, a high carrier mobility, a highly desirable property in PVs. This relationship between the energy,  $E$ , and the wavevector,  $k$ , for a free electron can be described in terms of the electron mass,  $m_e$ , as:

$$E(k) = \frac{\hbar^2 k^2}{2m_e} \quad (5.2)$$

where  $\hbar$  is the reduced Planck's constant and  $m_e$  is the electron mass. This is known as the dispersion relation and can be double differentiated with respect to  $k$ , to obtain:

$$\frac{d^2E(k)}{dk^2} = \frac{\hbar^2}{m_e} \quad (5.3)$$

This equation is parabolic and thus the reciprocal of the effective mass determines the curvature of the dispersion relationship. It is also important to note that there can be multiple effective masses in a material, which arise from the directional anisotropy in the crystal lattice. Therefore, to calculate a single effective electron and hole mass a harmonic mean,  $H$ , is used, where:

$$H = \frac{n}{\sum_{i=1}^n \frac{1}{x_i}} \quad (5.4)$$

and  $x$  is the effective mass and  $n$  is a positive integer value. This harmonic mean is used as it gives a more realistic average weighting for the effective masses as it has more emphasis on smaller effective masses, which play a more significant role in determining charge carrier mobility.

## 5.7 Optical Calculations

### 5.7.1 Dielectric Values and Optical Absorption

The optical absorption of a material is an intrinsic property relating to the energy exchange process of photons from incident light to electrons within the material lattice.<sup>283</sup> The dielectric constant,  $\epsilon_0$ , is an important parameter which is used to dictate the frequency-dependent optical absorption. The dielectric constant is com-

prised of two parts, the high-frequency dielectric response,  $\varepsilon_\infty$ , and the low frequency dielectric response,  $\varepsilon_{\text{ionic}}$ , where:<sup>283</sup>

$$\varepsilon_0 = \varepsilon_\infty + \varepsilon_{\text{ionic}} \quad (5.5)$$

The high-frequency dielectric values are tensors based on the crystal symmetry and calculated through the refraction of electromagnetic waves with frequencies much higher than the phonon lattice vibrations. The low-frequency ionic dielectric constant calculates the response of phonons under an applied electric field and is calculated using DFPT within the PBEsol framework. Additionally, a tight force convergence criteria is used to calculate  $\varepsilon_{\text{ionic}}$  as the crystal structure must be well converged to produce accurate results. The optical absorption is calculated with respect to the frequency dependent dielectric matrix and is an important property for photovoltaic absorber materials. The optical absorption coefficient,  $\alpha$ , measures the optical absorption as a function of photon energy. To be suitable for thin film photovoltaics the absorption coefficient should be in the order of  $10^5 \text{ cm}^{-1}$  and have a sharp absorption edge.

### 5.7.2 Spectroscopic Limited Maximum Efficiency

The SLME is a semi-empirical method which uses the detailed balance limit, absorption coefficient, recombination rates and bandgap value to determine the theoretical efficiency of a solar absorber.<sup>284,285</sup> The SLME is a more realistic estimate of a solar cell's efficiency compared to the Shockley-Queisser method, as it includes material properties and the non-idealities present in solar cells. It is a particularly useful metric for evaluating novel photovoltaic materials and structures, as it is based solely on intrinsic material properties such as; band gap, absorption spectra and

material-dependant non-radiative recombination losses.

### 5.7.3 Band Alignment

The band alignment is a technique used to measure the ionisation potential (IP), electron affinity (EA) and work functions,  $\Phi$ , of a solar absorber. Band alignments are important characteristics of solar cells, as they can be used to determine suitable contact materials and predict whether the material will be preferentially *n* or *p*-type doped. The IP is defined as the energy required to remove an electron from the VB to the vacuum and is calculated by:

$$\text{IP} = \Delta E_{\text{slab}} - \Delta E_{\text{bulk}} = (E_{\text{vac}} - E_{\text{core, slab}}) - (E_{\text{VBM}} - E_{\text{core, bulk}}) \quad (5.6)$$

The EA is described as the energy gained from adding an electron into the conduction band and is calculated by  $\text{IP} - E_g$ .  $E_{\text{vac}}$  is the vacuum energy level and  $E_{\text{core, slab}}$  is the energy in the core level within the bulk-like surface slab.  $E_{\text{VBM}}$  is the valence band maximum of the bulk and  $E_{\text{core, bulk}}$  is the bulk core level energy.<sup>286</sup> To obtain the values of the IP and EA they must be calculated with respect to the vacuum, as within VASP all eigenvalues are relative to the average background electrostatic potential. Band alignments were calculated using the slab-vacuum model, in which the surfaxe code<sup>286</sup> was utilised to generate a 2D slab of material in contact with a vacuum along the plane with lowest surface energy (calculated by a PBEsol relaxation). The vacuum used is 30 Å in thickness, to negate any interactions from periodical stacked slabs.<sup>1</sup> The bandgap of the slab with the lowest energy is calculated using the HSE06 functional to obtain the bandgap. Equation 5.6 can then be used to calculate the IP and then the EA.



# 6

## Results and Discussion

6

### Contents

---

6.1	Inorganic Chalcogenide Perovskites . . . . .	87
6.2	Hybrid Organic-Inorganic Chalcogenide Perovskites . .	93
6.3	Material Screening . . . . .	94
6.4	Geometric and Electronic Optimisation . . . . .	95
6.5	Electronic Properties . . . . .	98
6.6	Optical Properties . . . . .	106
6.7	<i>Ab Initio</i> Molecular Dynamics . . . . .	109
6.8	Thermodynamic Properties . . . . .	110
6.9	Band Alignments . . . . .	112
6.10	HZ(Zr, Hf)(S, Se) <sub>3</sub> Trends . . . . .	113
6.10.1	Chemical Composition Analysis . . . . .	113
6.10.2	Charge Density Analysis . . . . .	115

---

### 6.1 Inorganic Chalcogenide Perovskites

This section contains the results from two inorganic chalcogenide perovskites, namely BaZrS<sub>3</sub> and BaHfS<sub>3</sub>. These specific compounds were chosen as they have been experimentally verified in previous work, as seen in table 2.2.<sup>8,16,149,150,156</sup> By com-

paring the computational results in this report with verified experimental data, the accuracy of the calculation parameters can be validated. Once completed, similar parameters can be applied to the hybrid compounds to predict the properties of new chalcogenide perovskites which have not been experimentally verified. This ensures that the computational approaches in this report are accurate and reliable. Table 6.1 shows the converged properties for the inorganic chalcogenides mentioned ( $\text{BaZrS}_3$  and  $\text{BaHfS}_3$ ), adhering to the geometric and electronic parameters mentioned in section 5.3.

Table 6.1: Calculation parameters for  $\text{BaZrS}_3$  and  $\text{BaHfS}_3$ .

Compound	Structure	Space group	Cut-off (eV)	k-point mesh
$\text{BaZrS}_3$	Orthorhombic	$Pnma$	300	$3 \times 3 \times 4$
$\text{BaHfS}_3$	Orthorhombic	$Pnma$	300	$4 \times 3 \times 4$

The geometries of these structures were then optimised using the PBEsol functional. The associated lattice parameters can be seen in table 6.2. In both compounds the calculated lattice parameters are within 1% of experimental values, making the parameters suitable for subsequent usage on theoretical compounds. Figure 6.1 shows the optimised structures of  $\text{BaZrS}_3$  and  $\text{BaHfS}_3$ . Both chalcogenide perovskites exhibit  $a^-b^+a^-$  octahedral tilting in the orthorhombic phase, reducing symmetry and altering bond angles and lengths. This tilting influences the band structure and electronic properties which will be further discussed in section 6.10.

Table 6.2: Calculated lattice parameters and respective deviations from experimental values.<sup>16</sup>

Compound	a (Å)	b (Å)	c (Å)
$\text{BaZrS}_3$	7.074 (+0.18%)	9.923 (-0.56%)	6.962 (-0.88%)
$\text{BaHfS}_3$	6.998 (-0.15%)	9.862 (-0.56%)	6.938 (-0.91%)

The DOS and band structures were then calculated using the HSE06 functional for both  $\text{BaZrS}_3$  and  $\text{BaHfS}_3$  and can be seen in Figure 6.2. In the DOS plots, the valence states contributing to the electronic structure are split into partial DOS

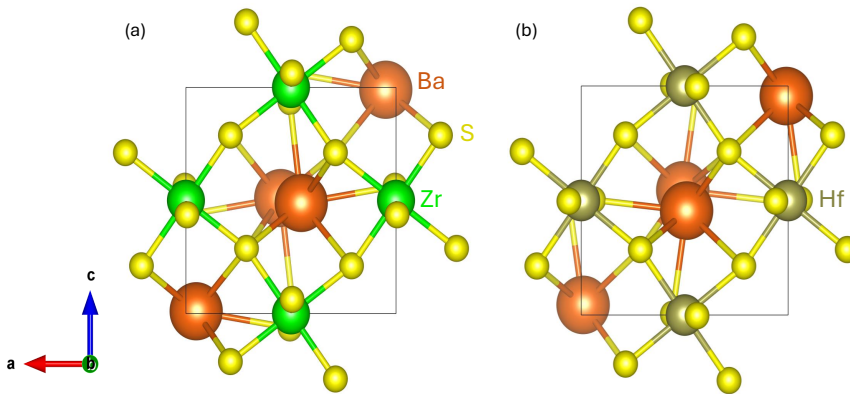


Figure 6.1: Optimised structure of (a) BaZrS<sub>3</sub> and (b) BaHfS<sub>3</sub>.

6

contributions, giving the proportion of each particular state. In the case of BaZrS<sub>3</sub>, the partial DOS is divided into Ba *d*-states, S *p*-states and Zr *d*-states. The relative proportion of these states can then be used to determine the state contributions over the range of energy values. The DOS of BaZrS<sub>3</sub> shows a bandgap of 1.77 eV, aligning closely with experimental results of 1.75 eV<sup>8</sup> and 1.79 eV<sup>148</sup> which can be attributed to the accuracy of the HSE06 functional. The valence band is dominated by S 3*p*-states while the conduction band mainly consists of Zr 4*d*-states.

The band structure in Figure 6.2b depicts the valence band in blue and the conduction band in orange. The regions of interest within the band structures are around the band edges which dictate the bandgap and are seen to be in agreement with the DOS plot. The VBM occurs at the  $\Gamma$ -point (0, 0, 0) in *k*-space. The occupied valence bands from 0 to -2 eV in BaZrS<sub>3</sub> lack dispersion as they are relatively flat, due to the localised S *p* states. The CBM also lies on the  $\Gamma$ -point, resulting in BaZrS<sub>3</sub> being a direct bandgap semiconductor. The CBM also displays more dispersive bands at energy levels from 1.78–3 eV. This can be attributed to broader DOS from an overlap of Zr *d*-states with S *p*-states resulting in delocalisation and therefore a higher dispersion. The higher dispersion results in lower electron effective mass ( $m_e$ ) with a value of  $0.38m_0$  compared to a hole effective mass ( $m_h$ ) of  $0.48m_0$ .

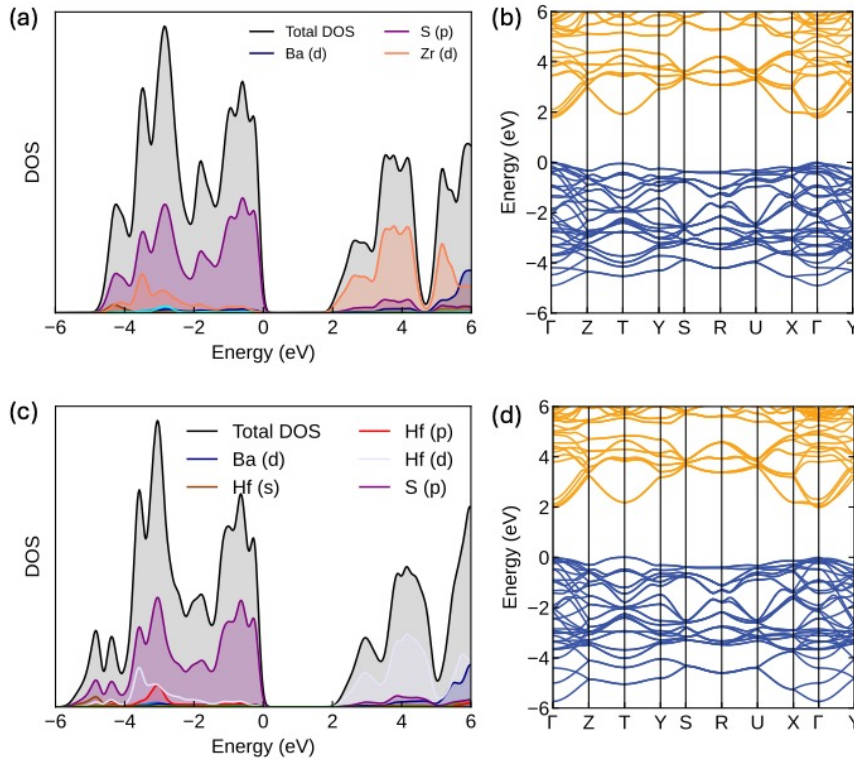


Figure 6.2: Partial density of states and band structure of (a-b) BaZrS<sub>3</sub> and (c-d) BaHfS<sub>3</sub>.

in the less dispersed valence band, aligning well with the results by Huo et al.<sup>6</sup>

Figure 6.2c shows the DOS plot for BaHfS<sub>3</sub> where the valence band also consists of S *p*-states while the conduction band is dominated by Hf *d*-states. The bandgap is slightly larger with a bandgap of 1.98 eV, agreeing well with experimental bandgaps of 2.06 eV.<sup>156</sup> The band structure in Figure 6.2d is similar to that of BaZrS<sub>3</sub> with strong dispersions in the CBM resulting in an electron effective mass of  $0.29m_0$ . The VB on the other hand exhibits a hole effective mass of  $2.41m_0$ . This increase in  $m_h$  can be attributed to the valence band minimum being located at the T point rather than the  $\Gamma$ -point as seen in BaZrS<sub>3</sub>. This makes BaHfS<sub>3</sub> a slightly indirect semiconductor, however it will still have desirable absorption properties due to the presence of a direct bandgap seen at 1.99 eV at the  $\Gamma$ -point. Table 6.3 summarises

the electronic properties of  $\text{Ba}(\text{Zr}, \text{Hf})\text{S}_3$ .

Table 6.3: The calculated direct bandgap ( $E_g^d$ ), indirect bandgap ( $E_g^i$ ), electron effective mass ( $m_e$ ) and hole effective mass ( $m_h$ ) for inorganic chalcogenide perovskites. Effective masses are in units of rest mass ( $m_0$ ).

Compound	$E_g^d$ (eV)	$E_g^i$ (eV)	$m_e/m_0$	$m_h/m_0$
BaZrS <sub>3</sub>	1.77	—	0.30	0.48
BaHfS <sub>3</sub>	1.99	1.98	0.29	2.41

The absorption spectra for  $\text{Ba}(\text{Zr}, \text{Hf})\text{S}_3$  can be seen in Figure 6.3. Both compounds exhibit strong absorption coefficients, represented by the sharp absorption edge which climbs to above  $10^5 \text{ cm}^{-1}$  within 0.5 eV above the onset of absorption, complementing well with experimental literature.<sup>16,149,217,287</sup> These absorption coefficients outperform current solar absorbers such as  $\text{MAPbI}_3$ , gallium arsenide (GaAs) and CdTe.<sup>288</sup> This high absorption can be attributed to the direct nature of the bandgaps in both materials along with the high JDOS. This efficient light absorption can lead to improved quantum efficiencies, allowing for thinner absorption layers to be used.<sup>14,16</sup>

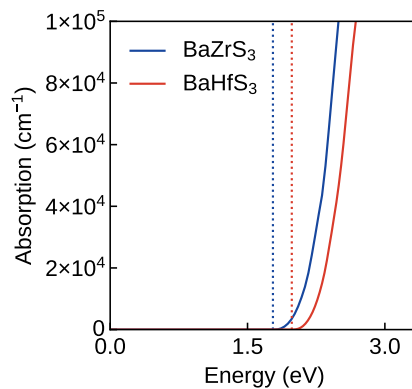


Figure 6.3: HSE06 calculated optical absorption spectra for  $\text{BaZrS}_3$  and  $\text{BaHfS}_3$  as a function of energy. Full lines indicate the optical absorption and dashed lines indicate the fundamental bandgap.

Additionally, the high-frequency dielectric constants,  $\varepsilon_\infty$ , and SLME were calculated and can be seen in table 6.4 and Figure 6.4. The SLME values are primarily based on the bandgap of the material. As  $\text{BaZrS}_3$  has a more suitable bandgap than  $\text{BaHfS}_3$  it will have a higher  $J_{sc}$  without compromising the  $V_{oc}$  and therefore have an increased efficiency. Furthermore,  $\text{BaZrS}_3$  exhibits a higher high-frequency dielectric constant and more desirable effective masses making it a superior choice over  $\text{BaHfS}_3$  for photovoltaic applications. Although a bandgap of 1.77 eV is too large for single junction cells,  $\text{BaZrS}_3$  would be more suited towards usage in Si/perovskite tandem solar cells.

## 6

Table 6.4: Optical properties of  $\text{BaZrS}_3$  and  $\text{BaHfS}_3$ . Includes high-frequency dielectric constants ( $\varepsilon_\infty$ ) along the X, Y and Z directions at 0 eV and the Spectroscopic Limited Maximum Efficiency (SLME).

Compound	X	Y	Z	SLME %
$\text{BaZrS}_3$	7.27	7.31	7.13	26.81
$\text{BaHfS}_3$	6.57	6.67	6.60	23.04

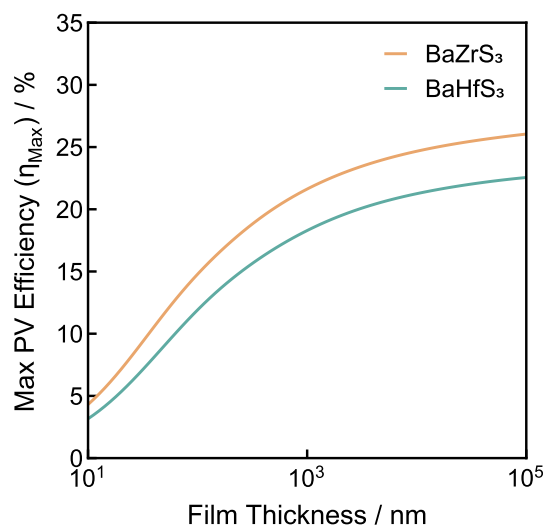


Figure 6.4: SLME for  $\text{BaZrS}_3$  and  $\text{BaHfS}_3$  as a function of film thickness, calculated using HSE06.

## 6.2 Hybrid Organic-Inorganic Chalcogenide Perovskites

As previously stated, lead halide perovskites currently are the highest performing single junction perovskite solar cells, although they suffer with long term stability and the use of Pb limits their widespread usage. Chalcogenide perovskites have been proposed as an alternative to these halide perovskites with large efforts being made in the field of fully inorganic chalcogenide materials. However, there has been a significant lack of literature on utilising organic molecules in the A-site of the  $\text{ABX}_3$  structure in replacement of inorganic atoms to form a hybrid structure. In this report, both monovalent cations and divalent cations were used in an attempt to form stable hybrid perovskite structures. For the monovalent compounds, A= organic cation; B= Bi, Sb; X= S, Se to form a  $\text{A}^{1+}\text{B}^{5+}\text{X}_3^{2-}$  perovskite. Bi was primarily used as the B-site cation due to the larger ionic radii 0.76 Å compared to Sb ionic radii of 0.60 Å for a 5<sup>+</sup> charge state.<sup>194</sup> This was required to increase the octahedral factor to above the threshold level of 0.41. The divalent structures took the form of  $\text{A}^{2+}\text{B}^{4+}\text{X}_3^{2-}$  where A= organic cation; B= Zr, Hf; X= S, Se. The B and X-sites were chosen due to their low toxicity and for the fact they are naturally abundant elements.

### 6.3 Material Screening

The initial search for organic cations focused on the divalent cations, which there are few of that are small enough to fit within the A-site. Additionally, many  $2^+$  charged organic cations can suffer from instability from the electron deficiencies and high ionisation energies required to remove the electrons to form a divalent molecule. Although there are some stable divalent cations they generally have an effective radii too large to satisfy the Goldschmidt tolerance factor. Therefore only two such dication were found to be stable and applicable for our use case;  $(\text{NH}_3-\text{NH}_3)^{2+}$  and  $(\text{NH}_3-\text{CH}_2-\text{NH}_3)^{2+}$ , known as Hydrazinium and Azaniumylmethyazanium, respectively. Due to the scarcity of divalent cations, we initially focused on using monovalent cations, which are far more plentiful. The caveat of using these cations, results in the B-site cation being pentavalent to ensure charge neutrality. Therefore, Bi and Sb were chosen which both have stable  $5^+$  charge states. The organic monovalent cations were chosen can be seen below in table 6.5. As emphasised by Park et al.<sup>7</sup> an A-site cation with a small effective radii is desirable in chalcogenide perovskites due to the rapid increases of structural deformation as the A-site molecule radii increases. This constraint also reduces the number of potential cations that would be suitable for chalcogenide perovskites. Using these organic cations with different B and X-sites yielded 50 unique structures which were produced using the Pymatgen code.<sup>270</sup>

Table 6.5: Organic cations used as an A-site molecules in the  $\text{ABX}_3$  perovskite structure.  
All molecular weights were taken from Ref. 17.

Cation	Shortname	Molecular weight (g/mol)	Molecular Formula
Hydronium	$\text{HY}^+$	19.02	$[\text{H}_3\text{O}]^+$
Ammonium	$\text{AM}^+$	18.04	$[\text{NH}_4]^+$
Phosphonium	$\text{PH}^+$	35.00	$[\text{PH}_4]^+$
Hydroxylammonium	$\text{HA}^+$	34.04	$[\text{NH}_3\text{OH}]^+$
Methylammonium	$\text{MA}^+$	32.06	$[\text{CH}_3\text{NH}_3]^+$
Hydrazinium	$\text{HZ}^+$	33.05	$[\text{NH}_3\text{NH}_2]^+$
Formamidinium	$\text{FA}^+$	45.08	$[\text{CH}(\text{NH}_2)_2]^+$
Formamide cation	$\text{FO}^+$	46.06	$[\text{NH}_3\text{COH}]^+$
Ethylammonium	$\text{EA}^+$	45.1	$[\text{CH}_3\text{CH}_2\text{NH}_3]^+$
Aziridinium	$\text{AZ}^+$	44.08	$[\text{NH}_2(\text{CH}_2)_2]^+$
Azetidinium	$\text{AZE}^+$	58.10	$[\text{NH}_2(\text{CH}_2)_3]^+$
Dimethylazanium	$\text{DMA}^+$	46.09	$[\text{NH}_2(\text{CH}_3)_2]^+$
Trimethylazanium	$\text{TMA}^+$	60.12	$[\text{NH}(\text{CH}_3)_3]^+$
Tetramethylazanium	$\text{TTMA}^+$	74.14	$[\text{N}(\text{CH}_3)_4]^+$
Cyclopropylammonium	$\text{CA}^+$	58.10	$[\text{NH}_3\text{CH}(\text{CH}_2)_2]^+$
Pyrrolidinium	$\text{PY}^+$	72.13	$[\text{NH}_2(\text{CH}_2)_4]^+$
Methylhydrazinium	$\text{MH}^+$	47.08	$[\text{CH}_3\text{NH}_2\text{NH}_3]^+$
Methaniminium	$\text{MAM}^+$	30.05	$[\text{CH}_2\text{NH}_2]^+$
Hydroxy(methylidene)azanium	$\text{HMA}^+$	58.06	$[\text{CH}_2\text{NHOH}]^+$
Hydrazinium	$\text{HZ}^{2+}$	34.06	$[\text{NH}_3\text{NH}_3]^{2+}$
Azaniumylmethylazanium	$\text{AMZ}^{2+}$	48.11	$[\text{CH}_2(\text{NH}_3)_2]^{2+}$

## 6.4 Geometric and Electronic Optimisation

The geometries of all 50 crystal structures were optimised using the PBEsol functional to ensure the compounds were in their ground state, using a cutoff energy of 500 eV and a converged  $k$ -point. Once completed, the structures which maintained an  $\text{ABX}_3$  perovskite structure with corner-sharing octahedra were used for further analysis. Table 6.6 shows the 50 initial compounds investigated in this report and their respective phase formations after geometric relaxations.

As seen the vast majority of compounds examined do not produce a perovskite structure and instead form non-perovskite structures as a result of bonds breaking from large distortions in the crystal structure structure. The monovalent cations which retained a perovskite structure were hydronium ( $\text{HY}^+$ ), ammonium ( $\text{AM}^+$ ), hydroxylammonium ( $\text{HA}^+$ ) and methaniminium ( $\text{MAM}^+$ ) which have effective radii

Table 6.6: The 50 compounds examined in this report with their converged k-points and phases formed after geometric optimisation and electronic convergence. The cutoff energy for all compounds was 500 eV. The compounds are split into sulphur and selenium based perovskites. The upper rows separated by the horizontal black line represent monovalent cations while the lower rows are compounds with divalent A-site cations.

ABS <sub>3</sub> perovskites			ABSe <sub>3</sub> perovskites		
Compound	k-point	Phase	Compound	k-point	Phase
HY SbS <sub>3</sub>	9 × 9 × 9	Orthorhombic	HY SbSe <sub>3</sub>	7 × 7 × 7	Non-perovskite
HY BiS <sub>3</sub>	8 × 8 × 8	Orthorhombic	HY BiSe <sub>3</sub>	8 × 8 × 8	Orthorhombic
AM SbS <sub>3</sub>	9 × 9 × 9	Non-perovskite	AM SbSe <sub>3</sub>	6 × 6 × 6	Non-perovskite
AM BiS <sub>3</sub>	9 × 9 × 9	Non-perovskite	AM BiSe <sub>3</sub>	8 × 8 × 8	Monoclinic
PH BiS <sub>3</sub>	9 × 9 × 9	Non-perovskite	PH BiSe <sub>3</sub>	9 × 9 × 9	Non-perovskite
HABiS <sub>3</sub>	9 × 9 × 9	Non-perovskite	HABiSe <sub>3</sub>	6 × 6 × 6	Monoclinic
MABiS <sub>3</sub>	6 × 6 × 6	Non-perovskite	MABiSe <sub>3</sub>	6 × 6 × 6	Non-perovskite
HZ BiS <sub>3</sub>	7 × 7 × 7	Non-perovskite	HZ BiSe <sub>3</sub>	7 × 7 × 7	Non-perovskite
FABiS <sub>3</sub>	9 × 9 × 9	Non-perovskite	FABiSe <sub>3</sub>	10 × 10 × 10	Non-perovskite
FOBiS <sub>3</sub>	8 × 8 × 8	Non-perovskite	FOBiSe <sub>3</sub>	7 × 7 × 7	Non-perovskite
EABiS <sub>3</sub>	7 × 7 × 7	Non-perovskite	EABiSe <sub>3</sub>	7 × 7 × 7	Non-perovskite
AZ BiS <sub>3</sub>	7 × 7 × 7	Non-perovskite	AZ BiSe <sub>3</sub>	7 × 7 × 7	Non-perovskite
AZEBiS <sub>3</sub>	8 × 8 × 8	Non-perovskite	AZEBiSe <sub>3</sub>	9 × 9 × 9	Non-perovskite
DMABiS <sub>3</sub>	7 × 7 × 7	Non-perovskite	DMABiSe <sub>3</sub>	7 × 7 × 7	Non-perovskite
TMABiS <sub>3</sub>	10 × 10 × 10	Non-perovskite	TMABiSe <sub>3</sub>	5 × 5 × 5	Non-perovskite
TTMABiS <sub>3</sub>	5 × 5 × 5	Non-perovskite	TTMABiSe <sub>3</sub>	5 × 5 × 5	Non-perovskite
CABiS <sub>3</sub>	8 × 8 × 8	Non-perovskite	CABiSe <sub>3</sub>	8 × 8 × 8	Non-perovskite
PY BiS <sub>3</sub>	6 × 6 × 6	Non-perovskite	PY BiSe <sub>3</sub>	7 × 7 × 7	Non-perovskite
MH BiS <sub>3</sub>	7 × 7 × 7	Non-perovskite	MH BiSe <sub>3</sub>	7 × 7 × 7	Non-perovskite
MAMBiS <sub>3</sub>	6 × 6 × 6	Non-perovskite	MAMBiSe <sub>3</sub>	9 × 9 × 9	Monoclinic
HMABiS <sub>3</sub>	9 × 9 × 9	Non-perovskite	HMABiSe <sub>3</sub>	9 × 9 × 9	Monoclinic
HZZrS <sub>3</sub>	6 × 6 × 6	Monoclinic	HZZrSe <sub>3</sub>	5 × 5 × 5	Monoclinic
HZ HfS <sub>3</sub>	6 × 6 × 6	Monoclinic	HZ HfSe <sub>3</sub>	5 × 5 × 5	Monoclinic
AMZZrS <sub>3</sub>	5 × 5 × 5	Non-perovskite	AMZZrSe <sub>3</sub>	5 × 5 × 5	Non-perovskite
AMZHfS <sub>3</sub>	6 × 6 × 6	Non-perovskite	AMZHfSe <sub>3</sub>	5 × 5 × 5	Non-perovskite

of 140 pm, 146 pm, 216 pm and 216 pm, respectively.<sup>196</sup> The combination of a small effective mass and low molecular weight allows the perovskite structure to be maintained, coinciding with the results found by Park et al.<sup>7</sup>. As the effective radius increased to over 220 pm, the stability declined sharply with no other monovalent cations being stable. The large number of non-perovskites can also be attributed to the small ionic radii of Bi and Sb in their 5<sup>+</sup> charge state resulting in low octahedral factors which can be an indication of instability from large distortions in the octahedral cage. Furthermore, geometric optimisation calculations are completed at low temperatures where organic molecules cannot be interpreted as spheres and therefore the non-spherical structure with the addition of hydrogen bonds can induce

symmetry breaking distortions.<sup>289</sup> As previously mentioned, small molecular cations have been shown to be more stable in chalcogenide perovskites, whereas halide perovskites are much more robust in terms of accommodating distortion.<sup>7</sup> This being due to the electronegativity differences between the B and X-site which is higher in chalcogenide perovskites, resulting in weaker covalent bonding and therefore a more fragile  $\text{BX}_6$  octahedra. This notion is further reinforced from the results in table 6.7, which show the stable perovskites all contain molecules with an effective radii ( $R_A$ ) below 217 pm as well as their respective lattice parameters. This trend continues in the divalent cation perovskites, as all the compounds containing hydrazinium,  $\text{HZ}^{2+}$  ( $\text{NH}_3 - \text{NH}_3^{2+}$ ) were geometrically stable while the Azaniumylmethylationazanium,  $\text{AMZ}^{2+}$  compounds containing an additional methylene bridge ( $\text{NH}_3 - \text{CH}_2 - \text{NH}_3^{2+}$ ) were all unstable in the same configurations, further alluding to the requirement of small organic cations for stable chalcogenide perovskites. All the perovskite forming compounds had a Goldschmidt tolerance factor of  $0.87 < t < 1.11$ , indicating a pseudocubic structure and an octahedral factor,  $\mu > 0.36$ , excluding  $\text{HYSbS}_3$  due to the presence of the small Sb atom. Although an octahedral factor of 0.41 is desirable, compounds can be stable with values slightly below, for example  $\text{BaZrS}_3$  ( $\mu = 0.39$ ). This is a result of the octahedral factor being designed for oxides rather than chalcogenides, skewing the lower bounds required to maintain an octahedral cage. The lattice parameters for the stable chalcogenide perovskites are given in table 6.8. Interestingly,  $\text{MA}^+$  did not stabilise within the  $\text{Bi}(\text{S}, \text{Se})_3$  octahedra which would have been expected given the small  $R_A$  of 217 pm.

Table 6.7: Effective radius ( $R_A$ ) and ionic radii ( $R_B, R_X$ ) used to calculate the tolerance factor ( $t$ ) and octahedral factor ( $\mu$ ) as well as the associated number of cation lone pairs ( $N_{LP}$ ) for the chalcogenide perovskites.

Compound	$R_A$ (pm)	$R_B$ (pm)	$R_X$ (pm)	$t$	$\mu$	$N_{LP}$
HYSbS <sub>3</sub>	140	60	184	0.93	0.30	1
HYBiS <sub>3</sub>	140	76	184	0.88	0.41	1
HYBiSe <sub>3</sub>	140	76	198	0.87	0.38	1
AMBiSe <sub>3</sub>	146	76	198	0.89	0.38	0
HABISe <sub>3</sub>	216	76	198	1.07	0.38	2
MAMBiSe <sub>3</sub>	216	76	198	1.07	0.38	1
HZZrS <sub>3</sub>	217	72	184	1.11	0.39	0
HZHfS <sub>3</sub>	217	71	184	1.11	0.39	0
HZZrSe <sub>3</sub>	217	72	198	1.09	0.36	0
HZHfSe <sub>3</sub>	217	71	198	1.09	0.36	0

## 6

Table 6.8: Lattice parameters for the stable chalcogenide perovskites calculated using PBEsol functional.

Compound	a (Å)	b (Å)	c (Å)	$\alpha(^{\circ})$	$\beta(^{\circ})$	$(\gamma)^{\circ}$
HYSbS <sub>3</sub>	10.040	9.969	10.146	90	90	90
HYBiS <sub>3</sub>	10.459	10.417	10.380	90	90	90
HYBiSe <sub>3</sub>	11.856	9.730	11.227	90	90	90
AMBiSe <sub>3</sub>	12.186	11.109	10.331	90	94.26	90
HABISe <sub>3</sub>	12.031	11.208	11.753	90	112.91	90
MAMBiSe <sub>3</sub>	12.075	10.026	11.400	90	89.99	90
HZZrS <sub>3</sub>	10.002	10.494	9.998	94.87	90	90
HZHfS <sub>3</sub>	9.957	10.405	9.914	94.79	90	90
HZZrSe <sub>3</sub>	10.416	10.907	10.476	93.86	90	90
HZHfSe <sub>3</sub>	10.374	10.836	10.379	93.99	90	90

## 6.5 Electronic Properties

As there is a lack of experimental results for the compounds investigated in this report, it is essential that the electronic structure predictions are accurate. Therefore, the HSE06 functional was used as it gave the most accurate results with respect to the well characterised inorganic chalcogenide perovskites. HSE06 is also the primary choice of functional as it known to be accurate at predicting the electronic structures of narrow and moderate bandgaps.<sup>262</sup> The electronic properties calculated include

the DOS, band structures and AIMD.

### Monovalent Cations

The chalcogenide perovskites in the  $\text{ABX}_3$  form where A= monovalent organic molecule, B= Bi, Sb and X= S, Se band structures and corresponding DOS can be seen in Figures 6.5a-f. From these figures it is evident the compounds where B= Bi, Sb exhibited poor properties for photovoltaic application. This is apparent from the band structure plots which show either a very small bandgap (Figures 6.5d, e) or the absence of any bandgap at all, indicating the compound is metallic (Figures 6.5a-c, f). The metallic structures are formed when there is an overlap between the VBM and CBM, preventing the formation of electron-hole pairs making them unsuitable for solar cells applications. The metallic nature of these compounds may be a result of the use of heavy elements such as Bi and Sb within the perovskite structure. As they contain partially filled *p*-orbitals, there is a strong overlap with the S or Se orbitals, indicated by the broad flatter regions within the DOS plots resulting in regions of strong hybridisation between states. This can then cause bands near the VB and CB edges to overlap. Additionally, those compounds with a metallic structure, all show large density of states at the Fermi level, as a result of high contributions from Bi and Sb orbitals, causing there to be higher charge carrier densities near the Fermi level, resulting in a metallic characteristics in these compounds.

$\text{AMBiSe}_3$  and  $\text{HABiSe}_3$  on the other hand both displayed semiconducting properties, however their bandgaps were very narrow, resulting in high thermalisation losses and low open circuit voltages making them poor candidates for solar cells.  $\text{AMBiSe}_3$  was calculated to have a direct bandgap of 0.348 eV and an indirect bandgap of 0.028 eV, far below the ideal bandgap range for photovoltaics.  $\text{HABiSe}_3$  had a slightly better direct bandgap of 0.516 eV and an indirect bandgap of 0.243 eV.

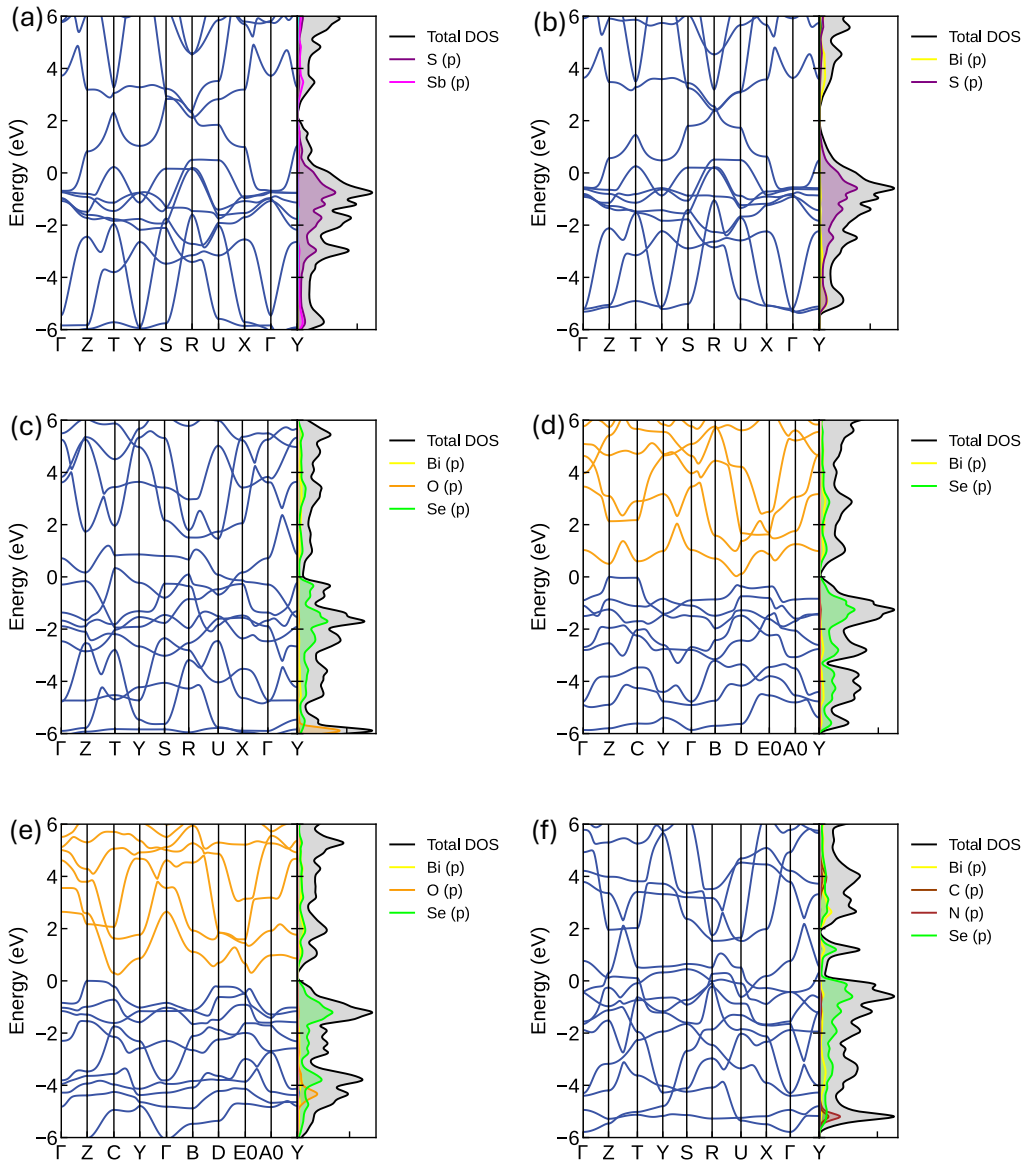


Figure 6.5: Hybrid chalcogenide perovskites with a stable perovskite structure and monovalent A-site cation calculated using HSE06. (a) HYsSb<sub>3</sub>, (b) HYBi<sub>3</sub>S, (c) HYBiSe<sub>3</sub>, (d) AMBiSe<sub>3</sub>, (e) HABiSe<sub>3</sub>, (f) MAMBiSe<sub>3</sub>.

Both materials have the indirect bandgaps given by the fact the valence band maxima are situated at the Z point, while the CBM is located between  $\Gamma$ -Y. The presence of an indirect bandgap in both materials result in lower photon absorption and reduced photocurrent generation, also limiting their PCE. Both materials did exhibit strong dispersions at the VBM and CBM resulting in small effective masses. AMBiSe<sub>3</sub> had an effective electron mass of  $0.22m_0$  and an effective hole mass of

0.15 $m_0$ , indicating high charge carrier mobilitys. HABiSe<sub>3</sub> also displayed desirable mobilitys with an effective electron mass of 0.28 $m_0$  and an effective hole mass of 0.15 $m_0$ .

### Divalent Cations

As mentioned, only two organic divalent cations were used in this report due to the scarcity of small divalent organic cations, arising from the chemical instability and reactivity of divalent cationic states. Many of the organic cations include nitrogen, which typically forms with three bonds and a lone pair, making the formation of a divalent cation less thermodynamically favourable. This resulted in only hydrazinium ( $\text{HZ}^{2+}$ ) being stable in a perovskite structure after geometric and electronic relaxation. These relaxed structures can be seen in Figure 6.6.

Although there were much fewer divalent organic cations to use in the chalcogenide perovskites it can be seen the variations of them were much more suitable for photovoltaic applications. Figures 6.7a-h display the PDOS and band structures for the four HZ based hybrid chalcogenides, namely; HZZrS<sub>3</sub>, HZZrSe<sub>3</sub>, HZHfS<sub>3</sub> and HZHfSe<sub>3</sub> all calculated using HSE06. These compounds can be seen to have superior properties compared to their monovalent counterparts. All four compounds exhibited direct bandgaps at the  $\Gamma$ -point, however also all formed a fundamental indirect bandgap, with the VBM being located at the C-point and the CBM at the  $\Gamma$ - point. This is a contrast to the inorganic BaZrS<sub>3</sub> which does not possess an indirect bandgap. The formation of this indirect bandgap is likely due to a combination of the exchange of Ba for the larger, HZ dication and a decreased structural tilting associated with this exchange in A-site cation. The decreased octahedral tilting in comparison to the BaZrS<sub>3</sub> may result in an increased anti-bonding character which will be further discussed in section 6.10.2. Although the formation of an indirect bandgap is undesirable, the HZ based perovskites showed strong photovoltaic prop-

6

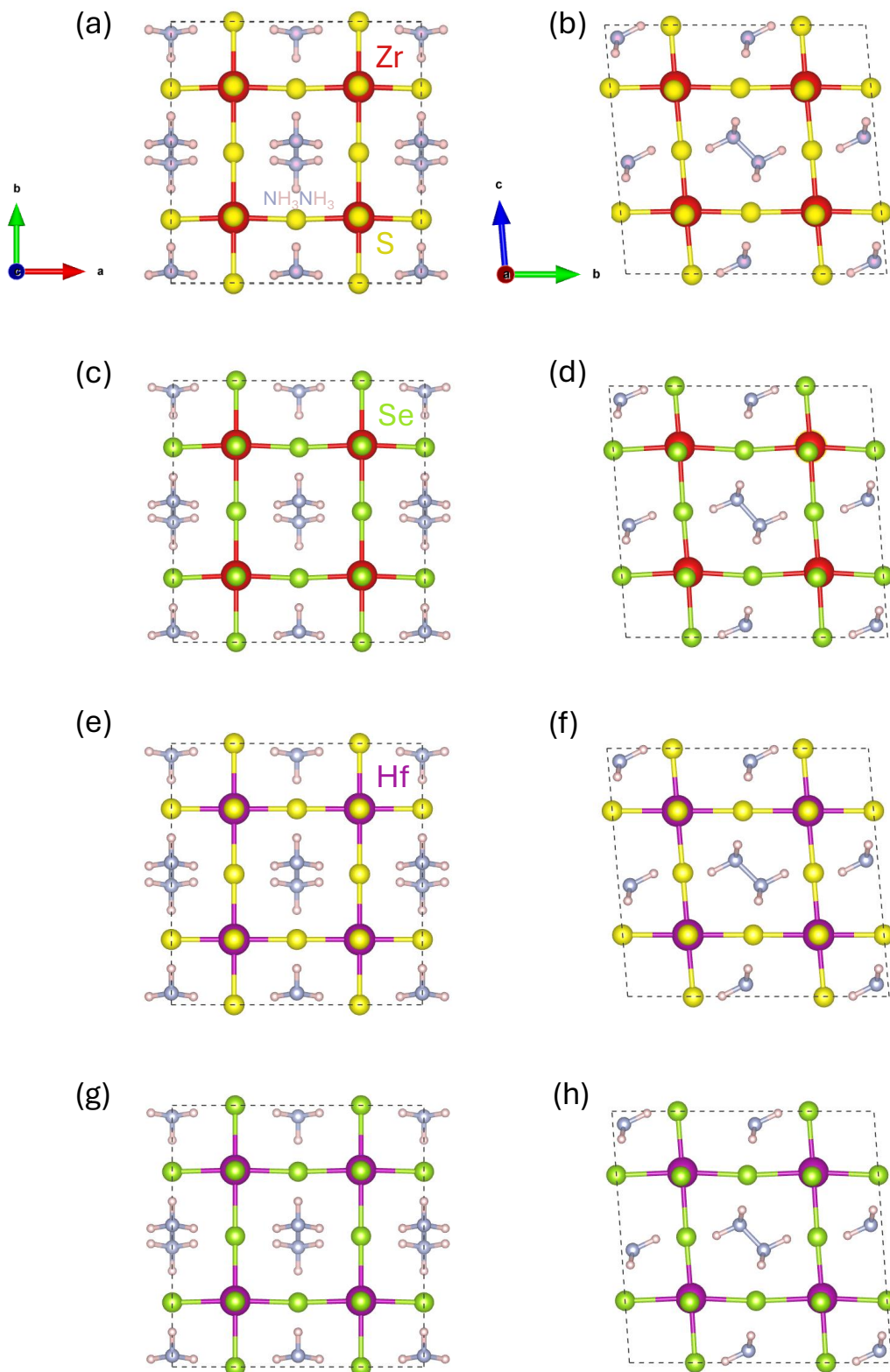


Figure 6.6: Atomic structures for optimised  $2 \times 2 \times 2$  supercells of HZ compounds. Calculations were completed using PBEsol functional. (a-b)  $\text{HZZrS}_3$ , (c-d)  $\text{HZZrSe}_3$ , (e-f)  $\text{HZHfS}_3$  and (g-h)  $\text{HZHfSe}_3$ .

erties as seen in table 6.9. In particular, HZZrS<sub>3</sub> had a calculated direct bandgap of 1.68 eV at the  $\Gamma$ -point, agreeing well with Sun et al.<sup>3</sup> bandgap calculation of 1.68 eV also.

Table 6.9: Electronic properties of hydrazinium based compounds. The direct and indirect bandgaps are given in eV, and the effective masses ( $m_e$  and  $m_h$ ) are given in units of the electron rest mass.

Compound	$E_g^d$ (eV)	$E_g^i$ (eV)	$m_e/m_0$	$m_h/m_0$
HZZrS <sub>3</sub>	1.68	1.18	0.38	0.49
HZZrSe <sub>3</sub>	1.38	0.70	0.30	0.40
HZHfS <sub>3</sub>	1.85	1.36	0.74	0.45
HZHfSe <sub>3</sub>	1.50	0.88	0.29	0.36

The DOS for HZZrS<sub>3</sub> is primarily comprised of S *p*-states in the VB with some additions of Zr *p*-states deeper in the VB. The CB is dominated by Zr *d*-states, particularly in the range of 2–4 eV with a small contribution from S *p*-states. The predominant S *p* character in the VB and Zr *d* character in the CB implies that the optical transitions will be comprised of charge transfers between these states. Small contributions are also made by the N *s* and *p*-states, indicating HZ does not contribute greatly to the frontier orbitals. Therefore, it can be implied HZ main role as the A-site cation is structural rather than electronic. HZZrSe<sub>3</sub> shows the VB dominated by Se *p*-states similar to the S *p*-states in HZZrS<sub>3</sub>. The CB remains comprised of Zr *d*-states, however display a more narrow peak, indicating greater localisation of states. A smaller bandgap of 1.38 eV is also seen due to the presence of Se. The HZHfS<sub>3</sub> DOS plot shows the S *p*-orbitals dominating the VB with some contribution from Hf *d* and *p*-states at deeper energy levels of –4 eV, whereas the CB is primarily Hf *d*-orbitals with contributions from S *p*-orbitals over a broad energy range (2–6 eV). The Hf *p*-states are only present in the VB and make up a small proportion of the DOS compared to the *d*-states. This is due to the *p*-orbitals being closer to the core and hence do not contribute as significantly to the VB. There is a small contribution by the Hf *p*-states at –4 eV as result of *p-d* hybridisation which is also seen in BaHfS<sub>3</sub> in Figure 6.2c. HZHfSe<sub>3</sub> displays a VB

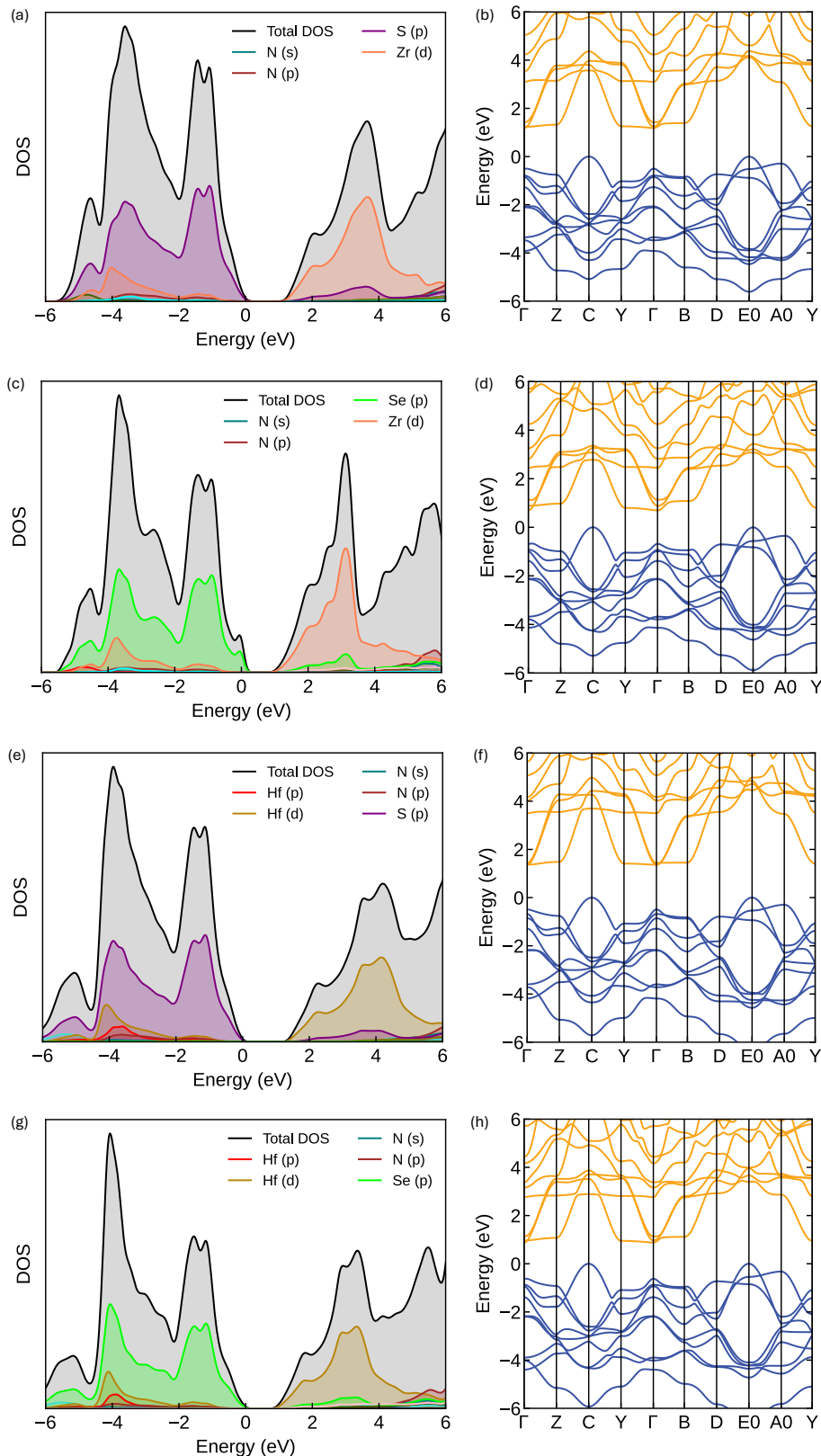


Figure 6.7: Partial density of states and band structure of (a-b) HZZrS<sub>3</sub>, (c-d) HZZrSe<sub>3</sub>, (e-f) HZHfS<sub>3</sub> and (g-h) HZHfSe<sub>3</sub>. All calculated using HSE06.

dominated by Se *p*-states similar to HZZrSe<sub>3</sub> and a CB also comprised of Hf *d*-states with a bandgap slightly larger than HZZrSe<sub>3</sub>. The delocalisation of states in the VB and CB of HZZrS<sub>3</sub> can be seen as strong dispersion's in the band structures resulting in an electron effective mass of  $0.38m_0$  and a hole effective mass  $0.49m_0$ . The band structure of HZZrSe<sub>3</sub> shows that the indirect bandgap is still maintained. The dispersion at the  $\Gamma$ -point looks to be stronger in the CBM, contributing to a lower electron effective mass of  $0.30m_0$  while the hole effective mass is  $0.40m_0$ . The conduction band of HZHfS<sub>3</sub> looks to be less dispersive than other band structures resulting in a higher electron effective mass of  $0.74m_0$ . The hole effective mass looks relatively unchanged compared to HZZr(S,Se)<sub>3</sub> with a value of  $0.45m_0$ . The dispersion in HZHfSe<sub>3</sub> are stronger than the other plots giving better effective masses of  $m_e^* = 0.29$  and  $m_h^* = 0.36$ . Due to the desirable properties seen in the HZ organic molecules, we also attempted to replace the B-site with other tetravalent cations such as Si<sup>4+</sup>, Ti<sup>4+</sup>, Ge<sup>4+</sup> and Sn<sup>4+</sup> in hopes of improving the electronic properties, however all of these configurations were unstable with both S and Se in the X-site.

## 6.6 Optical Properties

In this section we calculate the optical properties for the HZ based compounds as they have the most promising results of all the materials examined. The monovalent cations which did display semiconducting properties ( $\text{AMBiSe}_3$  and  $\text{HABiSe}_3$ ) displayed very small bandgaps and thus their optical properties would be suboptimal. Nonetheless, the optical absorption plot can be seen in Figure 6.8. As seen the onset of absorption occurs at an energy much greater than the fundamental bandgap, indicating poor absorption of photons. The  $\text{AMBiSe}_3$  had a negligible SLME of 0.01% while the  $\text{HABiSe}_3$  had an SLME of 2.68%.

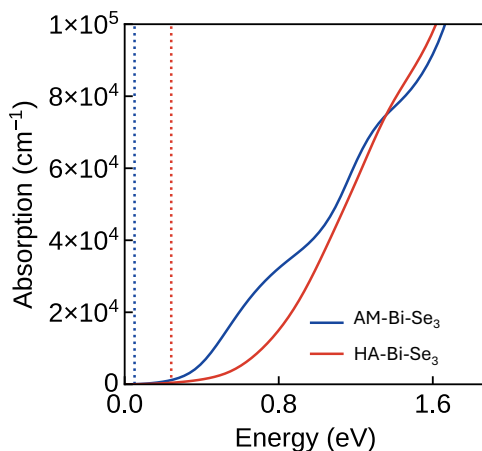


Figure 6.8: HSE06 calculated optical absorption spectra for  $\text{AMBiSe}_3$  and  $\text{HABiSe}_3$  as a function of energy. Full lines indicate the optical absorption and dashed lines indicate the fundamental bandgap

The HZ( $\text{Zr}, \text{Hf}$ )(S, Se)<sub>3</sub> group of chalcogenides exhibit superior optical properties compared to  $\text{AMBiSe}_3$  and  $\text{HABiSe}_3$ . All four of the HZ containing compounds optical absorptions and corresponding SLMEs can be seen in Figure 6.9a-b with  $\text{BaZrS}_3$  and  $\text{BaHfS}_3$  also included as a comparison. In Figure 6.9a, it can be seen that the absorption onset correlates well with the direct bandgap values of the compounds.  $\text{HZZrSe}_3$  has the lowest absorption onset, consistent with having the lowest bandgap of 1.38 eV while  $\text{HZHfS}_3$  has the highest energy onset, matching its

bandgap of 1.85 eV. The Se compounds ( $\text{HZZrSe}_3$ ,  $\text{HZHfSe}_3$ ) showed lower energy onsets due to their narrower bandgaps compared to the S containing compounds. Figure 6.9b shows that the sulfide materials exhibit higher efficiencies compared to selenides as a result of the more optimal bandgaps possessed by sulfide compounds. HZ compounds begin to plateau after 1000 nm indicating an absorption saturation point where additional thickness does not convert to a higher maximum theoretical efficiency. This could be due to non-radiative recombination losses in the material and due to the presence of an indirect bandgap, preventing additional photons from being absorbed.

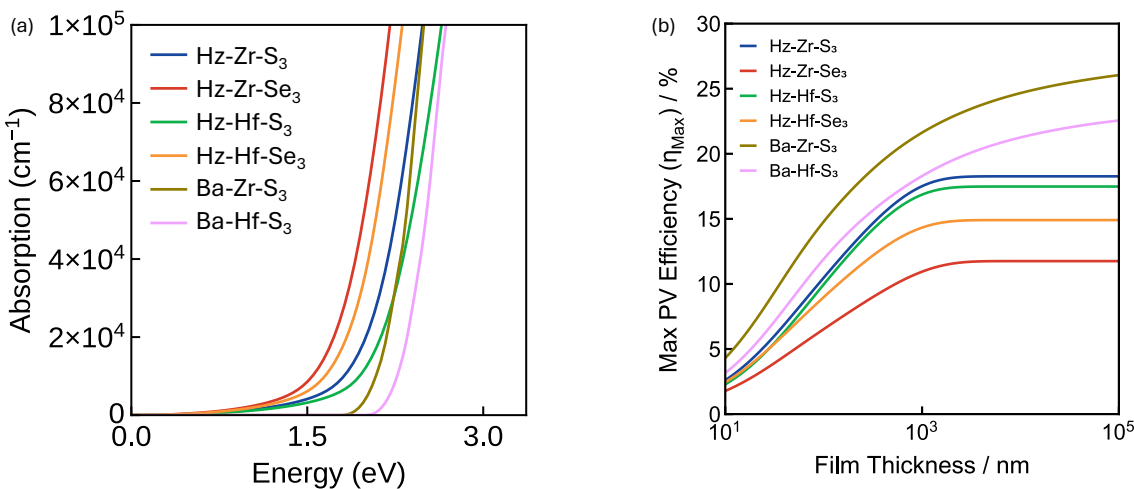


Figure 6.9: (a) HSE06 calculated optical absorption spectra for  $\text{HZ}(\text{Zr}, \text{Hf})(\text{S}, \text{Se})_3$  compounds as a function of energy. (b) SLME for  $\text{HZ}(\text{Zr}, \text{Hf})(\text{S}, \text{Se})_3$  compounds as a function of film thickness, calculated using HSE06.  $\text{BaZrS}_3$  and  $\text{BaHfS}_3$  compounds included as a comparison.

The SLME results show  $\text{HZZrS}_3$  had the highest theoretical efficiency of 18.27%, followed by  $\text{HZHfS}_3$  (17.48%), indicating that S in the X-site performs better than Se for these compounds, irrespective of the B-site. There is a discrepancy in results with the theoretical efficiency of  $\text{HZZrS}_3$  as Sun et al.<sup>3</sup> indicated a maximum efficiency of 29%, much higher than our predicted 18.27%. A likely reason for this would be the omission of the indirect bandgap in their calculations which would lead to a higher

overall performance. This aligns well with our predictions as we calculated a SLME of 29.5% when only a direct bandgap is included.

The high frequency dielectric response,  $\varepsilon_\infty$  and the low frequency response,  $\varepsilon_{\text{ionic}}$ , values along with the total average dielectric constant,  $\varepsilon_0$ , and SLME% were then calculated and are outlined in Table 6.10. The total dielectric constant is the average sum of the high and low frequency responses for each direction.

Table 6.10: Optical properties of HZ based chalcogenide perovskites. Includes high-frequency ( $\varepsilon_\infty$ ) and static ( $\varepsilon_{\text{ionic}}$ ) dielectric responses along the X, Y, and Z directions at 0 eV and the total dielectric constant ( $\varepsilon_0$ ). The corresponding SLME for each compound is also provided.  $\varepsilon_\infty$  calculated using HSE06 and  $\varepsilon_{\text{ionic}}$  calculated using DFPT.

Compound	Dielectric	X	Y	Z	$\varepsilon_0$	SLME%
<chem>HZZrS3</chem>	$\varepsilon_\infty$	7.54	7.13	5.90	83.32	18.27
	$\varepsilon_{\text{ionic}}$	100.87	76.79	51.73		
<chem>HZZrSe3</chem>	$\varepsilon_\infty$	8.69	8.38	6.83	69.77	11.75
	$\varepsilon_{\text{ionic}}$	64.49	79.43	41.49		
<chem>HZHfS3</chem>	$\varepsilon_\infty$	7.20	6.81	5.70	99.68	17.48
	$\varepsilon_{\text{ionic}}$	173.58	55.37	50.39		
<chem>HZHfSe3</chem>	$\varepsilon_\infty$	8.27	7.92	6.63	80.80	14.91
	$\varepsilon_{\text{ionic}}$	89.01	77.22	53.34		

Due to the presence of the HZ within the perovskite structure, there is a reduction in lattice symmetry, resulting in an anisotropic dielectric response. The high-frequency dielectric values for each material range from 5.70–8.69 which is similar to that of  $\varepsilon_\infty^{\text{CdTe}} = 7.1$ ,<sup>290</sup> indicating the ability to polarise under an electric bias and to interact strongly with light, improving absorption. The static dielectric response on the other hand is much greater with a range of values from 41.49–173.58, showing the variation in values based on the orientation and constituent elements. A higher dielectric constant has also been linked to a reduction in electrostatic interactions between charged carriers and charged defects, minimising the effects of defects in these materials.<sup>291,292</sup> Additionally, the high dielectric can be associated with a lower binding energy as outlined in Equation. 1.1 which can enhance charge separation.

## 6.7 *Ab Initio* Molecular Dynamics

Molecular dynamics was completed to explore the dynamical stability for the four HZ compounds over a duration of 10 ps. A  $4 \times 4 \times 4$  supercell containing 768 atoms was used for each simulation. Figure 6.10a-b shows the  $\text{HZZrS}_3$  supercell structure after the simulation while Figure 6.10c is a plot of the temperature and energy per atom as a function of time. The simulation begins at 300 K, followed by a sharp fluctuation in temperature and energy. This is due to the velocities and positions of atoms being in a non-equilibrium state when the simulation begins and is known as the equilibration phase.<sup>293</sup> As the simulation progresses, the energy stabilises around the target temperature. The other three HZ compounds ( $\text{HZZrSe}_3$ ,  $\text{HZHfS}_3$  and  $\text{HZHfSe}_3$ ) also displayed no instability over 10 ps at 300 K. This indicates that the system is in thermal equilibration as the temperature fluctuations are minimal and that the system is running at a consistently with respect to the thermostat settings. Additionally, the kinetic and potential energy are balanced, indicating the compounds are not undergoing any major structural changes and is therefore dynamically stable at room temperature over a time frame of 10 ps.<sup>294</sup>

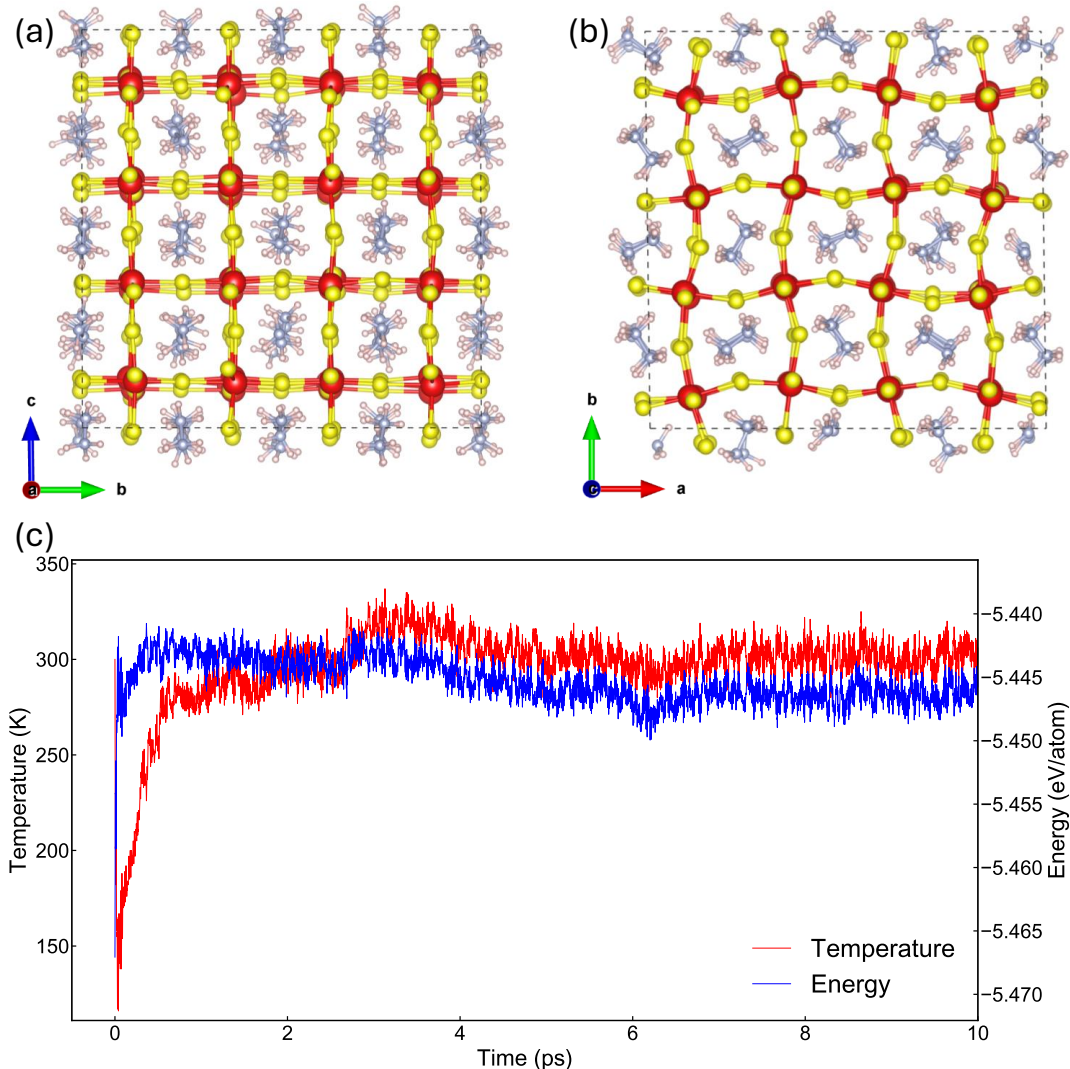


Figure 6.10: HZZrS<sub>3</sub> after 10 ps of AIMD normal to the (a) a-direction and (b) c-direction. (c) Plot of the temperature and energy per atom as a function of time for HZZrS<sub>3</sub>.

## 6.8 Thermodynamic Properties

The thermodynamics properties were calculated for the four HZ compounds. Each compounds formation energy and the thermodynamic stability against competing phases was calculated. The formation energy of each compound can be seen in table 6.11 along with the competing phases for each compound. As all the formation energies are negative, this indicates the compounds were all stable with respect to the elemental phases in their ground state.<sup>277</sup> Furthermore, a negative formation

energy would indicate that it would energetically favourable to form the compounds to form, potentially making them suitable for synthesis under appropriate conditions. The energy above hull was also calculated to be 0.0 eV for all four compounds, meaning each compound was also in its most thermodynamically stable state with respect to the competing phases and therefore lies on the convex hull point.<sup>277</sup> The quaternary convex hull diagram was then calculated for each compound, visualised in Figure 6.11. An energy above hull value of 0.0 eV confirms the compounds are thermodynamically stable and will not decompose into other stable phases further increasing their suitability for synthesis.

Table 6.11: Formation energy and competing phases of HZ containing compounds.

Compound	Formation energy (eV/atom)	Competing phases
HZZrS <sub>3</sub>	-0.56	H <sub>2</sub> , NH, N <sub>2</sub> , Zr, ZrN <sub>2</sub> , S, S <sub>5</sub> N <sub>6</sub>
HZZrSe <sub>3</sub>	-0.48	H <sub>2</sub> , NH, N <sub>2</sub> , Zr, ZrN <sub>2</sub> , Se, SeN
HZHfS <sub>3</sub>	-0.56	H <sub>2</sub> , NH, N <sub>2</sub> , Hf, HfN <sub>2</sub> , S, S <sub>5</sub> N <sub>2</sub> ,
HZHfSe <sub>3</sub>	-0.48	H <sub>2</sub> , NH, N <sub>2</sub> , Hf, HfN <sub>2</sub> , Se, SeN

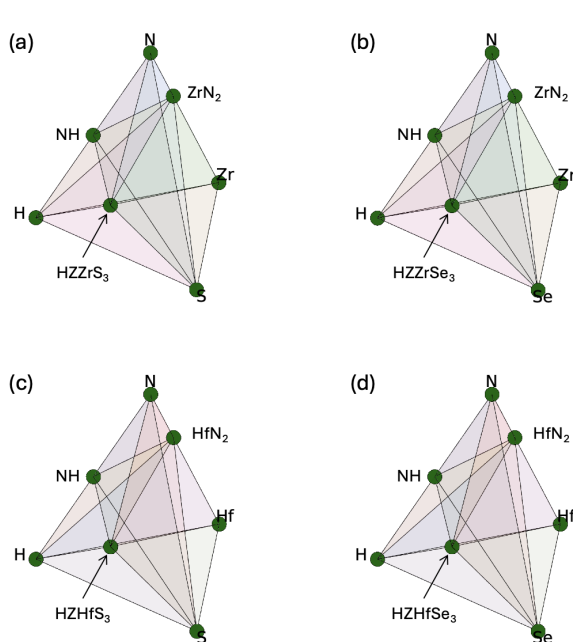


Figure 6.11: Convex hull of each HZ chalcogenide. (a) HZZrS<sub>3</sub>, (b) HZZrSe<sub>3</sub>, (c) HZHfS<sub>3</sub>, (d) HZHfSe<sub>3</sub>

## 6.9 Band Alignments

As these HZ compounds have not been reported in detail before, the band alignments are useful to calculate as they can provide a prediction on suitable contact materials. In this sense, it is possible to predict suitable device architectures for these materials for future work. For all four compounds the (010) plane had the lowest surface energy. The PlanarAverage<sup>295</sup> code was then utilised to calculate the average electrostatic potential in the vacuum and obtain the vacuum slab energy value. Band structure calculations were then completed to obtain the core state eigenenergies, the VBM and the bandgap to calculate the IP and EA which can be seen in Figure 6.12. Immediately it is noticeable that sulphide perovskites have deep ionisation potentials than the selenides due to the smaller atomic radii of sulphur and higher electronegativity. The Hf compounds also display slightly deeper ionisation potentials compared to the Zr ones, although not as drastically. HZHfS<sub>3</sub> has comparable ionisation potentials to other common solar absorbers such as MAPbI<sub>3</sub><sup>296</sup> (IP=5.70) and CdTe<sup>297</sup> (IP=5.69), whereas the other three compounds have ionisation potentials more than 1 eV higher. For HZZrS<sub>3</sub> a suitable HTL would be P3HT,<sup>298</sup> resulting an offset of only 0.05 eV, forming a low barrier for hole transport. An ETL of SnO<sub>2</sub> would be suitable as is well aligned with the CB. As HZHfS<sub>3</sub> has a deeper IP and EA, F8<sup>299</sup> has a better suited workfunction as the HTL while an ITO<sup>300</sup> would be a suitable contact material. However, challenges arise with the selenide compounds as they have have relatively shallow EA and IP which can hinder their charge extraction properties. Furthermore, there are very few suitable contact materials for these compounds, which could limit their suitability in PV devices.

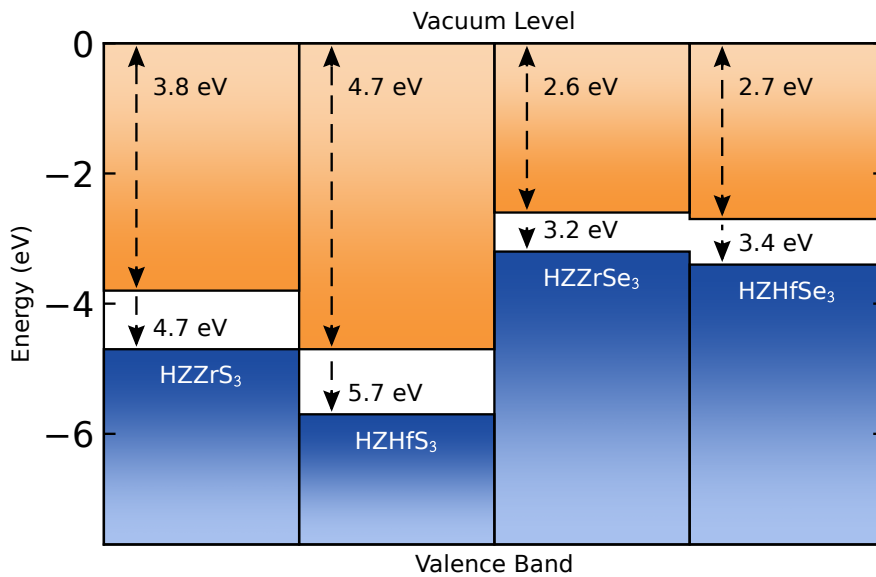


Figure 6.12: Band alignments for each HZ compound.

6

## 6.10 HZ(Zr, Hf)(S, Se)<sub>3</sub> Trends

### 6.10.1 Chemical Composition Analysis

To further understand the origins of the properties seen in the previous sections, it is essential to understand how the chemical structure of HZ chalcogenides impacts the electronic and optical properties. To understand the effect of different chemical structures on the electronic properties, the direct bandgaps and indirect bandgaps are plotted in Figure 6.13. From this figure, both the direct and indirect bandgap decrease from HZHfS<sub>3</sub> → HZZrS<sub>3</sub> → HZHfSe<sub>3</sub> → HZZrSe<sub>3</sub>. The direct bandgap reduces from 1.85 eV to 1.38 eV while the indirect bandgaps also decreases from 1.36 eV to 0.70 eV. This can be a result of a greater overlap between the transition metal (Zr, Hf) *d*-orbitals and chalcogenide *p*-orbitals, resulting in broader bands and therefore a smaller bandgap. It can also be seen that the energy difference between the direct bandgap and indirect bandgap ( $\Delta E_g^{\text{dir-indir}}$ ) increases when exchanging Hf for Zr and also when exchanging S for Se, resulting in an energy difference of

0.49 eV to 0.68 eV. The SLME is generally reduced as the difference in energy between direct and indirect bandgap increases, however the bandgap also plays a role in the SLME. For example, HZHfS<sub>3</sub> has a lower  $\Delta E_g^{\text{dir-indir}}$  than HZZrS<sub>3</sub> but has a slightly lower efficiency of 17.48 % compared to 18.27 %. This being due to HZHfS<sub>3</sub> having a less optimal direct bandgap of 1.85 eV in comparison to 1.68 eV. Additionally, the dielectric constant decreases as  $\Delta E_g^{\text{dir-indir}}$  increases, suggesting decreased polarizability in selenide compounds.

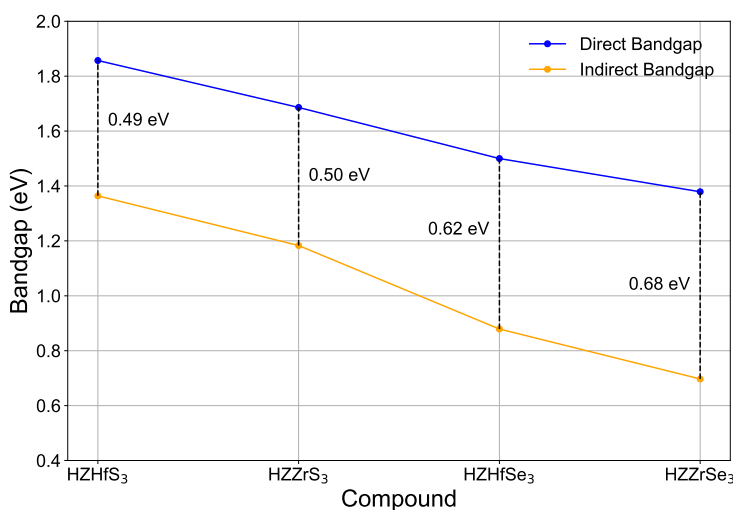


Figure 6.13: Direct and indirect bandgaps plotted for HZ perovskites.

The effect of exchanging the S to Se results in the effective masses dramatically improving in the Hf compounds. This effect is also seen in the Zr containing compounds but not as notably. This is likely due to the change in size and electronegativity between S and Se. The increased ionic radius results in increased lattice parameters, resulting in a more delocalised electronic states and lower effective masses. This is further exemplified by the lower electronegativity of Se, causing a weaker bonding character and greater orbital overlapping in Se compounds. The weaker bonding character results in a reduction in energy between bonding and anti-bonding sites and thus lowers the bandgap of Se based compounds. Lower bandgaps can also result in broader electronic bands with a greater curvature near the band

edges. The electron effective mass of HZHfS<sub>3</sub> is seen to be much higher than the rest of the results with a value of 0.74. This is a result of the CBM in Figure 6.7f exhibiting a significantly lower dispersion at the  $\Gamma$ -point compared to the other band structures. Consequently, the carriers near the CBM experience reduced mobility, leading to this higher effective mass. For the remainder of compounds, the electron and hole masses are lower in Hf compounds compared to Zr ones, visualised in Figure 6.14. The chemical composition also has effects on the optical properties of the HZ compounds. In Figure 6.9a there is a red-shift in absorption onset which is correlated to the bandgaps of each material. Similarly, in the case of exchanging Hf for Zr, which has a slightly larger ionic radii, the direct and indirect bandgap also decreases.

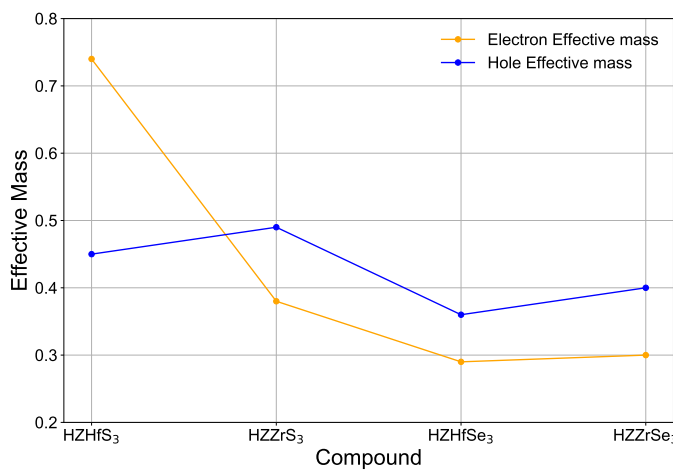


Figure 6.14: Comparison of changes in electron and hole effective masses in hydrazinium compounds. Effective mass is in units of electron rest mass.

### 6.10.2 Charge Density Analysis

In this section we attempt to understand the underlying reasons for the formation of an indirect bandgap in all the HZ compounds. This will be done through comparing the partial charge density isosurfaces of BaZrS<sub>3</sub> with HZZrS<sub>3</sub>. BaZrS<sub>3</sub> is used as a comparison as it possesses only a direct bandgap, while HZZrS<sub>3</sub> is chosen as

it has the most promising optoelectronic properties and has the same B and X-site elements and BaZrS<sub>3</sub>, which is important as the BX octahedra determines the electronic properties. The band structure along with the respective isosurfaces for HZZrS<sub>3</sub> and BaZrS<sub>3</sub> can be seen in Figure 6.15.

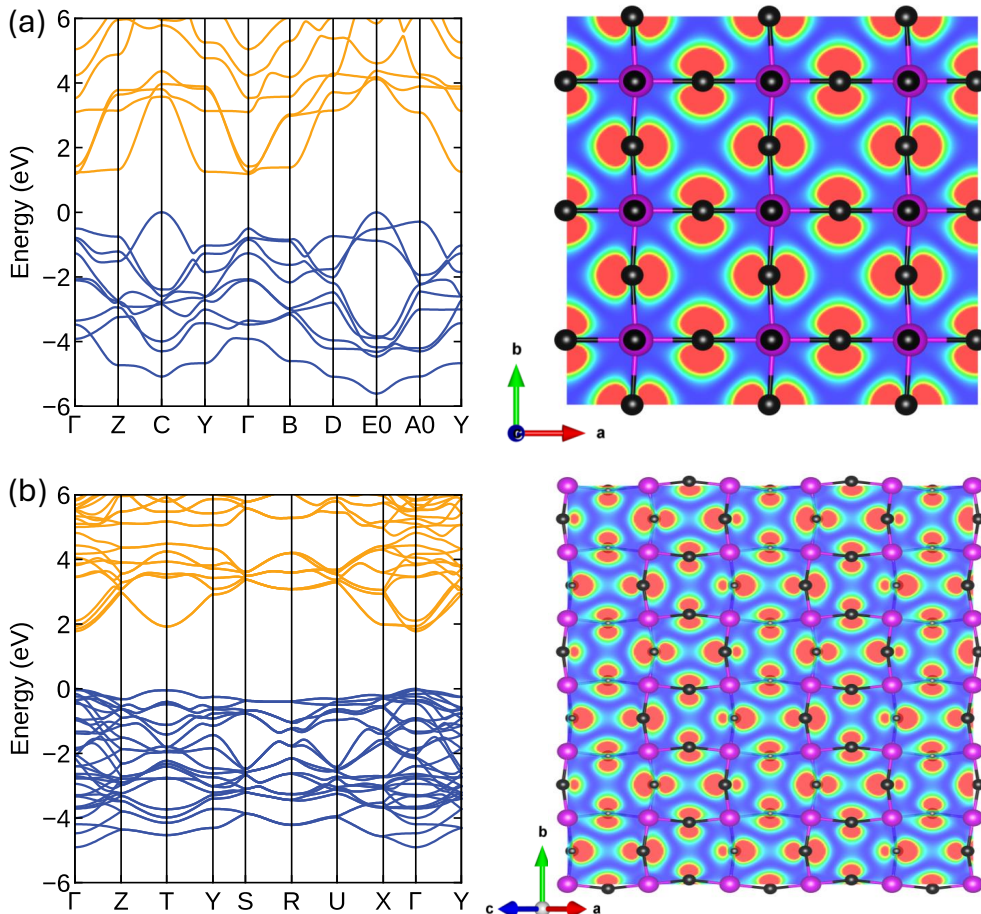


Figure 6.15: Band structure and partial charge density isosurface of (a) the VBM C-point of HZZrS<sub>3</sub> and (b) the VBM T-point BaZrS<sub>3</sub>. Zirconium atoms are in purple and sulphur are in black. The isosurface level is set to 2 meV/Å. Barium and hydrazinium have been excluded for image clarity.

In HZZrS<sub>3</sub> the indirect bandgap is located at the C-point. The corresponding partial charge density isosurface reveals a uniform and symmetric charge distribution around each sulphur atom in the (001) plane. This distribution results in a strong anti-bonding character which increases the energy at the C-point, shifting the VBM

upwards, contributing to the formation of an indirect bandgap. In contrast, when examining the T-point in BaZrS<sub>3</sub> which is comparable to the C-point in HZZrS<sub>3</sub>, it can be seen that the T-point is much less dispersive and at a lower energy than the  $\Gamma$ -point, indicating a direct bandgap. This difference can be attributed to the weak anti-bonding character in the (101) plane of BaZrS<sub>3</sub>, visualised by the asymmetric charge densities isosurfaces. This weaker anti-bonding character resulting in a more in-phase orbital overlap, lowering the energy and suppressing the T-point, causing the VBM to be located at the  $\Gamma$ -point.



# Conclusions and Further Work

In this thesis, computational methods were employed to aid the discovery of hybrid chalcogenide perovskites as an alternative to lead halide perovskites for photovoltaic application. Our approach involved screening 21 unique organic molecules to be incorporated into the A-site of the chalcogenide perovskite structure for further analysis using DFT. Through this material screening and DFT analysis, we have identified four promising hydrazinium chalcogenide perovskites with potential for photovoltaic application. This was achieved by obtaining the ground state energies for each material, followed by performing optoelectronic property calculations. To evaluate the stability of these compounds, dynamic and thermodynamic stability calculations were performed, revealing all four compounds were dynamically and thermodynamically stable. Additionally, band alignment calculations were completed to find suitable contact materials which showed that sulphur containing compounds would be more suited for full stack devices in comparison to those containing selenium. Through this workflow, we have found that hybrid chalcogenide perovskites are exceedingly rare due to the requirement of a small A-site cation. We have also found that an A-site cation effective greater than 220 pm, results in a highly distorted lattice resulting in bonds breaking and non-perovskite phases forming. Furthermore, we have found that monovalent cations are not well suited with pentavalent B-site cations such as Bi and Sb as any stable structures produced poor optoelectronic properties as a result of narrow bandgaps with some structures also displaying metallic behaviour. It was found divalent cations produced superior optoelectronic properties with bandgaps in the four  $\text{HZBX}_3$  where B= Zr, Hf and X= S, Se ranging from 1.38–1.85 eV and desirable effective masses less than

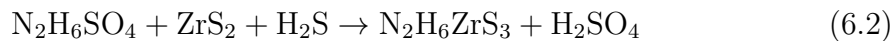
$m_0$ . Unfortunately, these compound were limited by an indirect bandgap forming at the C-point due to high symmetry regions in the (001) plane. This resulted in a reduction in maximum theoretical efficiencies which ranged from 11.75–18.27 %. Despite this reduced theoretical efficiencies, the four compounds displayed impressive absorption coefficients, rising to above  $10^5\text{cm}^{-1}$  within 0.5 eV of absorption onset.

Having shown theoretically that  $\text{HZBX}_3$  ( $\text{B} = \text{Zr, Hf}$ ;  $\text{X} = \text{S, Se}$ ) is thermodynamically and dynamically stable and produces a direct bandgap and desirable optoelectric properties with absorption coefficients  $> 10^5\text{cm}^{-1}$ , this family of hybrid chalcogenide compounds has merit to be a effective solar absorber. Currently, the largest drawback is the formation of an indirect bandgap at the C-point within the VBM. Further work must be carried out in understanding the origin this indirect bandgap and methods to shift the VBM to restore the direct bandgap to the  $\Gamma$ -point. This may be possible through bandgap tuning by introducing transition metals such as Ti into the B-site as done by Wei et al.<sup>151</sup> to form  $\text{HZZr}_{1-x}\text{Ti}_x\text{S}_3$  in an effort to narrow the bandgap at the  $\Gamma$ -point and produce a direct bandgap. Another route is by having a mixed A-site of HZ and Ba to improve suppress the primary VB pocket at the C-point. A potential mechanical solution that has been successful in  $\text{AZrS}_3$  where  $\text{A} = \text{Mg, Ca, Sr}$  and Ba was through strain induced bandgap tuning by applying hydrostatic pressure to reduce the direct bandgap to a more suitable energy level.<sup>301</sup> This method could also induce octahedral tilting, reducing the anti-bonding nature seen in the HZ compounds to form a direct bandgap at the  $\Gamma$ -point. It is also important to note, this report focuses solely on structures in their cubic phase and without any defects. By only examining a single phase it may be possible that the compound is not in its true ground state as mentioned in section 2.3 and therefore in further works it would be advantageous to calculate the ground state energies over multiple phases. A similar situation can occur through the omission of defect calculations as the compounds could potentially relax to local metastable configuration, possibly leading to inaccuracies in further calculations.<sup>302,303</sup> Defect

studies utilising the Doped<sup>278</sup> defect package and ShakeNBreak<sup>304</sup> package can be used to carry out these defect calculations and also to understand the nature of defects in these materials. It will be particularly important understand the defect chemistry of these compounds and the role of active traps and the associated non-recombination rates. Although these compounds have only recently been realised, further research is unwarranted if they prove challenging to synthesise. Therefore, a proposed synthesis method for H<sub>2</sub>H<sub>6</sub>SO<sub>4</sub> (HZSO<sub>4</sub>) by Klapötke et al.<sup>305</sup> is outlined below in Equation. 6.1 where hydrazinium azide ([N<sub>2</sub>H<sub>5</sub>][N<sub>3</sub>]) and sulphuric acid (H<sub>2</sub>SO<sub>4</sub>) are reacted in an aqueous solution to form N<sub>2</sub>H<sub>6</sub>SO<sub>4</sub>.<sup>305</sup>



Hydrazinium sulphate exists as a salt<sup>305</sup> and therefore would be most suited for a solid state powder reaction in the form:



This reaction is analogous to the sulphurization synthesis reaction outlined in section 2.5 and could provide a suitable pathway to synthesising HZZrS<sub>3</sub> in the future. Ultimately, this thesis provides a foundation for hybrid chalcogenide perovskites for photovoltaic applications, by displaying their theoretical properties and offering an Earth abundant and eco-friendly alternative to lead halide perovskites.



# Bibliography

- [1] Christopher N. Savory A Theoretical Exploration of Emerging Solar Absorber Materials. Ph.D. thesis, UCL.
- [2] Chen, B.; Yang, M.; Priya, S.; Zhu, K. *The Journal of Physical Chemistry Letters* **2016**, *7*, 905–917, DOI: 10.1021/acs.jpcllett.6b00215.
- [3] Sun, Y.-Y.; Agiorgousis, M. L.; Zhang, P.; Zhang, S. *Nano Letters* **2015**, *15*, 581–585, DOI: 10.1021/nl504046x.
- [4] JJ Acton *Literature review: Computational Discover of Hybrid Chalcogenide Perovskite Photovoltaics*; 2023.
- [5] Ju, M.-G.; Dai, J.; Ma, L.; Zeng, X. C. *Advanced Energy Materials* **2017**, *7*, 1700216, DOI: 10.1002/aenm.201700216, \_eprint: <https://onlinelibrary.wiley.com/doi/pdf/10.1002/aenm.201700216>.
- [6] Huo, Z.; Wei, S.-H.; Yin, W.-J. *Journal of Physics D: Applied Physics* **2018**, *51*, 474003, DOI: 10.1088/1361-6463/aae1ee.
- [7] Park, H.; Mall, R.; Alharbi, F. H.; Sanvito, S.; Tabet, N.; Bensmail, H.; El-Mellouhi, F. *The Journal of Physical Chemistry A* **2019**, *123*, 7323–7334, DOI: 10.1021/acs.jpca.9b06208, Publisher: American Chemical Society.
- [8] Gupta, T. et al. *Advanced Functional Materials* **2020**, *30*, 2001387, DOI: 10.1002/adfm.202001387.
- [9] Niu, S.; Milam-Guerrero, J.; Zhou, Y.; Ye, K.; Zhao, B.; Melot, B. C.; Ravichandran, J. *Journal of Materials Research* **2018**, *33*, 4135–4143, DOI: 10.1557/jmr.2018.419.

- [10] Haynes, W. M., Lide, D. R., Bruno, T. J., Eds. *CRC Handbook of Chemistry and Physics*, 97th ed.; CRC Press, 2016; DOI: 10.1201/9781315380476.
- [11] Yuan, Z.; Dahliah, D.; Claes, R.; Pike, A.; Fenning, D. P.; Rignanese, G.-M.; Hautier, G. Assessing carrier mobility, dopability, and defect tolerance in the chalcogenide perovskite BaZrS<sub>3</sub>. 2024; <http://arxiv.org/abs/2405.09793>, arXiv:2405.09793 [cond-mat].
- [12] Alex Ganose Tailoring the band gap of SnO<sub>2</sub> for improved transparent electronic conducting properties in solar cells. Ph.D. thesis, UCL.
- 6
- [13] Raj, R.; Singh, R.; Guin, M. *ChemistrySelect* **2023**, *8*, e202303550, DOI: 10.1002/slct.202303550, eprint: <https://onlinelibrary.wiley.com/doi/pdf/10.1002/slct.202303550>.
- [14] Sopiha, K. V.; Comparotto, C.; Márquez, J. A.; Scragg, J. J. S. *Advanced Optical Materials* **2022**, *10*, 2101704, DOI: 10.1002/adom.202101704.
- [15] Buffiere, M.; Dhawale, D. S.; El-Mellouhi, F. *Energy Technology* **2019**, *7*, 1900819, DOI: 10.1002/ente.201900819.
- [16] Nishigaki, Y.; Nagai, T.; Nishiwaki, M.; Aizawa, T.; Kozawa, M.; Hanzawa, K.; Kato, Y.; Sai, H.; Hiramatsu, H.; Hosono, H.; Fujiwara, H. *Solar RRL* **2020**, *4*, 1900555, DOI: 10.1002/solr.201900555.
- [17] Kim, S.; Chen, J.; Cheng, T.; Gindulyte, A.; He, J.; He, S.; Li, Q.; Shoemaker, B. A.; Thiessen, P. A.; Yu, B.; Zaslavsky, L.; Zhang, J.; Bolton, E. E. *Nucleic Acids Research* **2023**, *51*, D1373–D1380, DOI: 10.1093/nar/gkac956.
- [18] Alam, M. M.; Aktar, M. A.; Idris, N. D. M.; Al-Amin, A. Q. *World Development Sustainability* **2023**, *2*, 100048, DOI: 10.1016/j.wds.2023.100048.

- [19] Peter, L. M. *Philosophical Transactions of the Royal Society A: Mathematical, Physical and Engineering Sciences* **2011**, *369*, 1840–1856, DOI: 10.1098/rsta.2010.0348.
- [20] Tumala, M. M.; Salisu, A.; Nmadu, Y. B. *Energy Economics* **2023**, *124*, 106792, DOI: 10.1016/j.eneco.2023.106792.
- [21] Credence Research Solar Photovoltaic (PV) Market Size, Growth & Forecast 2032. 2024; <https://www.credenceresearch.com/report/solar-photovoltaic-pv-market>.
- [22] Torrence, C. E.; Libby, C. S.; Nie, W.; Stein, J. S. *iScience* **2023**, *26*, 105807, DOI: 10.1016/j.isci.2022.105807.
- [23] Fthenakis, V. M.; Bulawka, A. O. *Encyclopedia of Energy*; Elsevier, 2004; pp 61–69, DOI: 10.1016/B0-12-176480-X/00421-6.
- [24] Gielen, D.; Boshell, F.; Saygin, D.; Bazilian, M. D.; Wagner, N.; Gorini, R. *Energy Strategy Reviews* **2019**, *24*, 38–50, DOI: 10.1016/j.esr.2019.01.006.
- [25] Hersch, P.; Zweibel, K. *Basic photovoltaic principles and methods*; 1982; pp SERI/SP-290-1448, 5191389, DOI: 10.2172/5191389.
- [26] Goetzberger, A.; Hebling, C.; Schock, H.-W. *Materials Science and Engineering: R: Reports* **2003**, *40*, 1–46, DOI: 10.1016/S0927-796X(02)00092-X.
- [27] Al-Ezzi, A. S.; Ansari, M. N. M. *Applied System Innovation* **2022**, *5*, 67, DOI: 10.3390/asi5040067.
- [28] Nelson, J.; Kwiatkowski, J. J.; Kirkpatrick, J.; Frost, J. M. *Accounts of Chemical Research* **2009**, *42*, 1768–1778, DOI: 10.1021/ar900119f, Publisher: American Chemical Society.
- [29] Zanatta, A. R. *Results in Optics* **2022**, *9*, 100320, DOI: 10.1016/j.rio.2022.100320.

- [30] Shah, A.; Torres, P.; Tscharner, R.; Wyrsch, N.; Keppner, H. *Science* **1999**, *285*, 692–698, DOI: 10.1126/science.285.5428.692.
- [31] Sze, S. M.; Ng, K. K. *Physics of semiconductor devices*, 3rd ed.; Wiley-Interscience: Hoboken, N.J, 2007.
- [32] Gray, J. L. *Handbook of Photovoltaic Science and Engineering*; John Wiley & Sons, Ltd, 2010; pp 82–129, DOI: 10.1002/9780470974704.ch3, Section: 3 \_eprint: <https://onlinelibrary.wiley.com/doi/pdf/10.1002/9780470974704.ch3>.
- [33] Kangsabanik, J.; Svendsen, M. K.; Taghizadeh, A.; Crovetto, A.; Thygesen, K. S. *Journal of the American Chemical Society* **2022**, *144*, 19872–19883, DOI: 10.1021/jacs.2c07567, Publisher: American Chemical Society.
- [34] Htike, T.; Tun, H. M. **2020**, DOI: 10.5281/ZENODO.3616407, Publisher: Al-borear (OPC) Pvt. Ltd. Version Number: Original.
- [35] Nelson, J. *The Physics of Solar Cells*; PUBLISHED BY IMPERIAL COLLEGE PRESS AND DISTRIBUTED BY WORLD SCIENTIFIC PUBLISHING CO., 2003; DOI: 10.1142/p276.
- [36] Sadhukhan, S.; Acharya, S.; Panda, T.; Mandal, N. C.; Bose, S.; Nandi, A.; Das, G.; Maity, S.; Chakraborty, S.; Chaudhuri, P.; Saha, H. *Sustainable Developments by Artificial Intelligence and Machine Learning for Renewable Energies*; Elsevier, 2022; pp 63–129, DOI: 10.1016/B978-0-323-91228-0.00007-0.
- [37] Sharaf, O. Z.; Orhan, M. F. *Renewable and Sustainable Energy Reviews* **2015**, *50*, 1500–1565, DOI: 10.1016/j.rser.2015.05.036.
- [38] Kumar, S. G.; Rao, K. S. R. K. *Energy Environ. Sci.* **2014**, *7*, 45–102, DOI: 10.1039/C3EE41981A.

- [39] Yoon, J.; Sun, Y.; Rogers, J. A. *Semiconductor Nanomaterials for Flexible Technologies*; Elsevier, 2010; pp 159–196, DOI: 10.1016/B978-1-4377-7823-6.00006-4.
- [40] Qian, X. *Journal of Physics: Conference Series* **2021**, *2044*, 012042, DOI: 10.1088/1742-6596/2044/1/012042.
- [41] Singh, R.; Parashar, M. **2020**, DOI: 10.1063/9780735422414\_001.
- [42] Lindholm, F.; Fossum, J.; Burgess, E. *IEEE Transactions on Electron Devices* **1979**, *26*, 165–171, DOI: 10.1109/T-ED.1979.19400, Conference Name: IEEE Transactions on Electron Devices.
- [43] Augusto, A.; Herasimenka, S. Y.; King, R. R.; Bowden, S. G.; Honsberg, C. *Journal of Applied Physics* **2017**, *121*, 205704, DOI: 10.1063/1.4984071.
- [44] Baruch, P.; De Vos, A.; Landsberg, P.; Parrott, J. *Solar Energy Materials and Solar Cells* **1995**, *36*, 201–222, DOI: 10.1016/0927-0248(95)80004-2.
- [45] Sinton, R. A.; Cuevas, A. *Applied Physics Letters* **1996**, *69*, 2510–2512, DOI: 10.1063/1.117723.
- [46] Green, M. A. *Solid-State Electronics* **1981**, *24*, 788–789, DOI: 10.1016/0038-1101(81)90062-9.
- [47] Jain, A.; Kapoor, A. *Solar Energy Materials and Solar Cells* **2004**, *81*, 269–277, DOI: 10.1016/j.solmat.2003.11.018.
- [48] Shockley, W.; Queisser, H. J. *Journal of Applied Physics* **1961**, *32*, 510–519, DOI: 10.1063/1.1736034.
- [49] Chapin, D. M.; Fuller, C. S.; Pearson, G. L. *Journal of Applied Physics* **1954**, *25*, 676–677, DOI: 10.1063/1.1721711.

- [50] Musselman, K. P.; Poorkazem, K. *Advanced Micro- and Nanomaterials for Photovoltaics*; Elsevier, 2019; pp 1–17, DOI: 10.1016/B978-0-12-814501-2.00001-3.
- [51] Fraunhofer Institute for Solar Energy Systems, ISE; with the support of PSE Projects GmbH Photovoltaics Report. 2024; <https://www.ise.fraunhofer.de/en.html>.
- [52] Pastuszak, J.; Wgierek, P. *Materials* **2022**, *15*, 5542, DOI: 10.3390/ma15165542, Number: 16 Publisher: Multidisciplinary Digital Publishing Institute.
- 6
- [53] Rajendran, S.; Naushad, M.; Raju, K.; Boukherroub, R. *Emerging nanostructured materials for energy and environmental science*; Springer International Publishing, 2019; Accepted: 2020-08-21T09:40:09Z ISSN: 978-3-030-04474-9.
- [54] Carlson, D. E.; Wronski, C. R. *Applied Physics Letters* **1976**, *28*, 671–673, DOI: 10.1063/1.88617.
- [55] Kim, S.; Chung, J.-W.; Lee, H.; Park, J.; Heo, Y.; Lee, H.-M. *Solar Energy Materials and Solar Cells* **2013**, *119*, 26–35, DOI: 10.1016/j.solmat.2013.04.016.
- [56] Ong, Y. Y.; Chen, B. T.; Tay, F. E. H.; Iliescu, C. *Journal of Physics: Conference Series* **2006**, *34*, 812–817, DOI: 10.1088/1742-6596/34/1/134.
- [57] Freysoldt, C.; Pfanner, G.; Neugebauer, J. *Journal of Non-Crystalline Solids* **2012**, *358*, 2063–2066, DOI: 10.1016/j.jnoncrysol.2011.12.090.
- [58] Lee, S. H.; Bhopal, M. F.; Lee, D. W.; Lee, S. H. *Materials Science in Semiconductor Processing* **2018**, *79*, 66–73, DOI: 10.1016/j.msssp.2018.01.019.
- [59] Stutzmann, M.; Jackson, W. B.; Tsai, C. C. *Physical Review B* **1985**, *32*, 23–47, DOI: 10.1103/PhysRevB.32.23.

- [60] Lee, T.; Ebong, A. *Renewable and Sustainable Energy Reviews* **2017**, *70*, 1286–1297, DOI: 10.1016/j.rser.2016.12.028.
- [61] Dixon, A. *Solar Energy Conversion II*; Elsevier, 1981; pp 243–259, DOI: 10.1016/B978-0-08-025388-6.50037-4.
- [62] Hahn, H.; Mutschke, U. *Zeitschrift für anorganische und allgemeine Chemie* **1957**, *288*, 269–278, DOI: 10.1002/zaac.19572880505.
- [63] Kazmerski, L. L.; White, F. R.; Morgan, G. K. *Applied Physics Letters* **1976**, *29*, 268–270, DOI: 10.1063/1.89041.
- [64] Ramanujam, J.; Singh, U. P. *Energy & Environmental Science* **2017**, *10*, 1306–1319, DOI: 10.1039/C7EE00826K, Publisher: The Royal Society of Chemistry.
- [65] Interactive Best Research-Cell Efficiency Chart. <https://www.nrel.gov/pv/interactive-cell-efficiency.html>.
- [66] Salhi, B. *Materials* **2022**, *15*, 1908, DOI: 10.3390/ma15051908.
- [67] Bonnet, D.; Rabenhorst, H. New results on the development of a thin-film p-CdTe-n-CdS heterojunction solar cell. Photovoltaic specialists conference, 9 th, silver spring, md. 1972; pp 129–132.
- [68] Meng, W.; Jinqing, P.; Hongxing, Y.; Yimo, L. *Energy Procedia* **2018**, *152*, 1091–1096, DOI: 10.1016/j.egypro.2018.09.131.
- [69] Bibin John; Varadharajaperumal, S. *Physics of Metals and Metallography* **2023**, *124*, 1795–1812, DOI: 10.1134/S0031918X2110094X.
- [70] Agrinskaya, N.; Arkadeva, E. *Nuclear Instruments and Methods in Physics Research Section A: Accelerators, Spectrometers, Detectors and Associated Equipment* **1989**, *283*, 260–262, DOI: 10.1016/0168-9002(89)91367-3.

- [71] K. Rao, M.; Sangeetha, D.; Selvakumar, M.; Sudhakar, Y.; Mahesha, M. *Solar Energy* **2021**, *218*, 469–491, DOI: 10.1016/j.solener.2021.03.005.
- [72] Goetz, K. P.; Vaynzof, Y. *ACS Energy Letters* **2022**, *7*, 1750–1757, DOI: 10.1021/acsenergylett.2c00463.
- [73] Schulz, P.; Cahen, D.; Kahn, A. Halide perovskites: Is it all about the interfaces? 2018; <https://arxiv.org/abs/1812.04908>, Version Number: 1.
- [74] Almora, O. et al. *Advanced Energy Materials* **2024**, *14*, 2303173, DOI: 10.1002/aenm.202303173.
- [75] O'Regan, B.; Grätzel, M. *Nature* **1991**, *353*, 737–740, DOI: 10.1038/353737a0, Publisher: Nature Publishing Group.
- [76] Soga, T. *Nanostructured Materials for Solar Energy Conversion*; Elsevier, 2006; pp vii–ix, DOI: 10.1016/B978-044452844-5/50001-9.
- [77] Grätzel, M. *Journal of Photochemistry and Photobiology C: Photochemistry Reviews* **2003**, *4*, 145–153, DOI: 10.1016/S1389-5567(03)00026-1.
- [78] Gong, J.; Sumathy, K.; Qiao, Q.; Zhou, Z. *Renewable and Sustainable Energy Reviews* **2017**, *68*, 234–246, DOI: 10.1016/j.rser.2016.09.097.
- [79] Grätzel, M. *Inorganic Chemistry* **2005**, *44*, 6841–6851, DOI: 10.1021/ic0508371, Publisher: American Chemical Society.
- [80] Hagfeldt, A.; Boschloo, G.; Sun, L.; Kloo, L.; Pettersson, H. *Chemical Reviews* **2010**, *110*, 6595–6663, DOI: 10.1021/cr900356p, Publisher: American Chemical Society.
- [81] Polman, A.; Knight, M.; Garnett, E.; Ehrler, B.; Sinke, W. *Science* **2016**, *352*, aad4424–aad4424, DOI: 10.1126/science.aad4424.

- [82] Maalouf, A.; Okoroafor, T.; Jehl, Z.; Babu, V.; Resalati, S. *Renewable and Sustainable Energy Reviews* **2023**, *186*, 113652, DOI: 10.1016/j.rser.2023.113652.
- [83] A. Pochettino; A. Sella *Photoelectric behavior of anthracene*; Acad. Lincei Rend., 1906; Vol. 15; pp 355–363.
- [84] Clarke, T. M.; Durrant, J. R. *Chemical Reviews* **2010**, *110*, 6736–6767, DOI: 10.1021/cr900271s, Publisher: American Chemical Society.
- [85] Förster, T. *Annalen der Physik* **1948**, *437*, 55–75, DOI: 10.1002/andp.19484370105.
- [86] Oku, T. *Nanomaterials for Solar Cell Applications*; Elsevier, 2019; pp 661–698, DOI: 10.1016/B978-0-12-813337-8.00017-5.
- [87] Riley, D. B.; Meredith, P.; Armin, A.; Sandberg, O. J. *The Journal of Physical Chemistry Letters* **2022**, *13*, 4402–4409, DOI: 10.1021/acs.jpcllett.2c00791.
- [88] Marcus, R. A. *The Journal of Chemical Physics* **1984**, *81*, 4494–4500, DOI: 10.1063/1.447418.
- [89] Frost, J. M.; Faist, M. A.; Nelson, J. *Advanced Materials* **2010**, *22*, 4881–4884, DOI: 10.1002/adma.201002189.
- [90] Zhu, L. et al. *Nature Materials* **2022**, *21*, 656–663, DOI: 10.1038/s41563-022-01244-y, Publisher: Nature Publishing Group.
- [91] Wadsworth, A.; Hamid, Z.; Kosco, J.; Gasparini, N.; McCulloch, I. *Advanced Materials* **2020**, *32*, 2001763, DOI: 10.1002/adma.202001763, \_eprint: <https://onlinelibrary.wiley.com/doi/pdf/10.1002/adma.202001763>.
- [92] Holliday, S. et al. *Nature Communications* **2016**, *7*, 11585, DOI: 10.1038/ncomms11585.

- [93] Lin, Y.; He, Q.; Zhao, F.; Huo, L.; Mai, J.; Lu, X.; Su, C.-J.; Li, T.; Wang, J.; Zhu, J.; Sun, Y.; Wang, C.; Zhan, X. *Journal of the American Chemical Society* **2016**, *138*, 2973–2976, DOI: 10.1021/jacs.6b00853.
- [94] Gasparini, N.; Paletti, S. H. K.; Bertrandie, J.; Cai, G.; Zhang, G.; Wadsworth, A.; Lu, X.; Yip, H.-L.; McCulloch, I.; Baran, D. *ACS Energy Letters* **2020**, *5*, 1371–1379, DOI: 10.1021/acsenergylett.0c00604.
- [95] Goldschmidt, V. M. *Die Naturwissenschaften* **1926**, *14*, 477–485, DOI: 10.1007/BF01507527.
- [96] Li, Z.; Yang, M.; Park, J.-S.; Wei, S.-H.; Berry, J. J.; Zhu, K. *Chemistry of Materials* **2016**, *28*, 284–292, DOI: 10.1021/acs.chemmater.5b04107.
- [97] A. Hancock, C.; M. Porras-Vazquez, J.; J. Keenan, P.; R. Slater, P. *Dalton Transactions* **2015**, *44*, 10559–10569, DOI: 10.1039/C4DT03036B, Publisher: Royal Society of Chemistry.
- [98] Pisoni, A.; Jaimovi, J.; Barii, O. S.; Spina, M.; Gaál, R.; Forró, L.; Horváth, E. *The Journal of Physical Chemistry Letters* **2014**, *5*, 2488–2492, DOI: 10.1021/jz5012109, Publisher: American Chemical Society.
- [99] Hu, S.; Ren, Z.; Djurii, A. B.; Rogach, A. L. *ACS Energy Letters* **2021**, *6*, 3882–3905, DOI: 10.1021/acsenergylett.1c02015.
- [100] Duan, T.; Zha, J.; Lin, N.; Wang, Z.; Tan, C.; Zhou, Y. *Device* **2023**, *1*, 100221, DOI: 10.1016/j.device.2023.100221.
- [101] Kong, L. et al. *Nature* **2024**, *631*, 73–79, DOI: 10.1038/s41586-024-07531-9.
- [102] Frost, J. M.; Butler, K. T.; Brivio, F.; Hendon, C. H.; van Schilfgaarde, M.; Walsh, A. *Nano Letters* **2014**, *14*, 2584–2590, DOI: 10.1021/nl500390f, Publisher: American Chemical Society.

- [103] Giovanni, D. Optical-spin dynamics in organic-inorganic lead halide perovskites. Ph.D. thesis, 2017.
- [104] Jeon, N.; Noh, J.; Yang, W.; Kim, Y.; Ryu, S.; Seo, J.; Seok, S. *Nature* **2015**, *517*, 476–480, DOI: 10.1038/nature14133.
- [105] Mitzi, D. B.; Feild, C. A.; Harrison, W. T. A.; Guloy, A. M. *Nature* **1994**, *369*, 467–469, DOI: 10.1038/369467a0.
- [106] Chondroudis, K.; Mitzi, D. B. *Chemistry of Materials* **1999**, *11*, 3028–3030, DOI: 10.1021/cm990561t, Publisher: American Chemical Society.
- [107] Kojima, A.; Teshima, K.; Shirai, Y.; Miyasaka, T. *Journal of the American Chemical Society* **2009**, *131*, 6050–6051, DOI: 10.1021/ja809598r, Publisher: American Chemical Society.
- [108] Baikie, T.; Fang, Y.; Kadro, J. M.; Schreyer, M.; Wei, F.; Mhaisalkar, S. G.; Graetzel, M.; White, T. J. *Journal of Materials Chemistry A* **2013**, *1*, 5628–5641, DOI: 10.1039/C3TA10518K, Publisher: The Royal Society of Chemistry.
- [109] Ganose, A. M.; Savory, C. N.; Scanlon, D. O. *Chemical Communications* **2016**, *53*, 20–44, DOI: 10.1039/C6CC06475B, Publisher: The Royal Society of Chemistry.
- [110] Bati, A.; Zhong, Y. L.; Burn, P.; Nazeeruddin, M.; Shaw, P.; Batmunkh, M. *Communications Materials* **2023**, *4*, DOI: 10.1038/s43246-022-00325-4.
- [111] Dong, Q.; Fang, Y.; Shao, Y.; Mulligan, P.; Qiu, J.; Cao, L.; Huang, J. *Science* **2015**, *347*, 967–970, DOI: 10.1126/science.aaa5760, Publisher: American Association for the Advancement of Science.
- [112] McMeekin, D. P.; Sadoughi, G.; Rehman, W.; Eperon, G. E.; Saliba, M.; Hörantner, M. T.; Haghhighirad, A.; Sakai, N.; Korte, L.; Rech, B.; John-

- ston, M. B.; Herz, L. M.; Snaith, H. J. *Science* **2016**, *351*, 151–155, DOI: 10.1126/science.aad5845, Publisher: American Association for the Advancement of Science.
- [113] Shi, D. et al. *Science* **2015**, *347*, 519–522, DOI: 10.1126/science.aaa2725, Publisher: American Association for the Advancement of Science.
- [114] Nie, W.; Tsai, H.; Asadpour, R.; Blancon, J.-C.; Neukirch, A. J.; Gupta, G.; Crochet, J. J.; Chhowalla, M.; Tretiak, S.; Alam, M. A.; Wang, H.-L.; Mohite, A. D. *Science* **2015**, *347*, 522–525, DOI: 10.1126/science.aaa0472, Publisher: American Association for the Advancement of Science.
- 6 [115] Walsh, A.; Scanlon, D. O.; Chen, S.; Gong, X. G.; Wei, S.-H. *Angewandte Chemie (International Ed. in English)* **2015**, *54*, 1791–1794, DOI: 10.1002/anie.201409740.
- [116] Deng, Y.; Peng, E.; Shao, Y.; Xiao, Z.; Dong, Q.; Huang, J. *Energy & Environmental Science* **2015**, *8*, 1544–1550, DOI: 10.1039/C4EE03907F, Publisher: The Royal Society of Chemistry.
- [117] Xing, G.; Mathews, N.; Sun, S.; Lim, S. S.; Lam, Y. M.; Grätzel, M.; Mhaisalkar, S.; Sum, T. C. *Science (New York, N.Y.)* **2013**, *342*, 344–347, DOI: 10.1126/science.1243167.
- [118] Zhao, Y.; Zhu, K. *The Journal of Physical Chemistry Letters* **2013**, *4*, 2880–2884, DOI: 10.1021/jz401527q, Publisher: American Chemical Society.
- [119] Shao, Y.; Xiao, Z.; Bi, C.; Yuan, Y.; Huang, J. *Nature Communications* **2014**, *5*, 5784, DOI: 10.1038/ncomms6784.
- [120] Manser, J. S.; Christians, J. A.; Kamat, P. V. *Chemical Reviews* **2016**, *116*, 12956–13008, DOI: 10.1021/acs.chemrev.6b00136.

- [121] Motta, C.; El-Mellouhi, F.; Sanvito, S. *Scientific Reports* **2015**, *5*, 12746, DOI: 10.1038/srep12746, Publisher: Nature Publishing Group.
- [122] Dubey, A.; Adhikari, N.; Mabrouk, S.; Wu, F.; Chen, K.; Yang, S.; Qiao, Q. *Journal of Materials Chemistry A* **2018**, *6*, 2406–2431, DOI: 10.1039/C7TA08277K, Publisher: The Royal Society of Chemistry.
- [123] Yin, W.-J.; Yang, J.-H.; Kang, J.; Yan, Y.; Wei, S.-H. *Journal of Materials Chemistry A* **2015**, *3*, 8926–8942, DOI: 10.1039/C4TA05033A, Publisher: The Royal Society of Chemistry.
- [124] Niu, G.; Guo, X.; Wang, L. *Journal of Materials Chemistry A* **2015**, *3*, 8970–8980, DOI: 10.1039/C4TA04994B, Publisher: The Royal Society of Chemistry.
- [125] Berhe, T. A.; Su, W.-N.; Chen, C.-H.; Pan, C.-J.; Cheng, J.-H.; Chen, H.-M.; Tsai, M.-C.; Chen, L.-Y.; Dubale, A. A.; Hwang, B.-J. *Energy & Environmental Science* **2016**, *9*, 323–356, DOI: 10.1039/C5EE02733K, Publisher: The Royal Society of Chemistry.
- [126] Domanski, K.; Alharbi, E. A.; Hagfeldt, A.; Grätzel, M.; Tress, W. *Nature Energy* **2018**, *3*, 61–67, DOI: 10.1038/s41560-017-0060-5.
- [127] Jena, A. K.; Kulkarni, A.; Miyasaka, T. *Chemical Reviews* **2019**, *119*, 3036–3103, DOI: 10.1021/acs.chemrev.8b00539, Publisher: American Chemical Society.
- [128] Ruan, S.; Surmiak, M.-A.; Ruan, Y.; McMeekin, D. P.; Ebendorff-Heidepriem, H.; Cheng, Y.-B.; Lu, J.; McNeill, C. R. *Journal of Materials Chemistry C* **2019**, *7*, 9326–9334, DOI: 10.1039/C9TC02635E, Publisher: The Royal Society of Chemistry.

- [129] Bryant, D.; Aristidou, N.; Pont, S.; Sanchez-Molina, I.; Chotchunangatchaval, T.; Wheeler, S.; Durrant, J. R.; Haque, S. A. *Energy & Environmental Science* **2016**, *9*, 1655–1660, DOI: 10.1039/C6EE00409A.
- [130] Abdelmageed, G.; Mackeen, C.; Hellier, K.; Jewell, L.; Seymour, L.; Tingwald, M.; Bridges, F.; Zhang, J. Z.; Carter, S. *Solar Energy Materials and Solar Cells* **2018**, *174*, 566–571, DOI: 10.1016/j.solmat.2017.09.053.
- [131] Wali, Q.; Aamir, M.; Ullah, A.; Iftikhar, F. J.; Khan, M. E.; Akhtar, J.; Yang, S. *The Chemical Record* **2022**, *22*, e202100150, DOI: 10.1002/tcr.202100150.
- [132] Ponti, C.; Nasti, G.; Di Girolamo, D.; Cantone, I.; Alharthi, F. A.; Abate, A. *Trends in Ecology & Evolution* **2022**, *37*, 281–283, DOI: 10.1016/j.tree.2022.01.002.
- [133] Wang, H.; Liu, H.; Dong, Z.; Wei, X.; Li, W.; Zhu, L.; Zhu, C.; Bai, Y.; Chen, H. *Science Bulletin* **2023**, *68*, 192–202, DOI: 10.1016/j.scib.2023.01.016.
- [134] Mendez L., R. D.; Breen, B. N.; Cahen, D. *ACS Applied Materials & Interfaces* **2022**, *14*, 29766–29772, DOI: 10.1021/acsami.2c05074.
- [135] Worsley, C.; Raptis, D.; Meroni, S.; Doolin, A.; GarciaRodriguez, R.; Davies, M.; Watson, T. *Energy Technology* **2021**, *9*, 2100312, DOI: 10.1002/ente.202100312.
- [136] Lindquist, K. P.; Lee, T.; Xu, X.; Cava, R. J. *Chemistry of Materials* **2024**, *36*, 7610–7618, DOI: 10.1021/acs.chemmater.4c01880.
- [137] Mahmoudi, T.; Rho, W.-Y.; Kohan, M.; Im, Y. H.; Mathur, S.; Hahn, Y.-B. *Nano Energy* **2021**, *90*, 106495, DOI: 10.1016/j.nanoen.2021.106495.
- [138] Euvrard, J.; Yan, Y.; Mitzi, D. B. *Nature Reviews Materials* **2021**, *6*, 531–549, DOI: 10.1038/s41578-021-00286-z, Publisher: Nature Publishing Group.

- [139] Quan, J.; Yu, S.; Xing, B.; He, X.; Zhang, L. *Physical Review Materials* **2022**, *6*, 065405, DOI: 10.1103/PhysRevMaterials.6.065405.
- [140] Ding, P.; Li, W.; Zhao, H.; Wu, C.; Zhao, L.; Dong, B.; Wang, S. *Journal of Physics: Materials* **2021**, *4*, 022002, DOI: 10.1088/2515-7639/abe392.
- [141] Perera, S.; Hui, H.; Zhao, C.; Xue, H.; Sun, F.; Deng, C.; Gross, N.; Milleville, C.; Xu, X.; Watson, D. F.; Weinstein, B.; Sun, Y.-Y.; Zhang, S.; Zeng, H. *Nano Energy* **2016**, *22*, 129–135, DOI: 10.1016/j.nanoen.2016.02.020.
- [142] Han, Y.; Fang, X.; Shi, Z. *Applied Physics Reviews* **2024**, *11*, 021338, DOI: 10.1063/5.0203535.
- [143] Jess, A.; Yang, R.; Hages, C. J. *Chemistry of Materials* **2022**, *34*, 6894–6901, DOI: 10.1021/acs.chemmater.2c01289.
- [144] Choi, J.-Y.; Cho, J.-H.; Sun, J.-W.; Kim, H.-P.; Ryu, J.; Durmus, Y.; Tempel, H.; Eichel, R.-A.; Jo, W. *Materials Today Chemistry* **2023**, *32*, 101645, DOI: 10.1016/j.mtchem.2023.101645.
- [145] Tiwari, D.; Hutter, O. S.; Longo, G. *Journal of Physics: Energy* **2021**, *3*, 034010, DOI: 10.1088/2515-7655/abf41c.
- [146] Suhail, M.; Abbas, H.; Khan, M. B.; Khan, Z. H. *Journal of Nanoparticle Research* **2022**, *24*, 142, DOI: 10.1007/s11051-022-05525-0.
- [147] Niu, S.; Huyan, H.; Liu, Y.; Yeung, M.; Ye, K.; Blankemeier, L.; Orvis, T.; Sarkar, D.; Singh, D. J.; Kapadia, R.; Ravichandran, J. *Advanced Materials* **2017**, *29*, 1604733, DOI: 10.1002/adma.201604733, \_eprint: <https://onlinelibrary.wiley.com/doi/pdf/10.1002/adma.201604733>.
- [148] Osei-Agyemang, E.; Koratkar, N.; Balasubramanian, G. *Journal of Materials Chemistry C* **2021**, *9*, 3892–3900, DOI: 10.1039/D1TC00374G.

- [149] Wei, X. et al. *Nano Energy* **2020**, *68*, 104317, DOI: 10.1016/j.nanoen.2019.104317.
- [150] Mitzi, D.; Yan, Y. *High Performance Perovskite-Based Solar Cells (Final Technical Report)*; 2019; pp DOE-DUKE-06712-1, 1582433, DOI: 10.2172/1582433.
- [151] Wei, X.; Hui, H.; Perera, S.; Sheng, A.; Watson, D. F.; Sun, Y.-Y.; Jia, Q.; Zhang, S.; Zeng, H. *ACS Omega* **2020**, *5*, 18579–18583, DOI: 10.1021/acsomega.0c00740.
- [152] Clearfield, A. *Acta Crystallographica* **1963**, *16*, 135–142, DOI: 10.1107/S0365110X6300030X.
- [153] Comparotto, C.; Davydova, A.; Ericson, T.; Riekehr, L.; Moro, M. V.; Kubart, T.; Scragg, J. *ACS Applied Energy Materials* **2020**, *3*, 2762–2770, DOI: 10.1021/acsaem.9b02428.
- [154] Lelieveld, R.; IJdo, D. J. W. *Acta Crystallographica Section B* **1980**, *36*, 2223–2226, DOI: 10.1107/S056774088000845X, \_eprint: <https://onlinelibrary.wiley.com/doi/pdf/10.1107/S056774088000845X>.
- [155] Okai, B.; Takahashi, K.; Saeki, M.; Yoshimoto, J. *Materials Research Bulletin* **1988**, *23*, 1575–1584, DOI: 10.1016/0025-5408(88)90245-0.
- [156] Hanzawa, K.; Iimura, S.; Hiramatsu, H.; Hosono, H. *Journal of the American Chemical Society* **2019**, *141*, 5343–5349, DOI: 10.1021/jacs.8b13622.
- [157] Lee, C.-S.; Kleinke, K. M.; Kleinke, H. *Solid State Sciences* **2005**, *7*, 1049–1054, DOI: 10.1016/j.solidstatesciences.2005.02.010.
- [158] Mar, A.; Ibers, J. A. *Acta Crystallographica Section C: Crystal Structure Communications* **1992**, *48*, 771–773, DOI: 10.1107/S0108270191011599, Publisher: International Union of Crystallography.

- [159] Han, Y.; Fang, J.; Zhang, H.; Sun, Y.; Yuan, Y.; Chen, X.; Jia, M.; Li, X.; Gao, H.; Shi, Z. *Energy Material Advances* **2024**, *5*, 0116, DOI: 10.34133/energymatadv.0116.
- [160] Wang, Y.; Sato, N.; Yamada, K.; Fujino, T. *Shigen-to-Sozai* **2000**, *116*, 703–710, DOI: 10.2473/shigentosozai.116.703.
- [161] Meng, W.; Saparov, B.; Hong, F.; Wang, J.; Mitzi, D. B.; Yan, Y. *Chemistry of Materials* **2016**, *28*, 821–829, DOI: 10.1021/acs.chemmater.5b04213, Publisher: American Chemical Society.
- [162] Kikkawa, S.; Fujii, Y.; Miyamoto, Y.; Meerschaut, A.; Lafond, A.; Rouxel, J. *Materials Research Bulletin* **1999**, *34*, 279–288, DOI: 10.1016/S0025-5408(99)00015-X.
- [163] Murugesan, T.; Ramesh, S.; Gopalakrishnan, J.; Rao, C. N. R. *Journal of Solid State Chemistry* **1981**, *38*, 165–172, DOI: 10.1016/0022-4596(81)90031-1.
- [164] Cho, N.; Kikkawa, S.; Kanamaru, F.; Takeda, Y.; Yamamoto, O.; Kido, H.; Hoshikawa, T. *Solid State Ionics* **1993**, *63-65*, 696–701, DOI: 10.1016/0167-2738(93)90182-3.
- [165] Takahashi, T.; Ametani, K.; Yamada, O. *Journal of Crystal Growth* **1974**, *24-25*, 151–153, DOI: 10.1016/0022-0248(74)90293-0.
- [166] Ward, M.; Oh, G.; Mesbah, A.; Lee, M.; Sang Choi, E.; Ibers, J. *Journal of Solid State Chemistry* **2015**, *228*, 14–19, DOI: 10.1016/j.jssc.2015.04.005, Publisher: Elsevier.
- [167] Prakash, J.; Tarasenko, M. S.; Mesbah, A.; Lebègue, S.; Malliakas, C. D.; Ibers, J. A. *Inorganic chemistry* **2016**, *55*, 7734–7738, DOI: 10.1021/acs.inorgchem.6b01202.

- [168] Tranchitella, L. J.; Chen, B.-H.; Fettinger, J. C.; Eichhorn, B. W. *Journal of Solid State Chemistry* **1997**, *130*, 20–27, DOI: 10.1006/jssc.1996.7253.
- [169] Moroz, N. A.; Bauer, C.; Williams, L.; Olvera, A.; Casamento, J.; Page, A. A.; Bailey, T. P.; Weiland, A.; Stoyko, S. S.; Kioupakis, E.; Uher, C.; Aitken, J. A.; Poudeu, P. F. P. *Inorganic Chemistry* **2018**, *57*, 7402–7411, DOI: 10.1021/acs.inorgchem.8b01038.
- [170] Moroz, N. Engineered Transition Metal Chalcogenides for Photovoltaic, Thermoelectric, and Magnetic Applications. Thesis, 2017; Accepted: 2017-06-14T18:35:36Z.
- [171] Yamaoka, S.; Okai, B. *Materials Research Bulletin* **1970**, *5*, 789–794, DOI: 10.1016/0025-5408(70)90093-0.
- [172] Fagot, S.; Foury-Leylekian, P.; Ravy, S.; Pouget, J. P.; Anne, M.; Popov, G.; Lobanov, M. V.; Greenblatt, M. *Solid State Sciences* **2005**, *7*, 718–725, DOI: 10.1016/j.solidstatesciences.2004.11.017.
- [173] Jin, G. B.; Choi, E. S.; Guertin, R. P.; Brooks, J. S.; Bray, T. H.; Booth, C. H.; Albrecht-Schmitt, T. E. *Chemistry of Materials* **2007**, *19*, 567–574, DOI: 10.1021/cm062349c, Publisher: American Chemical Society.
- [174] Ohtani, T.; Honji, S.; Takano, M. *Journal of Solid State Chemistry* **1997**, *132*, 188–195, DOI: 10.1006/jssc.1997.7443.
- [175] Guo, S.-P.; Chi, Y.; Zou, J.-P.; Xue, H. *New J. Chem.* **2016**, *40*, 10219–10226, DOI: 10.1039/C6NJ02106A.
- [176] Donohue, P. C.; Weiher, J. F. *Journal of Solid State Chemistry* **1974**, *10*, 142–144, DOI: 10.1016/0022-4596(74)90020-6.
- [177] Crovetto, A.; Nielsen, R.; Pandey, M.; Watts, L.; Labram, J. G.; Geisler, M.; Stenger, N.; Jacobsen, K. W.; Hansen, O.; Seger, B.; Chorkendorff, I.;

- Vesborg, P. C. K. *Chemistry of Materials* **2019**, *31*, 3359–3369, DOI: 10.1021/acs.chemmater.9b00478.
- [178] Rodier, N.; Julien, R.; Tien, V. *Acta Crystallographica Section C* **1983**, *39*, 670–673, DOI: 10.1107/S0108270183005879, \_eprint: <https://onlinelibrary.wiley.com/doi/pdf/10.1107/S0108270183005879>.
- [179] Kadijk, F.; Huisman, R.; Jellinek, F. *Recueil des Travaux Chimiques des Pays-Bas* **1964**, *83*, 768–775, DOI: 10.1002/recl.19640830718, \_eprint: <https://onlinelibrary.wiley.com/doi/pdf/10.1002/recl.19640830718>.
- [180] Mitchell, K.; Somers, R. C.; Huang, F. Q.; Ibers, J. A. *Journal of Solid State Chemistry* **2004**, *177*, 709–713, DOI: 10.1016/j.jssc.2003.08.024.
- [181] Shaili, H.; Salmani, E.; Beraich, M.; Zidane, M.; Taibi, M.; Rouchdi, M.; Ez-Zahraouy, H.; Hassanain, N.; Mzerd, A. *ACS Omega* **2021**, *6*, 32537–32547, DOI: 10.1021/acsomega.1c04054, Publisher: American Chemical Society.
- [182] Ohno, Y. *Solid State Communications* **1991**, *79*, 1081–1084, DOI: 10.1016/0038-1098(91)90015-N.
- [183] Shen, X.; Cheng, D.; Zhao, H.-F.; Yao, Y.; Liu, X.-Y.; Yu, R. C. *Chinese Physics B* **2013**, *22*, 6102, DOI: 10.1088/1674-1056/22/11/116102.
- [184] Wiegers, G. A.; Meetsma, A.; Haange, R. J.; De Boer, J. L. *Acta Crystallographica Section C Crystal Structure Communications* **1989**, *45*, 847–849, DOI: 10.1107/S0108270188014647.
- [185] Kelber, J.; Reis, A. H.; Aldred, A. T.; Mueller, M. H.; Massenet, O.; De-Pasquali, G.; Stucky, G. *Journal of Solid State Chemistry* **1979**, *30*, 357–364, DOI: 10.1016/0022-4596(79)90248-2.
- [186] Onoda, M.; Kato, K.; Gotoh, Y.; Oosawa, Y. *Acta Crystallographica Section*

- B: Structural Science **1990**, *46*, 487–492, DOI: 10.1107/S0108768190003950, Publisher: International Union of Crystallography.
- [187] Mootz, D.; Puhl, H. *Acta Crystallographica* **1967**, *23*, 471–476, DOI: 10.1107/S0365110X67002993.
- [188] Sourisseau, C.; Cavagnat, R.; Tirado, J. L. *Journal of Raman Spectroscopy* **1992**, *23*, 647–651, DOI: 10.1002/jrs.1250231114, eprint: <https://onlinelibrary.wiley.com/doi/pdf/10.1002/jrs.1250231114>.
- [189] Jin, G. B.; Choi, E. S.; Albrecht-Schmitt, T. E. *Journal of Solid State Chemistry* **2009**, *182*, 1075–1081, DOI: 10.1016/j.jssc.2009.02.002.
- 6  
[190] Tranchitella, L. J.; Fettinger, J. C.; Dorhout, P. K.; Van Calcar, P. M.; Eichhorn, B. W. *Journal of the American Chemical Society* **1998**, *120*, 7639–7640, DOI: 10.1021/ja972442p, Publisher: American Chemical Society.
- [191] Ward, M. D.; Ibers, J. A. *Acta Crystallographica Section E: Structure Reports Online* **2014**, *70*, i4, DOI: 10.1107/S1600536813033680.
- [192] Shaili, H.; Beraich, M.; El Hat, A.; Oua, M.; Salmani, E. M.; Essajai, R.; Battal, W.; Rouchdi, M.; Taibi, M.; Hassanain, N.; Mzerd, A. *Journal of Alloys and Compounds* **2021**, *851*, 156790, DOI: 10.1016/j.jallcom.2020.156790.
- [193] Pilania, G.; Ghosh, A.; Hartman, S. T.; Mishra, R.; Stanek, C. R.; Uberuaga, B. P. *npj Computational Materials* **2020**, *6*, 1–11, DOI: 10.1038/s41524-020-0338-1, Publisher: Nature Publishing Group.
- [194] Shannon, R. D.; Prewitt, C. T. *Acta Crystallographica Section B Structural Crystallography and Crystal Chemistry* **1969**, *25*, 925–946, DOI: 10.1107/S0567740869003220.
- [195] Brehm, J. A.; Bennett, J. W.; Schoenberg, M. R.; Grinberg, I.; Rappe, A. M. *The Journal of Chemical Physics* **2014**, *140*, 224703, DOI: 10.1063/1.4879659.

- [196] Kieslich, G.; Sun, S.; Cheetham, A. K. *Chemical Science* **2014**, *5*, 4712–4715, DOI: 10.1039/C4SC02211D, Publisher: The Royal Society of Chemistry.
- [197] Glazer, A. M. *Acta Crystallographica Section B Structural Crystallography and Crystal Chemistry* **1972**, *28*, 3384–3392, DOI: 10.1107/S0567740872007976.
- [198] Bennett, J. W.; Grinberg, I.; Rappe, A. M. *Physical Review B* **2009**, *79*, 235115, DOI: 10.1103/PhysRevB.79.235115.
- [199] Thakur, N.; Kumar, P.; Neffati, R.; Sharma, P. *Physica Scripta* **2023**, *98*, 065921, DOI: 10.1088/1402-4896/acfc6.
- [200] Gardiner, R. W.; Goodwin, P. S.; Dodd, S. B.; Viney, B. W. *Advanced Performance Materials* **1996**, *3*, 343–364, DOI: 10.1007/BF00136796.
- [201] Maeder, X.; Döbeli, M.; Dommann, A.; Neels, A.; Rudigier, H.; Widrig, B.; Ramm, J. *Surface and Coatings Technology* **2014**, *260*, 56–62, DOI: 10.1016/j.surfcoat.2014.07.095.
- [202] Bretos, I.; Jiménez, R.; Ricote, J.; Calzada, M. L. *Chemistry A European Journal* **2020**, *26*, 9277–9291, DOI: 10.1002/chem.202000244.
- [203] Filippone, S. A.; Sun, Y.-Y.; Jaramillo, R. *MRS Advances* **2018**, *3*, 3249–3254, DOI: 10.1557/adv.2018.497.
- [204] Yamamoto, A. *Solid State Ionics* **1998**, *108*, 333–336, DOI: 10.1016/S0167-2738(98)00059-9.
- [205] Hester, J. R.; Howard, C. J.; Kennedy, B. J.; Macquart, R. *Australian Journal of Chemistry* **2002**, *55*, 543, DOI: 10.1071/CH02023.
- [206] Susaki, J.-i. *Physics and Chemistry of Minerals* **1989**, *16*, DOI: 10.1007/BF00223311.

- [207] Inaguma, Y.; Yoshida, M.; Tsuchiya, T.; Aimi, A.; Tanaka, K.; Katsumata, T.; Mori, D. *Journal of Physics: Conference Series* **2010**, *215*, 012131, DOI: 10.1088/1742-6596/215/1/012131.
- [208] Smith, A. J. *Acta Crystallographica* **1960**, *13*, 749–752, DOI: 10.1107/S0365110X60001813.
- [209] Pradhan, A. A.; Uible, M. C.; Agarwal, S.; Turnley, J. W.; Khan-delwal, S.; Peterson, J. M.; Blach, D. D.; Swope, R. N.; Huang, L.; Bart, S. C.; Agrawal, R. *Angewandte Chemie International Edition* **2023**, *62*, e202301049, DOI: 10.1002/anie.202301049, \_eprint: <https://onlinelibrary.wiley.com/doi/pdf/10.1002/anie.202301049>.
- [210] Park, H.; Mall, R.; Alharbi, F. H.; Sanvito, S.; Tabet, N.; Bensmail, H.; El-Mellouhi, F. *Physical Chemistry Chemical Physics* **2019**, *21*, 1078–1088, DOI: 10.1039/C8CP06528D, Publisher: The Royal Society of Chemistry.
- [211] Thakur, N.; Aly, K.; Mohery, M.; Ebrahium, M.; Kumar, P.; Sharma, P. *Journal of Alloys and Compounds* **2023**, *957*, 170457, DOI: 10.1016/j.jallcom.2023.170457.
- [212] Mosconi, E.; Azpiroz, J. M.; De Angelis, F. *Chemistry of Materials* **2015**, *27*, 4885–4892, DOI: 10.1021/acs.chemmater.5b01991.
- [213] Strontium | Toxicological Profile | ATSDR. <https://www.cdc.gov/TSP/ToxProfiles/ToxProfiles.aspx?id=656&tid=120>.
- [214] Ghosh, S.; Sharma, A.; Talukder, G. *Biological Trace Element Research* **1992**, *35*, 247–271, DOI: 10.1007/BF02783770.
- [215] *Toxicological Profile for Barium and Barium Compounds*; Agency for Toxic Substances and Disease Registry (US), 2007.

- [216] MacFarquhar, J. K. *Archives of Internal Medicine* **2010**, *170*, 256, DOI: 10.1001/archinternmed.2009.495.
- [217] Márquez, J. A.; Rusu, M.; Hempel, H.; Ahmet, I. Y.; Kölbach, M.; Simsek, I.; Choubrac, L.; Gurieva, G.; Gunder, R.; Schorr, S.; Unold, T. *The Journal of Physical Chemistry Letters* **2021**, *12*, 2148–2153, DOI: 10.1021/acs.jpclett.1c00177.
- [218] Peng, Y.; Sun, Q.; Chen, H.; Yin, W.-J. *The Journal of Physical Chemistry Letters* **2019**, *10*, 4566–4570, DOI: 10.1021/acs.jpclett.9b01657, Publisher: American Chemical Society.
- [219] Ponce, S. *ACS Energy Letters* **2019**,
- [220] Zhang, X.; Turiansky, M. E.; Shen, J.-X.; Van De Walle, C. G. *Physical Review B* **2020**, *101*, 140101, DOI: 10.1103/PhysRevB.101.140101.
- [221] Wang, Y.; Sato, N.; Fujino, T. *Journal of Alloys and Compounds* **2001**, *327*, 104–112, DOI: 10.1016/S0925-8388(01)01553-5.
- [222] Ramanandan, S. P.; Giunto, A.; Stutz, E. Z.; Reynier, B.; Lefevre, I. T. F. M.; Rusu, M.; Schorr, S.; Unold, T.; Fontcuberta I Morral, A.; Márquez, J. A.; Dimitrievska, M. *Journal of Physics: Energy* **2023**, *5*, 014013, DOI: 10.1088/2515-7655/aca9fe.
- [223] Vincent, K.; Agarwal, S.; Turnley, J.; Agrawal, R. *Advanced Energy and Sustainability Research* **2023**, *4*, DOI: 10.1002/aesr.202300010.
- [224] Comparotto, C.; Ström, P.; Donzel-Gargand, O.; Kubart, T.; Scragg, J. J. S. *ACS Applied Energy Materials* **2022**, *5*, 6335–6343, DOI: 10.1021/acsmaem.2c00704, Publisher: American Chemical Society.

- [225] Yu, Z.; Wei, X.; Zheng, Y.; Hui, H.; Bian, M.; Dhole, S.; Seo, J.-H.; Sun, Y.-Y.; Jia, Q.; Zhang, S.; Yang, S.; Zeng, H. *Nano Energy* **2021**, *85*, 105959, DOI: 10.1016/j.nanoen.2021.105959.
- [226] Ravi, V. K.; Yu, S. H.; Rajput, P. K.; Nayak, C.; Bhattacharyya, D.; Chung, D. S.; Nag, A. *Nanoscale* **2021**, *13*, 1616–1623, DOI: 10.1039/D0NR08078K, Publisher: The Royal Society of Chemistry.
- [227] Dallas, P.; Gkini, K.; Kaltzoglou, A.; Givalou, L.; Konstantakou, M.; Orfanoudakis, S.; Boukos, N.; Sakellis, E.; Tsipas, P.; Kalafatis, A.; Karydas, A.; Lagogiannis, A.; Falaras, P.; Pscharis, V.; Stergiopoulos, T. *Materials Today Communications* **2024**, *39*, 108608, DOI: 10.1016/j.mtcomm.2024.108608.
- [228] Sunshine, S. A.; Ibers, J. A. *Acta Crystallographica Section C Crystal Structure Communications* **1987**, *43*, 1019–1022, DOI: 10.1107/S0108270187093168.
- [229] Chen, C.; Chu, L.; Qing, F.-L. *Journal of the American Chemical Society* **2012**, *134*, 12454–12457, DOI: 10.1021/ja305801m.
- [230] Kuhar, K.; Crovetto, A.; Pandey, M.; Thygesen, K. S.; Seger, B.; Vesborg, P. C. K.; Hansen, O.; Chorkendorff, I.; Jacobsen, K. W. *Energy & Environmental Science* **2017**, *10*, 2579–2593, DOI: 10.1039/C7EE02702H.
- [231] Mukherjee, S.; Riva, S.; Comparotto, C.; Johansson, F. O. L.; Man, G. J.; Phuyal, D.; Simonov, K. A.; Just, J.; Klementiev, K.; Butorin, S. M.; Scragg, J. J. S.; Rensmo, H. *ACS Applied Energy Materials* **2023**, *6*, 11642–11653, DOI: 10.1021/acsadm.3c02075, Publisher: American Chemical Society.
- [232] Göltl, F.; Sautet, P. *Comprehensive Inorganic Chemistry II*; Elsevier, 2013; pp 405–420, DOI: 10.1016/B978-0-08-097774-4.00734-8.
- [233] Fock, V. *Zeitschrift für Physik* **1930**, *61*, 126–148, DOI: 10.1007/BF01340294.

- [234] Thompson, D. C.; Rodríguez, J. I. In *Advances in Quantum Chemical Topology Beyond QTAIM*; Rodríguez, J. I., Cortés-Guzmán, F., Anderson, J. S. M., Eds.; Elsevier, 2023; pp 21–36, DOI: 10.1016/B978-0-323-90891-7.00012-8.
- [235] Verdaguer, M.; Robert, V. *Comprehensive Inorganic Chemistry II*; Elsevier, 2013; pp 131–189, DOI: 10.1016/B978-0-08-097774-4.00819-6.
- [236] Schettino, V.; Mugnai, M. *Encyclopedia of Condensed Matter Physics*; Elsevier, 2005; pp 67–76, DOI: 10.1016/B0-12-369401-9/00630-6.
- [237] Kadanoff, L. P. **2009**, DOI: 10.48550/ARXIV.0906.0653, Publisher: arXiv Version Number: 2.
- [238] Hartree, D. R. *Mathematical Proceedings of the Cambridge Philosophical Society* **1928**, *24*, 89–110, DOI: 10.1017/S0305004100011919.
- [239] Band, Y. B.; Avishai, Y. *Quantum Mechanics with Applications to Nanotechnology and Information Science*; Elsevier, 2013; pp 579–603, DOI: 10.1016/B978-0-444-53786-7.00011-3.
- [240] S, D. R. H. F. R. *Reports on Progress in Physics* **1947**, *11*, 113–143, DOI: 10.1088/0034-4885/11/1/305.
- [241] Slater, J. C. *Physical Review* **1929**, *34*, 1293–1322, DOI: 10.1103/PhysRev.34.1293.
- [242] Kaplan, T. A.; Kleiner, W. H. *Physical Review* **1967**, *156*, 1–11, DOI: 10.1103/PhysRev.156.1.
- [243] Slater, J. C. *Reviews of Modern Physics* **1963**, *35*, 484–487, DOI: 10.1103/RevModPhys.35.484.
- [244] Gulania, S.; Whitfield, J. D. *The Journal of Chemical Physics* **2021**, *154*, 044112, DOI: 10.1063/5.0018415.

- [245] N. M. Harrison An Introduction to Density Functional Theory. [https://www.imperial.ac.uk/media/imperial-college-research-centres-and-groups/computational-materials-science/teaching/DFT\\_NATO.pdf](https://www.imperial.ac.uk/media/imperial-college-research-centres-and-groups/computational-materials-science/teaching/DFT_NATO.pdf).
- [246] Calais, J. *International Journal of Quantum Chemistry* **1993**, *47*, 101–101, DOI: 10.1002/qua.560470107.
- [247] Thomas, L. H. *Mathematical Proceedings of the Cambridge Philosophical Society* **1927**, *23*, 542–548, DOI: 10.1017/S0305004100011683.
- [248] Hohenberg, P.; Kohn, W. *Physical Review* **1964**, *136*, B864–B871, DOI: 10.1103/PhysRev.136.B864.
- [249] Kohn, W.; Sham, L. J. *Physical Review* **1965**, *140*, A1133–A1138, DOI: 10.1103/PhysRev.140.A1133.
- [250] Perdew, J. P. *Comprehensive Computational Chemistry*; Elsevier, 2024; pp 69–77, DOI: 10.1016/B978-0-12-821978-2.00125-2.
- [251] Ceperley, D. M.; Alder, B. J. *Physical Review Letters* **1980**, *45*, 566–569, DOI: 10.1103/PhysRevLett.45.566.
- [252] Vosko, S. H.; Wilk, L.; Nusair, M. *Canadian Journal of Physics* **1980**, *58*, 1200–1211, DOI: 10.1139/p80-159.
- [253] Gedeon, J.; Schmidt, J.; Hodgson, M. J. P.; Wetherell, J.; Benavides-Riveros, C. L.; Marques, M. A. L. *Machine Learning: Science and Technology* **2022**, *3*, 015011, DOI: 10.1088/2632-2153/ac3149.
- [254] Perdew, J. P.; Yue, W. *Physical Review B* **1986**, *33*, 8800–8802, DOI: 10.1103/PhysRevB.33.8800.

- [255] Perdew, J. P.; Burke, K.; Ernzerhof, M. *Physical Review Letters* **1996**, *77*, 3865–3868, DOI: 10.1103/PhysRevLett.77.3865, Publisher: American Physical Society.
- [256] Csonka, G. I.; Perdew, J. P.; Ruzsinszky, A.; Philipsen, P. H. T.; Lebègue, S.; Paier, J.; Vydrov, O. A.; Ángyán, J. G. *Physical Review B* **2009**, *79*, 155107, DOI: 10.1103/PhysRevB.79.155107, Publisher: American Physical Society.
- [257] Perdew, J. P.; Ruzsinszky, A.; Csonka, G. I.; Vydrov, O. A.; Scuseria, G. E.; Constantin, L. A.; Zhou, X.; Burke, K. *Physical Review Letters* **2008**, *100*, 136406, DOI: 10.1103/PhysRevLett.100.136406, Publisher: American Physical Society.
- [258] Bao, J. L.; Gagliardi, L.; Truhlar, D. G. *The Journal of Physical Chemistry Letters* **2018**, *9*, 2353–2358, DOI: 10.1021/acs.jpclett.8b00242.
- [259] Perdew, J. P.; Chevary, J. A.; Vosko, S. H.; Jackson, K. A.; Pederson, M. R.; Singh, D. J.; Fiolhais, C. *Physical Review B* **1992**, *46*, 6671–6687, DOI: 10.1103/PhysRevB.46.6671.
- [260] Adamo, C.; Barone, V. *The Journal of Chemical Physics* **1999**, *110*, 6158–6170, DOI: 10.1063/1.478522.
- [261] Perdew, J. P.; Ernzerhof, M.; Burke, K. *The Journal of Chemical Physics* **1996**, *105*, 9982–9985, DOI: 10.1063/1.472933.
- [262] Heyd, J.; Scuseria, G. E.; Ernzerhof, M. *The Journal of Chemical Physics* **2003**, *118*, 8207–8215, DOI: 10.1063/1.1564060.
- [263] Krukau, A. V.; Vydrov, O. A.; Izmaylov, A. F.; Scuseria, G. E. *The Journal of Chemical Physics* **2006**, *125*, 224106, DOI: 10.1063/1.2404663.
- [264] Bloch, F. *Zeitschrift für Physik* **1929**, *52*, 555–600, DOI: 10.1007/BF01339455.

- [265] Lehtola, S. *International Journal of Quantum Chemistry* **2019**, *119*, e25968, DOI: 10.1002/qua.25968.
- [266] Giustino, F. *Materials modelling using density functional theory: properties and predictions*, 1st ed.; Oxford University Press: Oxford, 2014; OCLC: ocn870986749.
- [267] Kresse, G.; Furthmüller, J. *Computational Materials Science* **1996**, *6*, 15–50, DOI: 10.1016/0927-0256(96)00008-0.
- [268] Blöchl, P. E. *Physical Review B* **1994**, *50*, 17953–17979, DOI: 10.1103/PhysRevB.50.17953, Publisher: American Physical Society.
- 6 [269] Rostgaard, C. The Projector Augmented-wave Method. 2009; <https://arxiv.org/abs/0910.1921>, Version Number: 2.
- [270] Ong, S. P.; Richards, W. D.; Jain, A.; Hautier, G.; Kocher, M.; Cholia, S.; Gunter, D.; Chevrier, V. L.; Persson, K. A.; Ceder, G. *Computational Materials Science* **2013**, *68*, 314–319, DOI: 10.1016/j.commatsci.2012.10.028.
- [271] Pulay, P. *Molecular Physics* **1969**, *17*, 197–204, DOI: 10.1080/00268976900100941.
- [272] Parrinello, M.; Rahman, A. *Physical Review Letters* **1980**, *45*, 1196–1199, DOI: 10.1103/PhysRevLett.45.1196.
- [273] Parrinello, M.; Rahman, A. *Journal of Applied Physics* **1981**, *52*, 7182–7190, DOI: 10.1063/1.328693.
- [274] Huang, J.; Shin, S.-J.; Tolborg, K.; Ganose, A. M.; Krenzer, G.; Walsh, A. *Materials Horizons* **2023**, *10*, 2883–2891, DOI: 10.1039/D3MH00314K.
- [275] Jinnouchi, R.; Lahnsteiner, J.; Karsai, F.; Kresse, G.; Bokdam, M. *Physical Review Letters* **2019**, *122*, 225701, DOI: 10.1103/PhysRevLett.122.225701.

- [276] Jinnouchi, R.; Karsai, F.; Kresse, G. *Physical Review B* **2019**, *100*, 014105, DOI: 10.1103/PhysRevB.100.014105.
- [277] Bartel, C. J. *Journal of Materials Science* **2022**, *57*, 10475–10498, DOI: 10.1007/s10853-022-06915-4.
- [278] Kavanagh, S. R.; Squires, A. G.; Nicolson, A.; Mosquera-Lois, I.; Ganose, A. M.; Zhu, B.; Brlec, K.; Walsh, A.; Scanlon, D. O. *Journal of Open Source Software* **2024**, *9*, 6433, DOI: 10.21105/joss.06433.
- [279] Marchiori, R. *Nanostructures*; Elsevier, 2017; pp 209–232, DOI: 10.1016/B978-0-323-49782-4.00008-5.
- [280] Fatima; Liao, Y.; Tolba, S. A.; Ruiz Pestana, L. A.; Xia, W. *Fundamentals of Multiscale Modeling of Structural Materials*; Elsevier, 2023; pp 3–35, DOI: 10.1016/B978-0-12-823021-3.00007-5.
- [281] Veerman, J. J. P.; Peixoto, M. M.; Rocha, A. C.; Sutherland, S. **1998**, DOI: 10.48550/ARXIV.MATH/9806154, Publisher: arXiv Version Number: 1.
- [282] Misra, P. K. *Physics of Condensed Matter*; Elsevier, 2012; pp 1–35, DOI: 10.1016/B978-0-12-384954-0.00001-3.
- [283] Solé, J. G.; Bausá, L.; Jaque, D. *An Introduction to the Optical Spectroscopy of Inorganic Solids*, 1st ed.; Wiley, 2005; DOI: 10.1002/0470016043.
- [284] Yu, L.; Zunger, A. *Physical Review Letters* **2012**, *108*, 068701, DOI: 10.1103/PhysRevLett.108.068701.
- [285] Yu, L.; Kokkenyesi, R. S.; Keszler, D. A.; Zunger, A. *Advanced Energy Materials* **2013**, *3*, 43–48, DOI: 10.1002/aenm.201200538.
- [286] Brlec, K.; Davies, D.; Scanlon, D. *Journal of Open Source Software* **2021**, *6*, 3171, DOI: 10.21105/joss.03171.

- [287] Qin, S. *Applied and Computational Engineering* **2023**, *7*, 14–23, DOI: 10.54254/2755-2721/7/20230312.
- [288] Fujiwara, H., Collins, R. W., Eds. *Spectroscopic Ellipsometry for Photovoltaics: Volume 2: Applications and Optical Data of Solar Cell Materials*; Springer Series in Optical Sciences; Springer International Publishing: Cham, 2018; Vol. 214; DOI: 10.1007/978-3-319-95138-6.
- [289] Ambrosio, F.; Wiktor, J.; De Angelis, F.; Pasquarello, A. *Energy & Environmental Science* **2018**, *11*, 101–105, DOI: 10.1039/C7EE01981E.
- [290] Madelung, O. *Semiconductors: Data Handbook*; Springer Berlin Heidelberg: Berlin, Heidelberg, 2004; DOI: 10.1007/978-3-642-18865-7.
- 6
- [291] Ganose, A. M.; Scanlon, D. O.; Walsh, A.; Hoye, R. L. Z. *Nature Communications* **2022**, *13*, 4715, DOI: 10.1038/s41467-022-32131-4, Publisher: Nature Publishing Group.
- [292] Huang, Y.-T.; Kavanagh, S. R.; Scanlon, D. O.; Walsh, A.; Hoye, R. L. Z. *Nanotechnology* **2021**, *32*, 132004, DOI: 10.1088/1361-6528/abcf6d.
- [293] Ormeño, F.; General, I. J. *Communications Chemistry* **2024**, *7*, 26, DOI: 10.1038/s42004-024-01114-5.
- [294] Lu, Q.; Zhang, B.; Zhang, L.; Zhu, Y.; Gong, W. *Nanomaterials* **2023**, *13*, 1553, DOI: 10.3390/nano13091553.
- [295] Harnett-Caulfield, L.; Walsh, A. *The Journal of Chemical Physics* **2021**, *155*, 024113, DOI: 10.1063/5.0044866.
- [296] Brivio, F.; Butler, K. T.; Walsh, A.; Van Schilfgaarde, M. *Physical Review B* **2014**, *89*, 155204, DOI: 10.1103/PhysRevB.89.155204.
- [297] Teeter, G. *Journal of Applied Physics* **2007**, *102*, 034504, DOI: 10.1063/1.2759876.

- [298] Davis, R. J.; Lloyd, M. T.; Ferreira, S. R.; Bruzek, M. J.; Watkins, S. E.; Lindell, L.; Sehati, P.; Fahlman, M.; Anthony, J. E.; Hsu, J. W. P. *J. Mater. Chem.* **2011**, *21*, 1721–1729, DOI: 10.1039/C0JM02349C.
- [299] Inbasekaran, M.; Woo, E.; Wu, W.; Bernius, M.; Wujkowski, L. *Synthetic Metals* **2000**, *111-112*, 397–401, DOI: 10.1016/S0379-6779(99)00382-3.
- [300] Gassenbauer, Y.; Klein, A. *The Journal of Physical Chemistry B* **2006**, *110*, 4793–4801, DOI: 10.1021/jp056640b.
- [301] Majumdar, A.; Adeleke, A. A.; Chakraborty, S.; Ahuja, R. *Journal of Materials Chemistry C* **2020**, *8*, 16392–16403, DOI: 10.1039/D0TC04516K.
- [302] Mosquera-Lois, I.; Kavanagh, S. R. *Matter* **2021**, *4*, 2602–2605, DOI: 10.1016/j.matt.2021.06.003.
- [303] Mannodi-Kanakkithodi, A. *Nature Physics* **2023**, *19*, 1243–1244, DOI: 10.1038/s41567-023-02049-9.
- [304] Mosquera-Lois, I.; Kavanagh, S. R.; Walsh, A.; Scanlon, D. O. *Journal of Open Source Software* **2022**, *7*, 4817, DOI: 10.21105/joss.04817.
- [305] Klapötke, T. M.; White, P. S.; Tornieporth-Oetting, I. C. *Polyhedron* **1996**, *15*, 2579–2582, DOI: 10.1016/0277-5387(95)00527-7.

